DEVELOPMENT OF SPECTRAL AND WAVELET TIME-OF-FLIGHT METHODS FOR PROPAGATING SHOCK AND DETONATION WAVES

by

ALFREDO ALBERT ORTIZ

Presented to the Faculty of the Graduate School of

The University of Texas at Arlington in Partial Fulfillment

of the Requirements

for the Degree of

MASTER OF SCIENCE IN AEROSPACE ENGINEERING

THE UNIVERSITY OF TEXAS AT ARLINGTON

December 2008

ACKNOWLEDGEMENTS

I would like to thank my research advisor Dr. Frank Lu. He helped me get to this point in my academic career by providing me with guidance and encouragement while remaining patient with my work during my graduate studies. I would also like to thank Dr. Donald R. Wilson for his help and support during my time at UTA. I would also like to thank him for inviting me to join the PDE group at the ARC. I would also like to thank Dr. Atilla Dogan and Dr. Kamesh Subbarao for being on my committee. They were very patient with my research, and provided valuable feedback on my work.

I would like to thank the UTA MAE department for providing funding for most of my time at UTA. This work was partly funded by a Research Collaboration Agreement "Ground Test Demonstrator for a Liquid-Fuelled Pulse Detonation Engine," with Temasek Laboratories, National University of Singapore. I would also like to thank the staff at the MAE department. They all helped me during my progress at UTA that made life a lot simpler.

I would like to thank my colleague Dr. Philip K. Panicker for all his help during my time at UTA. I learned a lot from him that helped guide my path during my research. I also want to thank Rafaela Bellini and Prashaanth Ravindran for helping me with Fortran and LaTex, which helped speed up my progress. I would also like to thank them along with Eric M. Braun and Richard Mitchell for their help and support during my research. They all also made life at the ARC worth attending. I would also like to thank the rest of the fellow researchers at the ARC for all the good times.

I also want to thank my family for their continued support throughout my academic career. Also, without them, I would not be where I am today.

November 26, 2008

ABSTRACT

DEVELOPMENT OF SPECTRAL AND WAVELET TIME-OF-FLIGHT METHODS FOR PROPAGATING SHOCK AND DETONATION WAVES

ALFREDO ALBERT ORTIZ, M.S.

The University of Texas at Arlington, 2008

Supervising Professor: Frank K. Lu

An accurate time delay estimate for a propagating disturbance, including an estimate of its uncertainty, is important in many areas of science. Several techniques were developed for determining the propagation time of a shock and detonation wave. The speed of the propagating wave was then determined by the time delay estimates provided for the best techniques. The techniques used ranged from the commonly used time-of-flight method to a nonstationary cross-spectral density phase method that provided a statistical estimation of the propagation time.

The time delay results for a shock tube experiment showed that most of the methods had difficulties in determining a feasible time delay estimate. These methods tended to be more sensitive to a moving time window developed for nonstationary signals. The results also showed that the application of the envelope signals typically improved the propagation time estimates.

The only methods that provided a reasonable time delay estimate on a consistent basis were the nonstationary envelope correlation coefficient method and two

variations of the Haar wavelet methods. The time delay estimates from these methods were then used to provide a statistical estimate of the velocity of the propagating waves.

TABLE OF CONTENTS

LIST OF FIGURES

LIST OF TABLES

CHAPTER 1

INTRODUCTION

1.1 Introduction

Determining the propagation time of an event is needed in many areas of science. A proper estimate of the time delay between the signals can provide the distance traveled, velocity, or angle of incidence of the propagating disturbance. Many techniques have been developed for determining these quantities in several fields ranging from large events in astrophysics and seismology to medicine and to high-energy physics.

Some of the techniques requiring the determination of the propagation time are provided. One of these utilize a moving-window cross-correlation with three thresholds to help identify the propagation of earthquakes in Spain [3]. Another technique used a hybrid cross-correlation with recurrent neural networks to enable robots to identify their surroundings [4]. Several techniques were used to determine a ranking system for concert halls in [5]. A cross-correlation coefficient method for different frequency bands was utilized and compared to several other methods, and was determined to be a valuable statistical tool for ranking concert halls. A cross-correlation fitting technique was proposed in [6] that utilizes overlapping to help determine the location of a leak in a water distribution pipeline. A wavelet cross-correlation method was used in [7] to determine the relationship between arterial blood pressure and cerebral oxyhaemoglobin for elderly patients. They propose that the wavelet cross-correlation method may prove to help diagnose a patient for autonomic failure that is difficult to distinguish with Fourier based methods [7]. Another technique proposed in [8] used a cross wavelet analysis to determine the correlation between El

Nino/Southern oscillations and North Atlantic oscillations. The paper discusses the drawbacks as well as the significance of the method for determining the correlation between the two events. A cross wavelet transform and wavelet coherence technique was proposed to determine a trend between "the mean winter state of the arctic atmosphere and winter severity reflected by ice conditions" [9]. The authors discussed the abilities of their technique as well as provided some guidelines for analyzing two time series. In [10], a wavelet cross-correlation weighted technique was proposed to detect weak gravitational waves that are difficult to resolve otherwise due to the poor signal-to-noise ratio (SNR). Another wavelet cross-correlation technique was proposed in [11] to determine the time delay of the different scales in a plane turbulent jet. The proposed method was able to distinguish the propagation of large eddies from smaller eddies. A general cross-correlation and cross-spectral technique was compared in [12] for determining the propagation distance or the angle of incidence in acoustic multiple-path experiments. The same techniques were then used to determine the propagation time for a dispersive case that consisted of analyzing the vibrations flexural and longitudinal waves at various frequencies. From the few examples cited above, it is clear that the determination of propagation time is required in many scientific disciplines. The present study is limited to determining the time delay between a pair of signals for obtaining wave propagation speeds.

Before estimating the propagation time, a classification of the signals is required for determining an appropriate approach. Broadly speaking, signals can be classified as either stationary or nonstationary. A stationary signal is preferred as it requires less computational work for estimating the time delay. A stationary signal can be classified as strongly or weakly stationary. The signal is considered to be strongly stationary when all the moments and joint moments for the ensemble of time-history

records are time invariant [13]. A weakly stationary signal is defined when the mean, variance and autocorrelation function are time invariant

$$\mu_x(t) = \mu_x \tag{1.1a}$$

$$\sigma_x(t) = \sigma_x \tag{1.1b}$$

$$R_{xx}(t,\, t+\tau) = R_{xx}(\tau) \tag{1.1c}$$

In practice though, a signal is assumed to be strongly stationary if it meets the weakly stationary requirements [13]. If the signal does not meet the requirements for weak stationarity, the signal is classified as nonstationary. In reality, all signals are nonstationary because of the finite time record since a stationary process, by definition, is of infinite duration [14]. However, the process can be assumed to be stationary for the duration. A nonstationary process can be categorized into three kinds [14]:

1. "a transient random process
2. a random processes driven by deterministically varying phenomena and
3. random processes more loosely coupled to external phenomena that evolve over time".

An example of a random process that is transient and yet driven by deterministically varying phenomena is the repeated detonation pulses in a pulse detonation engine (PDE). To illustrate, the pressure history for a PDE operating with a mixture of propane and oxygen is provided in Fig. 1.1. The figure clearly shows a time varying mean. The transducer signal displays thermal drift.

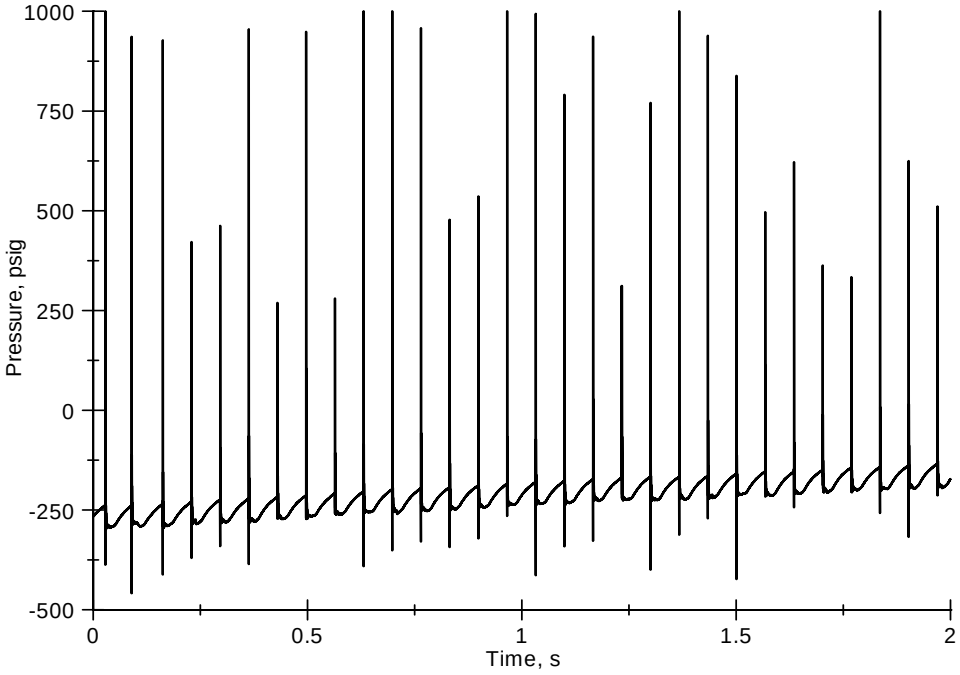

Figure 1.1. Pressure history for a single sensor in a PDE displaying the thermal drift with time.

CHAPTER 2

SENSORS

2.1 Second-order systems

Of the various methods for detecting a propagating disturbance, the present study focuses on the use of pressure transducers. The pressure transducers are PCB Model 111A24, which are integrated circuit piezoelectric quartz sensors. The specifications for these sensors are provided in Appendix B, and further information about piezoelectric sensors are provided in [15, 1].

The pressure transducers can be modeled as a second-order system, namely,

$$m\ddot{x} + c\dot{x} + kx = P(t)A_{dia} \tag{2.1}$$

where the right-hand side represents the pressure history over the diaphragm for the propagating wave. Since the pressure transducers used are modeled as second-order systems, some of the properties as well as limitations of a second-order system will be provided. Further details about second-order systems are presented in [16, 12].

A second-order system is characterized by its sensitivity K, undamped natural frequency ω_n, and damping ratio ζ, defined respectively as

$$K = 1/k \tag{2.2a}$$

$$\omega_n = \sqrt{k/m} \tag{2.2b}$$

$$\zeta = \frac{c}{2\sqrt{km}} \tag{2.2c}$$

The sensitivity is a property of all dynamic systems and characterizes the amount that an output is amplified or attenuated over the input. The frequency that the system

prefers to oscillate at is known as the undamped natural frequency, and the damping ratio defines the systems ability to dissipate energy and dampen the response of a mechanical system.

2.1.1 Time Response

Some other characteristics of the response of the system derived from these three properties are the ringing frequency, rise time, and settling time. The ringing frequency is the frequency that the system oscillates due to system being damped and is defined as

$$\omega_d = \omega_n \sqrt{1 - \zeta^2} \tag{2.3}$$

The rise and settling times are defined as the time required to meet a certain criterion due to a step response. The rise time is when the system first achieves 90% of the final value, whereas the settling time is time required for the output to settle within 10% of the final value [16]. An example of these properties for an underdamped system is shown in Fig. 2.1.

The solution to Eq. (2.1) is obtained in terms of the damping ratio. When the damping ratio is less than, equal or larger than unity, the system is said to be underdamped, critically damped and overdamped respectively. These are shown for the system's response to a step function in Fig. 2.2. As the damping ratio becomes small, the rise time decreases but this produces a ringing frequency that increases the settling time. Whereas, for high damping ratios, the system has a slower rise time with no ringing frequency, but may also have poor settling times. Typically the damping ratio for dynamic transducers lies between 0.6 and 0.8 since this provides a good balance between the ringing and settling times [16].

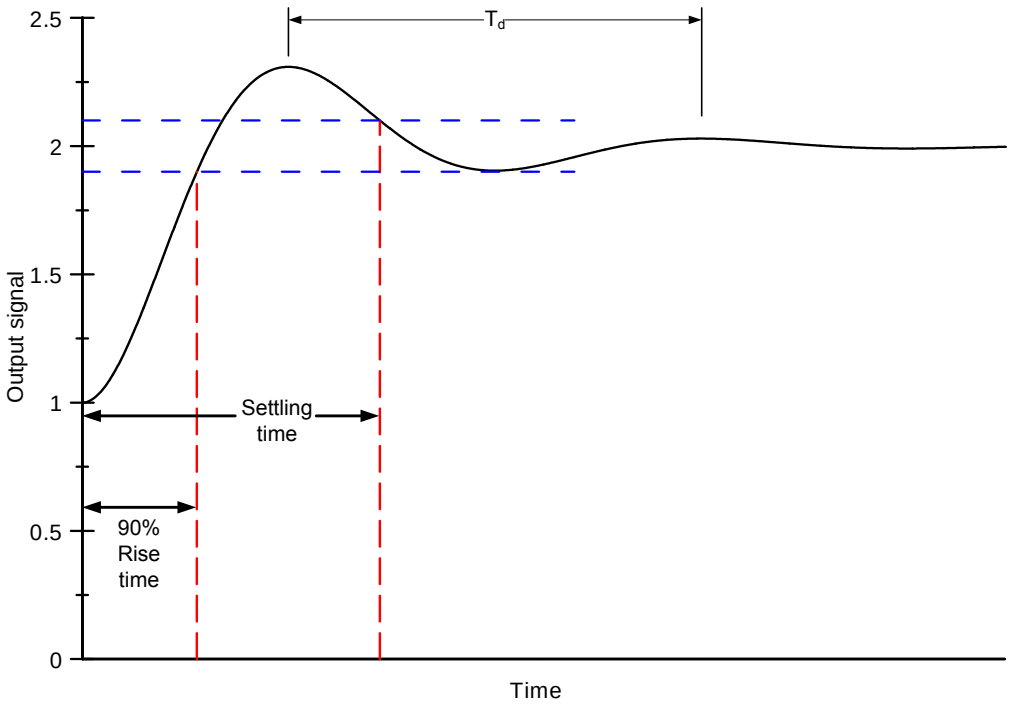

Figure 2.1. Time response for a second-order system to a step function with a damping ratio of 0.35.

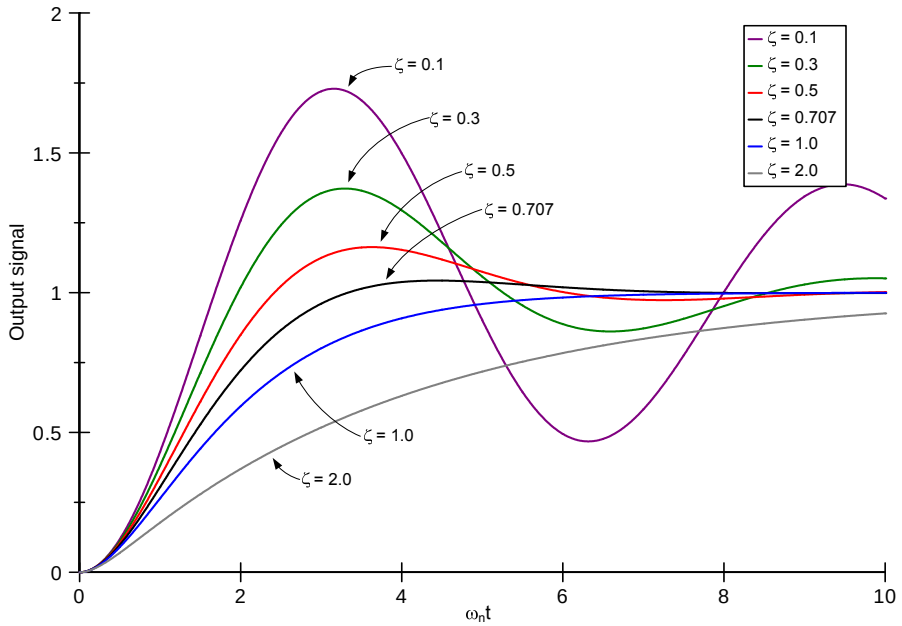

Figure 2.2. Time response for a second-order system to a step input for various damping ratios.

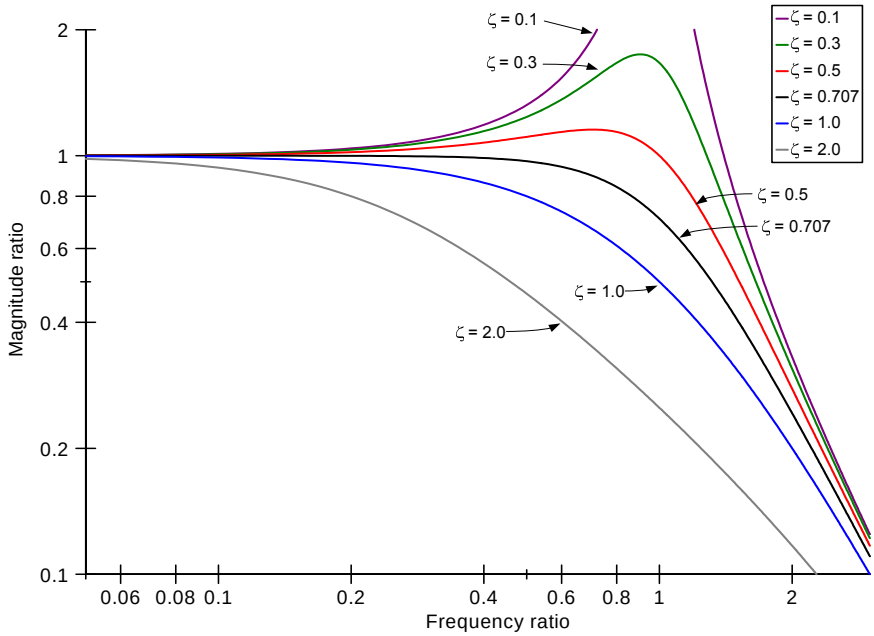

Figure 2.3. The frequency response for a second-order system. The magnitude ratio for the entire spectrum for varous damping ratios.

2.1.2 Frequency Response

The frequency response provides further information on the characteristics of a second-order system. The frequency response for various damping ratios is shown in Figs. 2.3 and 2.4. The ideal response is to have the magnitude ratio to be unity with zero phase shift for the entire spectrum. Referring to the two figures, high values of the damping ratio are undesirable as these yield a narrow range of useful frequencies with a large phase shift. On the other hand, as the damping ratio approaches zero, this also yields a narrow range of useful frequencies, limited by the resonant frequency. The resonant frequency is an undesirable effect of a lightly damped system that distorts the response. In addition, the sensor may be damaged due to amplification around the resonant frequency. The desired range for the damping ratio of 0.6–0.8 contains the best compromise between useful frequency range and an approximately linear phase shift.

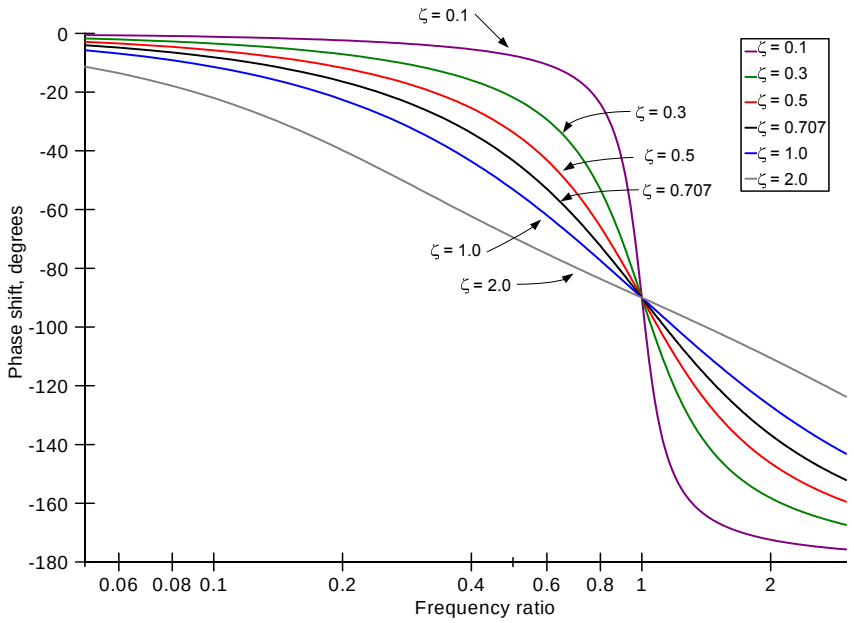

Figure 2.4. The frequency response for a second-order system. The phase shift introduced for varous damping ratios.

CHAPTER 3

MATHEMATICAL TRANSFORMATIONS

3.1 Fourier Transform

One of the most common mathematical transformations is the Fourier transform. The Fourier transform consists of sinusoidal basis functions that are used to decompose the function into an infinite set of sinusoidal functions [17]. These sets are used to produce the spectral contents for the given function, where each set contains a magnitude, a frequency and a phase component. The continuous Fourier transform (CFT) can be defined as

$$X(f) \equiv \mathcal{F}\{x(t)\} = \int_{-\infty}^{\infty} x(t)\, e^{-j2\pi ft} dt \tag{3.1}$$

where

$$e^{-j2\pi ft} = \cos(2\pi ft) - j\sin(2\pi ft) \tag{3.2}$$

Instead of the CFT, the discrete Fourier transform (DFT), is used in digital signal processing. The DFT utilizes a finite dataset that is physically realizable and it can be expressed as

$$X(k) = \sum_{n=0}^{N-1} x(n)\, e^{-j2\pi kn/N}, \quad k = 0, 1, 2, \ldots, N-1 \tag{3.3}$$

The Euler identity can then be applied to Eqn. (3.3) to decompose it into real and imaginary parts, which are used to define the amplitude and phase spectra.

The finite series of Eqn. (3.3) produces an artifact known as Gibbs phenomenon where an overshoot occurs even as the number of terms is increased [17]. The phenomenon can easily be illustrated by a square wave with its finite Fourier components

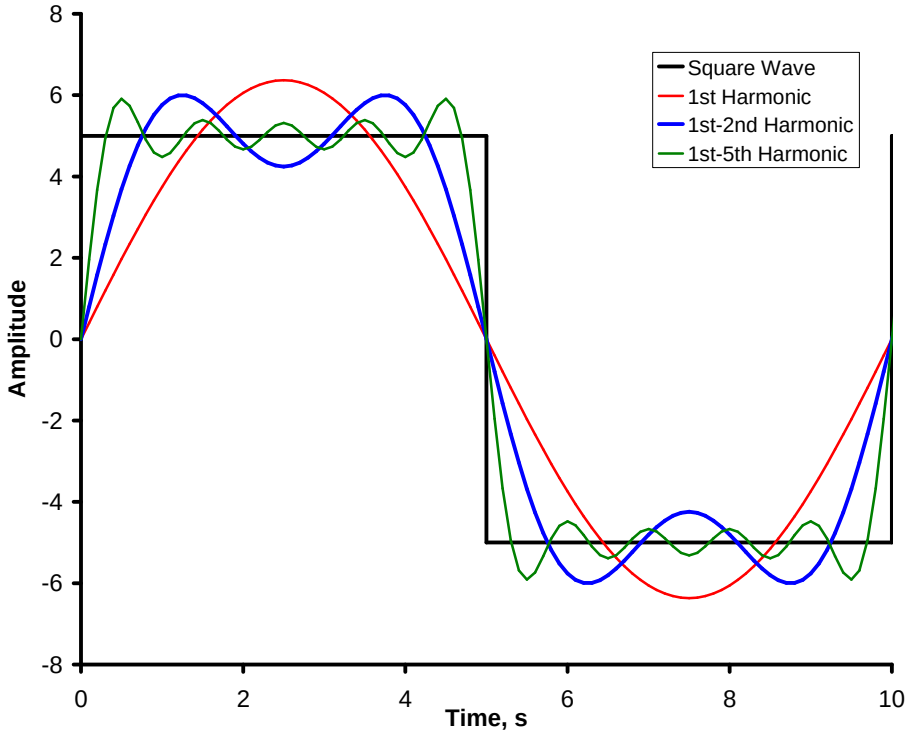

Figure 3.1. Gibbs phenomenon for a square wave with a low harmonic order representation.

as shown in Fig. 3.1. The small number of components results in a poor representation of the square wave. As more terms are used, the difference between the actual signal and its finite Fourier representation decreases as shown in Fig. 3.2. But, the sharp corners of the square wave cannot be properly captured and very large amplitude peaks result.

Another effect of using the DFT is aliasing, which occurs when the sampling rate does not satisfy the Nyquist–Shannon sampling theorem

$$f_s/2 \geq f_{signal} \tag{3.4}$$

where f_s is the sampling frequency and f_{signal} is the bandwidth of the signal. Referring to Fig. 3.3, when the sampling rate is not adequate for capturing the signal, an aliased frequency wraps around into the frequency domain of interest. The aliased frequency

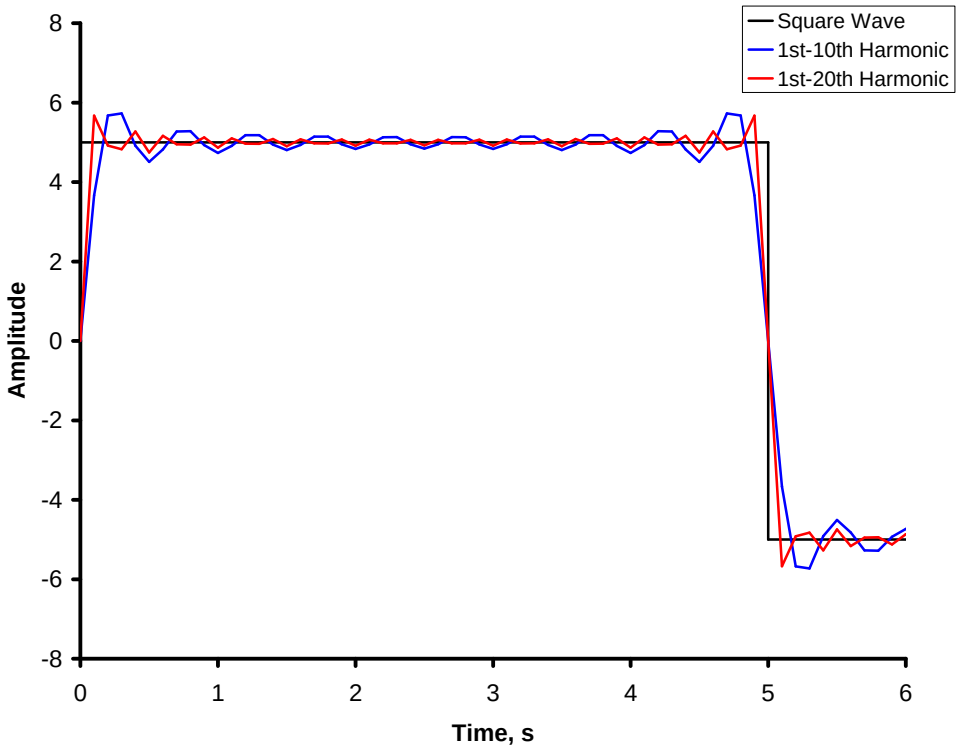

Figure 3.2. Gibbs phenomenon shown for higher-order harmonics.

causes a misrepresentation of the true spectrum. The frequency of the aliased signal is given by

$$f_{aliased} = \frac{nf_s}{2} - f_{signal}, \quad \frac{(n-1)f_s}{2} < f_{signal} < \frac{(n+1)f_s}{2} \tag{3.5}$$

There are several methods to mitigate against aliasing. One method is to sample at a rate that meets the Nyquist–Shannon sampling theorem. Another method is to use a low-pass filter to cut-off all frequencies exceeding the Nyquist frequency. The filter attenuates frequencies exceeding the cutoff frequency. The attenuation is dependent on the filter applied. In practice a low-pass filter does not follow the ideal situation of completely eliminating the frequencies outside the cutoff frequency. A roll-off rate occurs instead near the cutoff frequency that attenuates the frequencies as a function of frequency. In practice, the cutoff frequency is set in the range of $f_s/4 \leq f_c \leq f_s/2.5$, and is dependent on the roll-off rate [14]. This form of aliasing

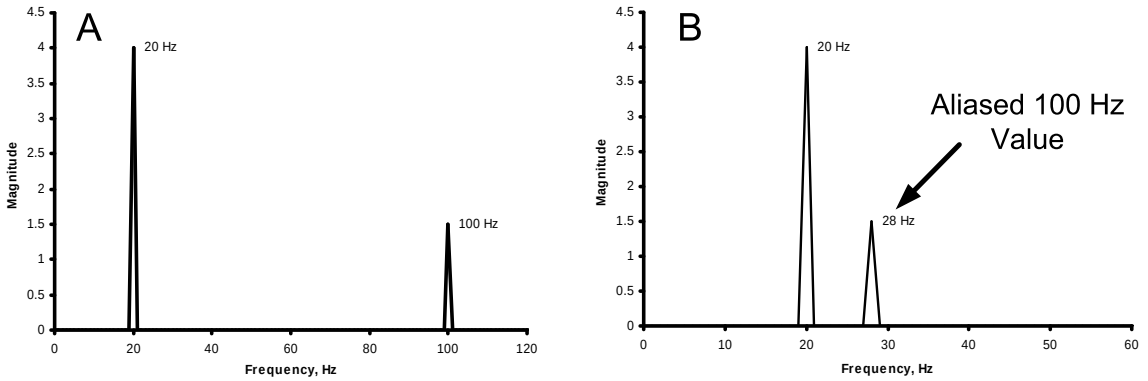

Figure 3.3. The graph on the left (A) shows the proper frequency values for the signal sampled at 256 Hz. The graph on the right (B) was sampled at 128 Hz, and contains an aliased 100 Hz signal that was folded back into the frequency domain.

is usually not an issue with acquiring data though, since most of the time the data acquisition system already contains its own low-pass filter. A (low-pass) anti-aliasing filter crucial since the noise bandwidth should be assumed to exceed the Nyquist bandwidth.

Another artifact of the DFT is due to the finite data record. The DFT assumes the time record of data to be one period of a periodic signal. Since the DFT treats the data as one period, a discontinuity is effectively introduced at both ends of the record. The discontinuity occurs when the signal's periodicity is longer than the sample record as shown in Fig. 3.4. The discontinuity appear as high frequencies. These frequencies, being higher than the cutoff frequency, are then aliased into the data bandwidth.

Further problems occur if the discrete data record is aperiodic. The non-integer frequency component leads to a leakage of energy known as spectral leakage. Spectral leakage is the energy being spread over the surrounding frequencies. The leakage follows the picket fence effect, which is shown in Fig. 3.5 [1]. There are no side lobes for an integer number of periods; the side lobes are zero. This leads to an accurate representation of the signal in the frequency domain. The problem occurs when the

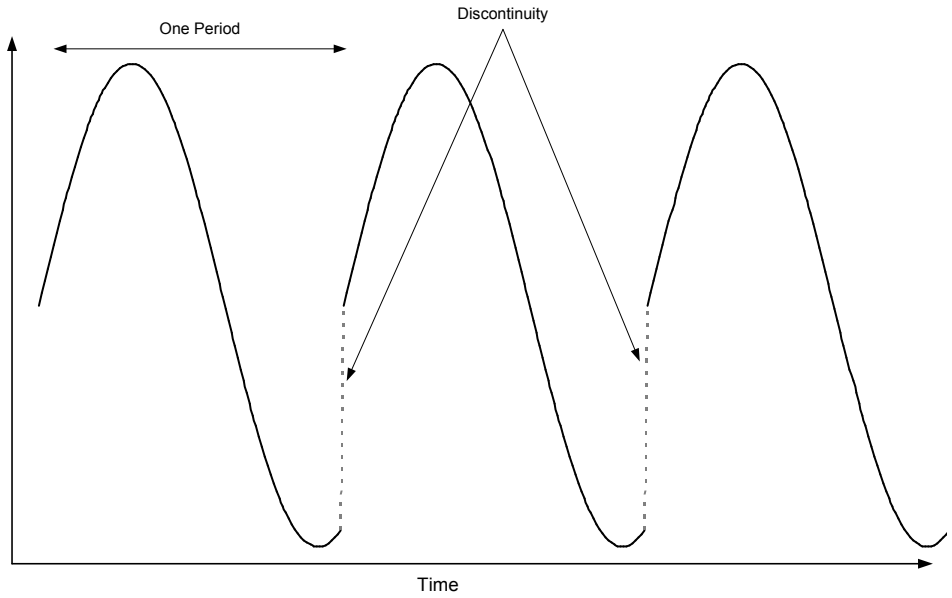

Figure 3.4. A time record showing a discontinuity between periods due to the finiteness of the data record.

signal contains a non-integer number of periods, which increases the magnitude of the surrounding frequencies. The side lobes are at a maximum when the signal contains a half-integer number of periods [1].

Spectral leakage can be reduced with windowing. Windowing is a weighting function that is multiplied to the time signal and ensures that the data contains the same value for the starting and the ending points. The data now contain no discontinuity due to the finite record, thereby reducing the spectral leakage to adjoining frequencies. There are several types of windows that can be applied to a signal with each having its own advantages and disadvantages. Selecting an appropriate window requires some *a priori* knowledge of the signal. A list of the properties of the various windows is displayed in Table 3.1. A disadvantage to using a window is that it reduces the spectral resolution and power, but the advantages far outweigh the reduction in resolution.

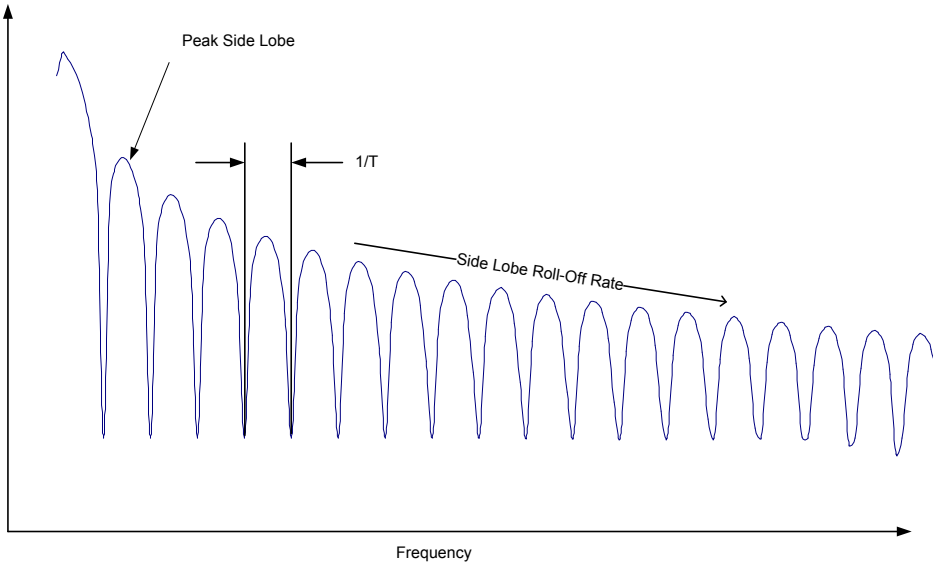

Figure 3.5. Picket fence effect for a rectangular window.

Table 3.1. Properties of some data windows [1, 2]

Window Type	Main lobe width at –6 dB	Max. side lobe (dB)	Side lobe roll-off, dB/decade
Rectangular	1.21	−13.4	−20
Hanning	2	−32	−60
Hamming	1.81	−43	−20
Blackman–Harris	2.27	−71	−20
Exact B–Harris	2.25	−67	−20
Flattop	2.94	−44	−20

Figure 3.6 shows the advantage in applying a weighting function, in this case a Hanning window, as opposed to not having a window, which is equivalent to applying a rectangular window. The figure clearly shows that the rectangular window was unable to distinguish the second frequency due to spectral leakage from the more dominant signal. On the other hand, application of the Hanning window clearly shows the presence of a smaller frequency peak that was not captured with a rectangular window. It should also be noted that even with the application of a weighting function,

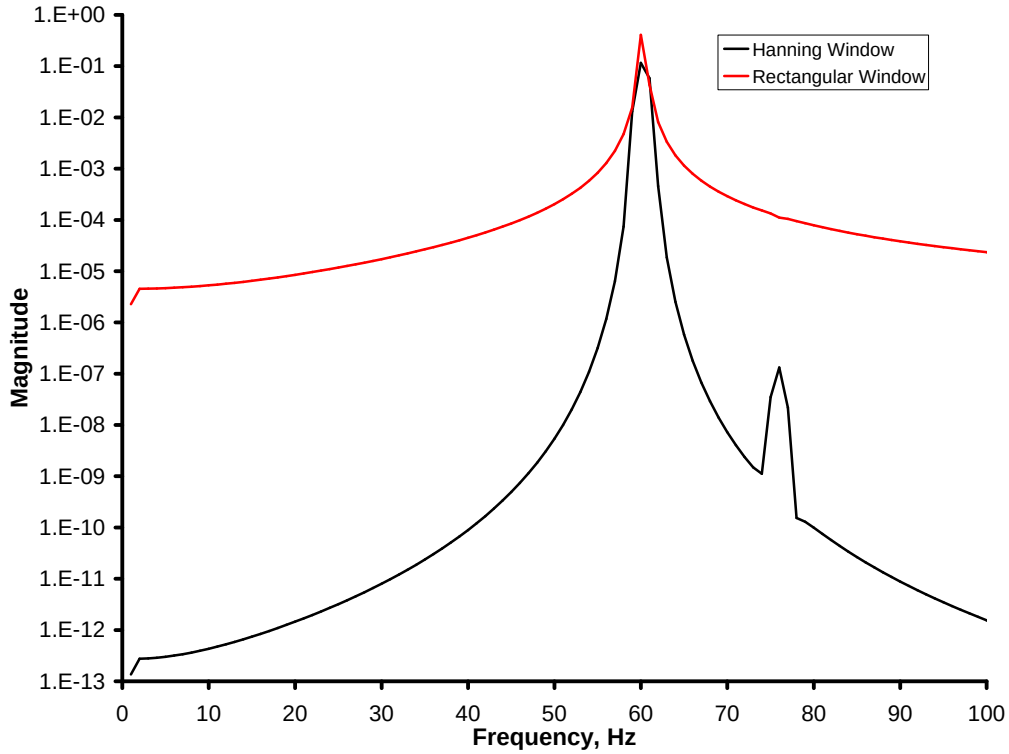

Figure 3.6. A comparison between a rectangular window and a Hanning window. The signal contains non-integer number of periods within the data record.

a low frequency component is introduced due to the DFT assumption of the signal being periodic.

3.1.1 Fast Fourier Transform

The DFT is usually computed with the fast Fourier transform (FFT) algorithm, which is a computationally efficient method for determining the DFT. The FFT outputs $(N+2)$ values for a given data record of size N. Half the data contain the real component (cosine function) and the other half contains the imaginary components (sine function). The real component represents the symmetric portion of the signal whereas the imaginary component represents the asymmetric portion.

A critical requirement of the FFT algorithm is that the sample size must be in powers of two, which may require trimming or padding of the data record. The choice of the method for achieving the correct sample size depends on the situation. Trimming the data reduces the spectral resolution and reduces the possibility of capturing the periodic component of the signal. Trimming may also cause the signal to be nonstationary. Padding the data increases the resolution. Padding is likely done by interpolation which may be misleading.

In the application of Fourier transforms, the mean component (DC offset) of the signal is usually removed. The DC offset is represented on the spectrum at a frequency of 0 Hz. The removal of the DC offset ensures that the power in the fluctuations is not overwhelmed by the power of the mean value. The FFT produces two-sided spectra that contain both the positive and negative frequencies. Usually (as in time domain signals) the negative frequencies are ignored because the negative frequencies are a mirror image of the positive frequencies. Typically after the application of the FFT, the discrete spectral content is then normalized and multiplied by two to yield the one-sided amplitude and phase spectra.

$$X(k) = \Re(k) + \Im(k) = \frac{2}{N} \left| \mathcal{F}\{x(t)\} \right| \tag{3.6a}$$

$$M(k) = \sqrt{\Re(k)^2 + \Im(k)^2} \tag{3.6b}$$

$$\theta(k) = \tan^{-1}\left[\frac{\Im(k)}{\Re(k)}\right] \tag{3.6c}$$

A relationship between frequency and the FFT indices is

$$f = k\Delta f \tag{3.7}$$

where

$$\Delta f = f_s/N \tag{3.8}$$

Hence, the ratio of the sampling rate to sample size plays an important role in the spectral resolution.

A method used for producing a better representation of the signal in the frequency domain is ensemble averaging. Ensemble averaging averages multiple data sets of the same signal to denoise the spectrum. Typically, ensemble averaging applies an overlap process. A 50% overlap with windowing is the most effective method when considering the computational time [14]. The improvements for a larger overlap process is minimal, and does not justify the additional computational time required. However, the slight improvement may be warranted, especially for nonstationary signals that may be limited to one sample set.

3.1.2 Zoom Transform

Unfortunately, while applying the DFT, the spectral resolution can be inadequate for the intended application. In such a case, a zoom transform can be applied to improve the spectral resolution for a narrowband region. An added advantage to the improved resolution is the reduction in spectral leakage [18]. The reduction in spectral leakage is especially important for identifying frequencies in close proximity of each other. A disadvantage to the application of the zoom transform is that it is computationally intensive. The transformation is achieved by applying a complex demodulation process.

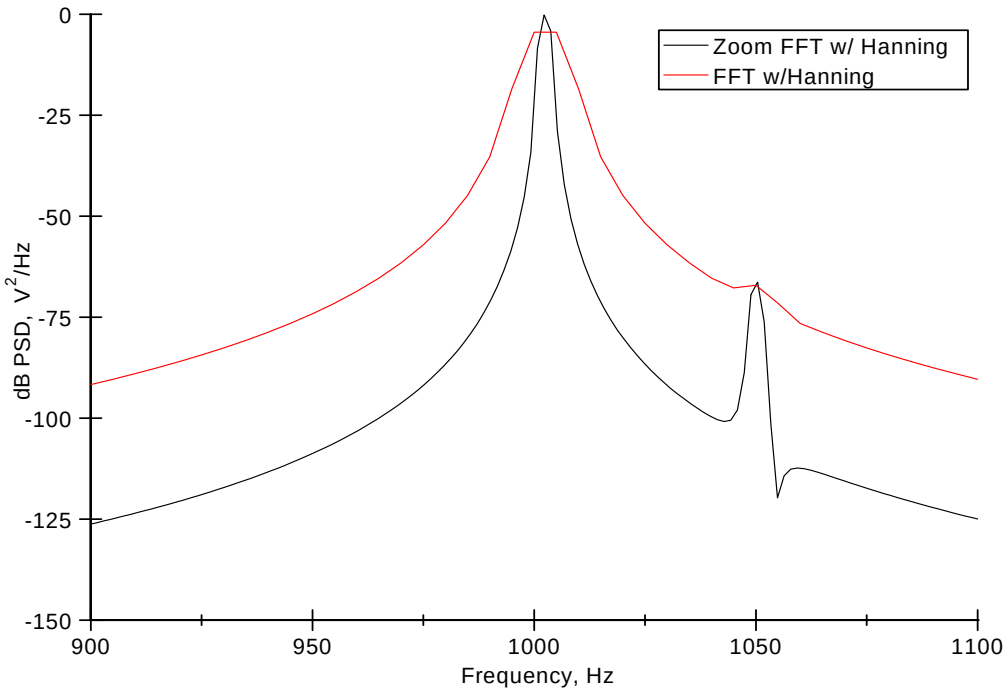

Figure 3.7. A comparison between a zoom FFT transform and an unmodified FFT transform.

$$y(t) = \begin{cases} x(t) & f_0 - B/2 \le f \le f_0 + B/2 \\ 0 & \text{otherwise} \end{cases} \tag{3.9a}$$

$$v(t) = y(t)\, e^{j2\pi f_1 t} \tag{3.9b}$$

$$V(f) = \int_0^T y(t)\, e^{j2\pi f_1 t} e^{-j2\pi f t} dt = \int_0^T y(t)\, e^{-j2\pi (f - f_1) t} dt \tag{3.9c}$$

$$G_{vv}(f) = \lim_{T\to\infty} \frac{2}{T} \mathcal{E}\left[|V(f)|^2\right] = G_{yy}(f - f_1) \tag{3.9d}$$

$$f_1 = f_0 - B/2 \tag{3.9e}$$

3.2 Hilbert Transform

The Hilbert transform (HT) is another mathematical transform that can provide insight into a signal. The HT has been applied in several applications such as

narrowband modulation, filters, and recently in the Hilbert–Huang transform (HHT). The HT is

$$\tilde{x}(t) = \mathcal{H}[x(t)] = -\frac{1}{\pi}\mathsf{P}\left(\int_{-\infty}^{\infty} \frac{x(u)}{(u-t)}du\right) \tag{3.10}$$

where P denotes the Cauchy principal value. Since the HT transformation is represented by an improper integral, it can then be defined as

$$\tilde{x}(t) = \lim_{\substack{\varepsilon\to 0 \\ A\to\infty}} \left[-\frac{1}{\pi}\left\{\int_{-A}^{t-\varepsilon} \frac{x(\eta)}{(\eta-t)}d\eta + \int_{t+\varepsilon}^{A} \frac{x(\eta)}{(\eta-t)}d\eta\right]\right\} \tag{3.11}$$

Noting that the HT can also be written as the convolution integral

$$\tilde{x}(t) = x(t) \otimes \frac{1}{\pi t} \tag{3.12}$$

it can be computed by transforming the equation into the frequency domain. The Fourier transform of Eqn. (3.12) is

$$\mathcal{F}[\tilde{x}(t)] = \mathcal{F}[x(t)]\,\mathcal{F}\left[\frac{1}{\pi t}\right] = X(f)\,[-j\,\mathrm{sgn}(f)] \tag{3.13}$$

where

$$\mathrm{sgn}(f) = \begin{cases} 1 & f > 0 \\ 0 & f = 0 \\ -1 & f < 0 \end{cases} \tag{3.14}$$

Hence, the HT produces a phase shift of 90 degrees to the original function while keeping the magnitude of the frequency component unchanged [19]. The new function is orthogonal to the original function.

The HT of the signal is often used to create the analytic function

$$z(t) = x(t) + j\tilde{x}(t) = A(t)\,e^{j\theta(t)} \tag{3.15}$$

where the instantaneous amplitude (envelope) and phase are

$$A(t) = \left[x^2(t) + \tilde{x}^2(t)\right]^{1/2} \tag{3.16a}$$

$$\theta(t) = \tan^{-1}\tilde{x}(t)/x(t) \tag{3.16b}$$

The instantaneous angular frequency is then defined by the rate of change of the instantaneous phase w.r.t. time,

$$\dot{\theta}(t) = \omega(t) = 2\pi f(t) \tag{3.17}$$

The envelope of a signal is one of the useful quantities developed from the analytic signal. An application of the envelope function is the identification of the trend of an autocorrelation function. An example is shown in Fig. 3.8. This figure shows that the correlation trend (red solid line) is easily determined with the use of the envelope function. The trend shows how randomness affects the signals predictibility for future terms.

3.3 Wavelet Transform

The wavelet transform (WT) is also useful for signal processing. The main advantage of WT is the ability to localize both frequency and time for a given signal. The localization of the time and frequency is the identification of the intervals in the time-frequency representation that contain the energy of the signal [20]. The localization of both frequency and time with the Fourier method is problematic due to the fixed window size [20]. For the FT, good frequency localization is achieved with a large window that indicates good frequency resolution with poor time resolution throughout, whereas good time localization is achieved with a small window that has good time resolution with poor frequency resolution. In other words, the FT can achieve good frequency or time localization by spreading the energy in the time or

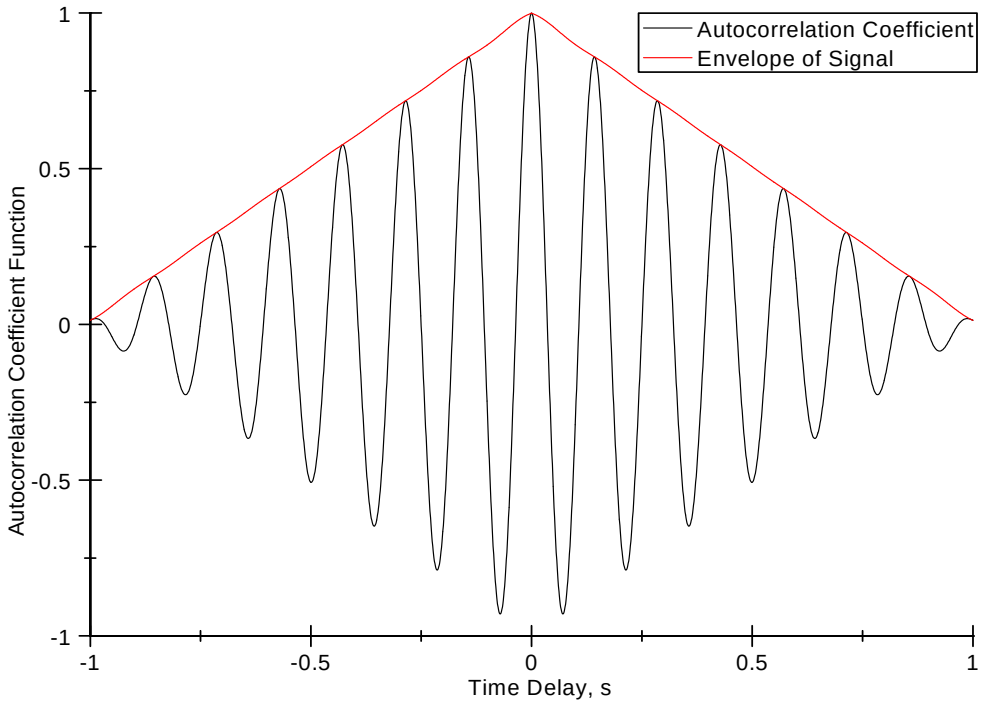

Figure 3.8. The envelope of an autocorrelation function for a noisy sine wave.

frequency domain. The WT resolves this issue by having the width of the window vary from low to high frequency. The varying window allows the WT to achieve good time localization for high frequency bands, which tends to have a shorter time duration. Whereas for low frequency bands that are usually of longer time duration, the WT has good frequency localization. The WT has become particular useful in analyzing nonstationary signals due to the inherent properties associated with the transformation.

In fact, there are many types of time-frequency representations, such as wavelets, short-time Fourier transforms, and the Wigner-Ville distribution. All the time-frequency representations are governed by the time-frequency uncertainty principle that results in a tradeoff of the localization of time for frequency and vice versa [21]. The uncertainty principle is a modification of the Heisenberg uncertainty principle ap-

plied for signal processing. The uncertainty principle is defined by the time-frequency bandwidth product

$$\Delta_t \Delta_\omega \geq \frac{1}{2} \tag{3.18}$$

which defines a lower bound for the time and frequency localization. The time-frequency bandwidth can be derived from the application of Schwartz' inequality to the time duration [[What is E?]]

$$\Delta_t^2 = \frac{1}{E} \int_{-\infty}^{\infty} (t - \langle t \rangle)^2 |x(t)|^2 \, dt = \int_{-\infty}^{\infty} t^2 \frac{|x(t)|^2}{E} \, dt - \langle t \rangle^2 \tag{3.19}$$

and the frequency bandwidth

$$\Delta_\omega^2 = \frac{1}{2\pi} \int_{-\infty}^{\infty} (\omega - \langle \omega \rangle)^2 \frac{|X(\omega)|^2}{E} d\omega = \frac{1}{2\pi} \int_{-\infty}^{\infty} \omega^2 \frac{|X(\omega)|^2}{E} \, d\omega - \langle \omega \rangle^2 \tag{3.20}$$

which are both normalized by the Energy of the signal. The derivation for the uncertainty principle is provided in several introductory wavelet books [22, 20, 23].

3.3.1 Continuous Wavelet Transform

The continuous wavelet transform (CWT) is the continuous-time transformation for a given signal. The CWT consists of a a family of dilated and translated wavelets that are

$$\psi_{a,b}(t) = \frac{1}{\sqrt{|a|}} \psi \left(\frac{t-b}{a} \right) \tag{3.21}$$

The mother wavelet is the template basis function that is used for determing the family of wavelets. The mother wavelet has to have a zero mean, which follows from the admissibility condition. The admissibility condition is

$$C_\psi = \int_{-\infty}^{\infty} \frac{|\Psi(\omega)|^2}{\omega} d\omega < \infty \tag{3.22}$$

which is a requirement if perfect reconstruction of the signal is needed. In most cases, the admissibility condition is satisfied in construction of the mother wavelet.

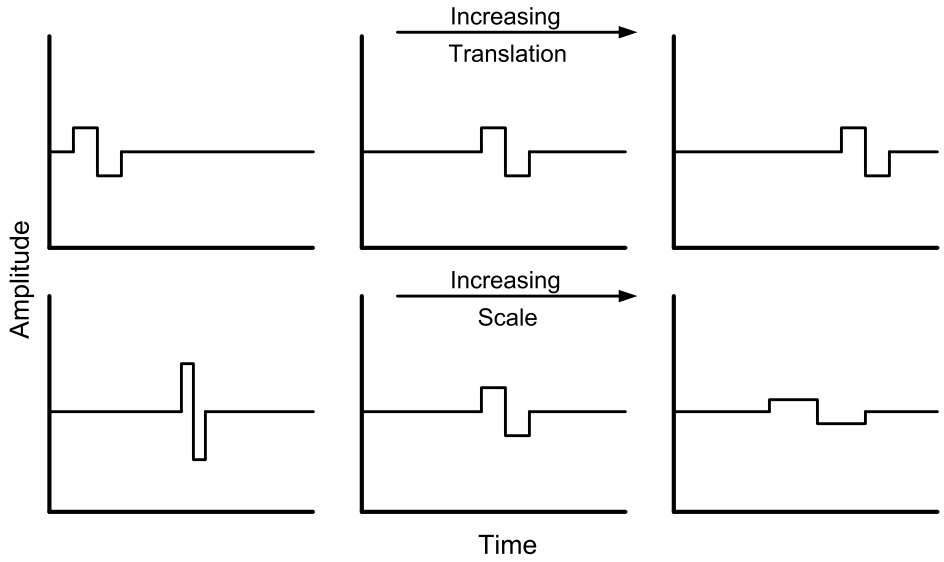

Figure 3.9. A translation and dilation of the Haar wavelet.

The mother wavelet is used to generate a family of daughter wavelets that have been dilated and translated with Eqn. (3.21). Dilation of the wavelets is defined by scales, which are related to frequency. The scaling of the wavelet has a compression effect on the mother wavelet that is used to form a daughter wavelet. The compressed versions of the mother wavelet also have shorter time durations that allow for more accurate time localization of the higher frequency component. The translation of the mother wavelet has no effect on the wavelet function other than a shift in time. An example of the Haar mother wavelet translated and dilated is shown in Fig. 3.9. Referring to Fig. 3.9, the top half shows the Haar wavelet translated in time, which remains a uniform shape throughout. The bottom half consists of the Haar wavelet located at the same time, but for various scales. The amplitude and time duration varies as a function of the scaling factor. With increasing scale, the amplitude decreases while the time duration increases. The total energy is uniform throughout as the power remains the same for the various translations and dilations.

Just as for the FT, the family of daughter wavelets are orthogonal to each other. The family of daughter wavelets is used to compute the CWT

$$\mathrm{CWT}\,(a,b) = \int_{-\infty}^{\infty} \psi^{*}_{a,b}\,(t) f\,(t)\,dt \tag{3.23}$$

The CWT has a varying scale and time grid that forms a constant relative bandwidth (Q) grid. The constant Q is

$$Q = \frac{2\Delta_{\omega}/a}{\omega_0/a} = \frac{2\Delta_{\omega}}{\omega_0} \tag{3.24}$$

which relates the spectral width with a mean frequency. An example of the constant relative bandwidth grid is shown in Fig. 3.10. The grid shows for ow frequencies (large scales) a finer frequency band with poor time localization. On the other hand, the high frequencies (low scales) have a poor frequency band, but have a much better time localization. The CWT also conserves energy after the transformation like the FT.

Similar to the CFT, the CWT cannot be implemented in digital signal processing. A solution to this problem is to discretize the CWT. Note, this is not the same as the discrete wavelet transform (DWT), which applies high- and low-pass filters to determine the wavelet coefficients at various levels. A scalogram is used for displaying the CWT for various scales with time. The scalogram is a time-frequency representation commonly used for wavelet analysis. The scalogram is a representation of the energy spectrum, which is

$$E_{CWT}\,(a,b) = |\mathrm{CWT}\,(a,b)|^2 \tag{3.25}$$

The wavelet phase angle is

$$\theta_{CWT}\,(a,b) = \tan^{-1}\left[\frac{\Im\,[CWT\,(a,b)]}{\Re\,[CWT\,(a,b)]}\right] \tag{3.26}$$

and is neglected in some cases when the basis function consists of only real values.

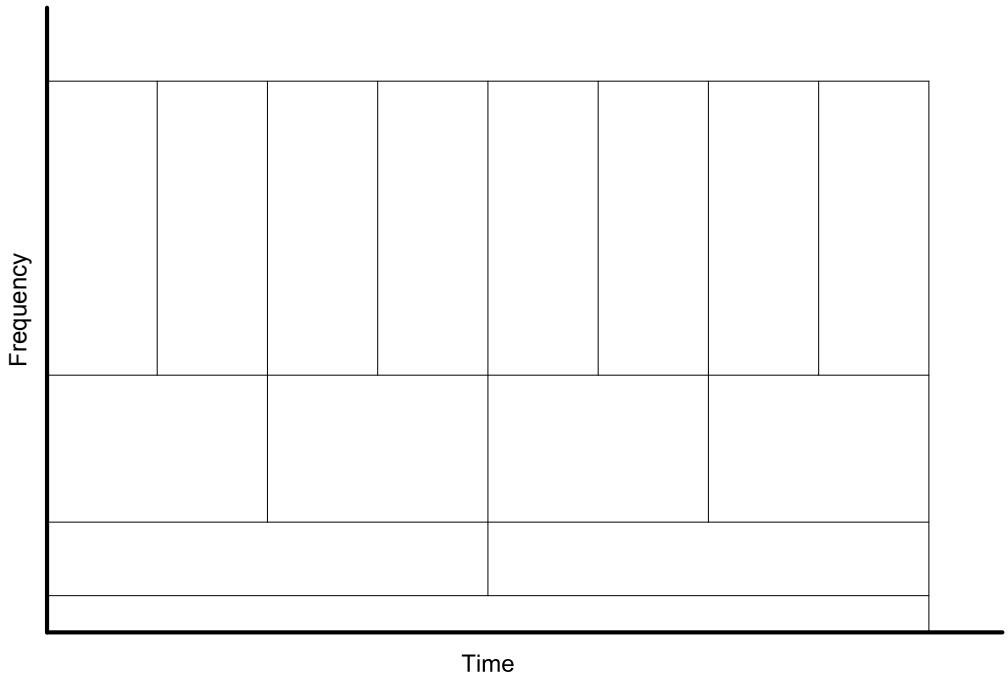

Figure 3.10. A general grid representing the varying time and frequency resolution for a CWT.

Another useful parameter is the wavelet ridge that is defined by

$$\frac{dE_{CWT}(a,b)}{da} = 0 \tag{3.27}$$

which is a representation of the local maxima of the energy spectrum. The wavelet ridge is particularly useful for extracting the extreme energy signatures from the energy spectrum.

3.3.2 Cone of Influence

The cone of influence (COI) is the effect that discontinuities and the edges of a finite signal create in the scalogram [24]. The COI affects the analysis of the energy spectrum that is ultimately the result of the end discontinuities from the finite record. The COI can be considered to be a contamination of the spectrum, which increases linearly with increasing scale [24]. An example of the COI for a Kronecker delta

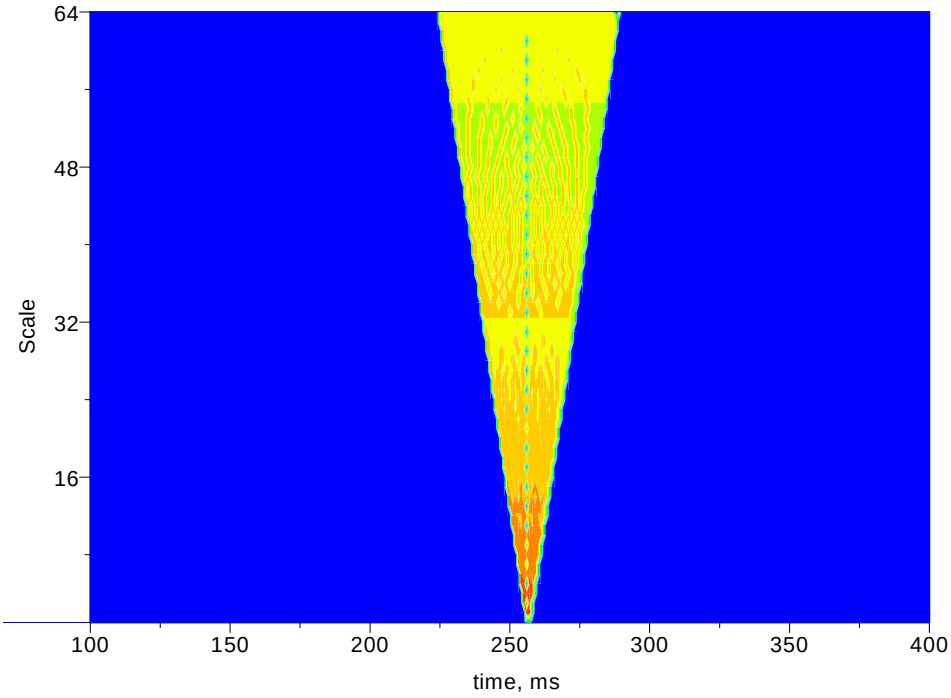

Figure 3.11. The effect of the cone of influence for an impulse function.

utilizing a Haar wavelet is shown in Fig. 3.11. Note that for the Haar wavelet, the width of the COI increases with a 1:1 ratio with scale. It has good time localization of the discontinuity for low scale values (high frequencies).

There are many types of mother wavelet functions that have been created to utilize the properties associated with the WT. Each mother wavelet function provides its own advantages and disadvantages, like the weighting functions for the DFT. A brief introduction to some of the wavelets utilized in this study are now provided.

3.3.3 Haar wavelet

The Haar wavelet is the first and simplest wavelet. It is also the least computational intensive wavelet and may be preferred for quick computations. The Haar wavelet is

$$\psi(t) = \begin{cases} 1 & 0 \leq t < \frac{1}{2} \\ -1 & \frac{1}{2} \leq t < 1 \\ 0 & \text{otherwise} \end{cases} \tag{3.28}$$

The Haar wavelet is orthogonal in translation and dilation for all the wavelets. It has good time localization but bad frequency localization. Referring to Fig. 3.12, the frequency information of the Haar wavelet has a broad peak with ripples throughout due to the discontinuity in the time domain. The applications for the Haar wavelet are limited due to the discontinuity.

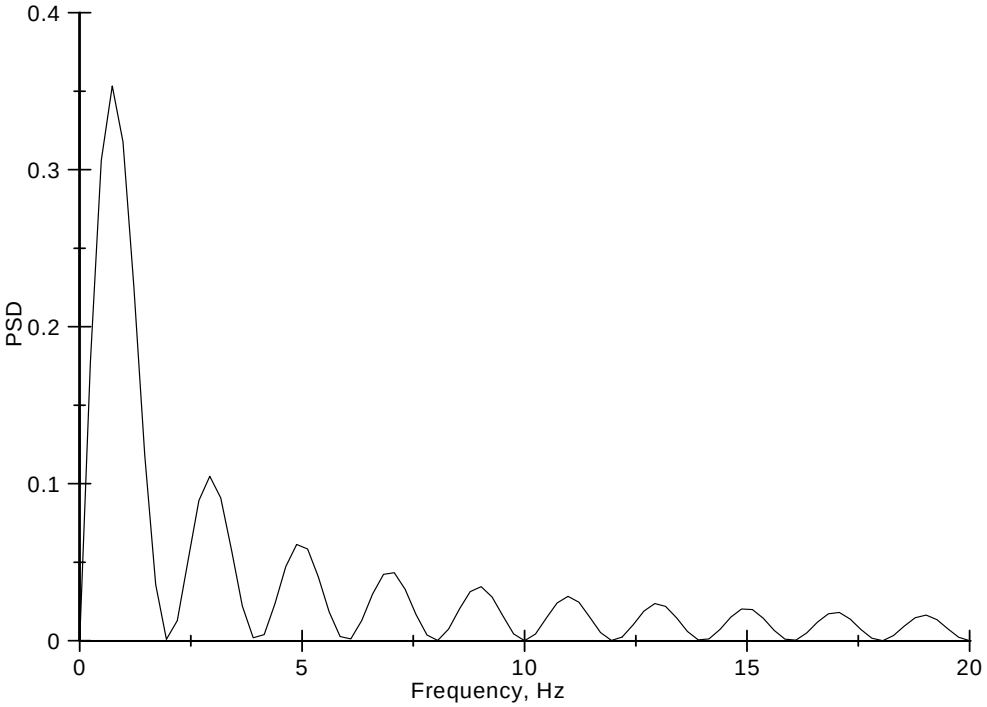

Figure 3.12. The frequency content for the Haar wavelet.

3.3.4 Morlet wavelet

The Morlet wavelet is more complicated than the Haar wavelet and it is a modulated Gaussian function

$$\psi(t) = \frac{1}{\sqrt{\pi f_b}} e^{j2\pi f_c t} e^{-t^2/f_b} \tag{3.29}$$

where

$$f_b = \int f^2 \Psi df \tag{3.30}$$

The Morlet wavelet is a complex wavelet function that does not satisfy the admissibility condition [21]. Modifications to the Morlet wavelet can be done to satisfy the condition if reconstruction is necessary. The wavelet has good time and frequency localization since it has exponential decays in both domains. The localization is governed by the central frequency which, for high values, reduces the Morlet wavelet function to

$$\psi(t) = \pi^{-1/4} e^{j2\pi f_c t} e^{-t^2/2} \tag{3.31}$$

The center frequency has a direct relationship on the number of oscillations that the wavelet exhibits. For high frequencies, the number of oscillations increases while improving the spectral resolution and decreasing the temporal resolution [25]. An example of a Morlet wavelet in the time and frequency domain is provided in Fig. 3.13. Referring to Fig. 3.13, the left-hand side contains the real and imaginary components for a Morlet wavelet function with a wavelet's central frequency of seven in the time domain. The right-half side shows the Fourier transform of the Morlet wavelet, which has a better resolved frequency component then the Haar wavelet shown in Fig. 3.12.

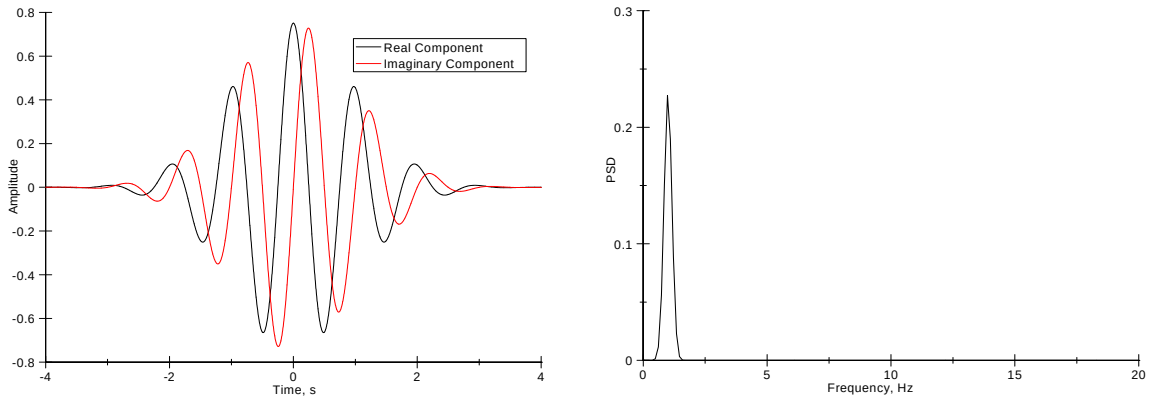

Figure 3.13. The time and frequency domain for a Morlet wavelet.

CHAPTER 4

METHODS FOR DETERMINING THE PROPAGATION TIME

The propagation time or time delay related to the passage of a disturbance is a ubiquitous parameter in a large number of scientific and engineering disciplines. This chapter starts off by introducing the usual approach, known as the time-of-flight method. With advances in computing hardware and software, more sophisticated techniques can be developed that provide an estimate of not only the time delay but also the uncertainty of the estimate. These techniques applied specifically to the propagation of a shock or detonation wave are described.

4.1 Time of Flight

The time of flight (TOF) method is the classic method for determining the propagation time of a disturbance. In this method, the propagating disturbances passes by two sensors that generate two signals with a time delay. Thus, this method assumes that the time delay between the signals can be distinguised. The TOF method determines the propagation time by selecting a single point for each sensor as a point of comparison. The selection of the points is arbitrary, and is generally the peak value. The difference between the peak-to-peak values for the given transducers is thus used to determine the propagation time. The TOF method is the most simplistic approach for the determination of the propagation time. However, it has an unknown uncertainty arising from the selection process, which can be problematic if the signals are not distinct. An example of the selection possibilities is shown in Fig. 4.1 for the TOF method. The figure shows some of the selection possibilities for the given

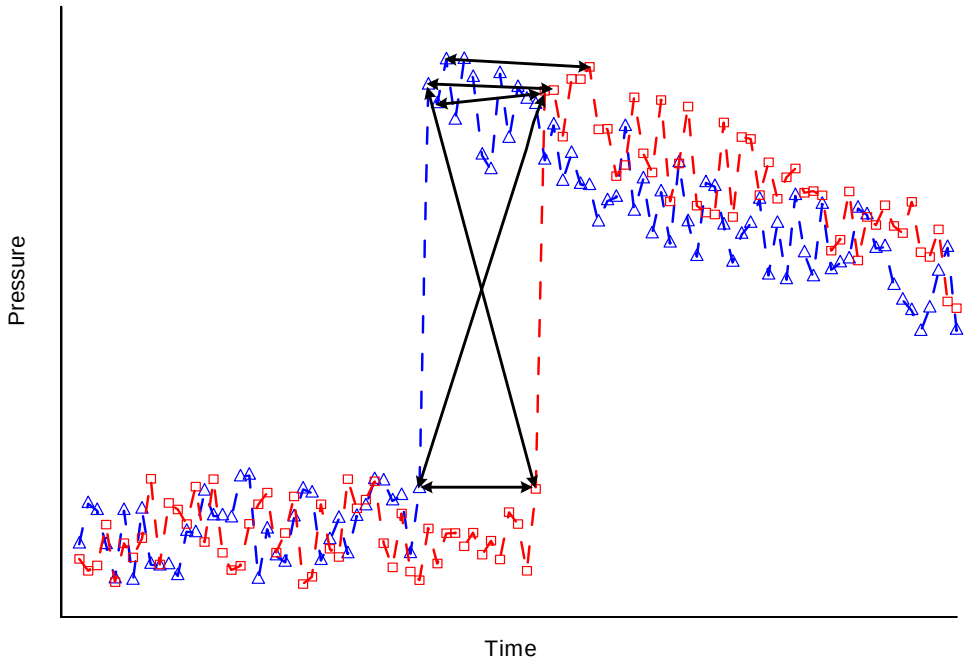

Figure 4.1. Some of the selection possibilities for determining the TOF.

signals. Since each of the selction possibilities are a viable option for the signals, the randomness in the selection process introduces an undefined uncertainty.

4.2 Cross-Correlation Coefficient

The cross-correlation coefficient (CCC) is another method for determining the propagation time. The CCC is a normalization of the cross-correlation function (CCF). The CCF is a joint statistical property for a pair of random records that measures the fundamental properties shared by the pair of records in the time domain [13]. The CCF can be defined as

$$R_{xy}(\tau) = E[x(t)\, y(t+\tau)] = \int_{-\infty}^{\infty} x(t)\, y(t+\tau)\, dt \tag{4.1}$$

The CCF provides an estimate of the time delay between the given signals due to the propagation of a disturbance under the assumption of stationarity [13]. Poor SNR

have negligible influence on the time delay estimate [26, 27]. The time delay estimate is provided by the maxima in the cross-correlation, which is the peak value for the CCF.

Since the experiments are acquired at a finite rate for a finite period of time, the CCF has to be modified for discrete data. The discrete, biased estimate CCF is given by

$$\hat{R}_{xy}\left(i_\tau\right) = \frac{1}{N}\sum_{i=0}^{N-1} x\left(i\right) y\left(i+i_\tau\right), \quad i_\tau = -(N-1), -(N-2), \ldots, N-2, N-1 \tag{4.2}$$

where the time delay is determined by

$$\tau = i_\tau / f_s \tag{4.3}$$

and

$$\Delta t = 1/f_s \tag{4.4}$$

The estimate is said to be biased because of the finite window.

As an example, Fig. 4.2 shows a generated sinusoidal signal at 4 Hz and another at the same frequency but phase delayed by 90 deg. A pair of sine waves were used because the signals have a known cross-correlation function. The CCF for the signals is also a sine wave that has a phase equivalent to the time delay between the pair of signals [13]. The biased estimate of the CCF output for the two signals is shown in Fig. 4.3. Referring to Fig. 4.3, the CCF shows stronger correlations in the vicinity near no time delay. The CCF also shows a decaying trend with increasing time delay due to the finite window. This is unlike the analytical result if the two signals are infinitely long since the cross-correlation will then be an infinite sine function of constant amplitude between -1 and 1. The peaks further from the maximum peak become broader, indicating weaker correlations.

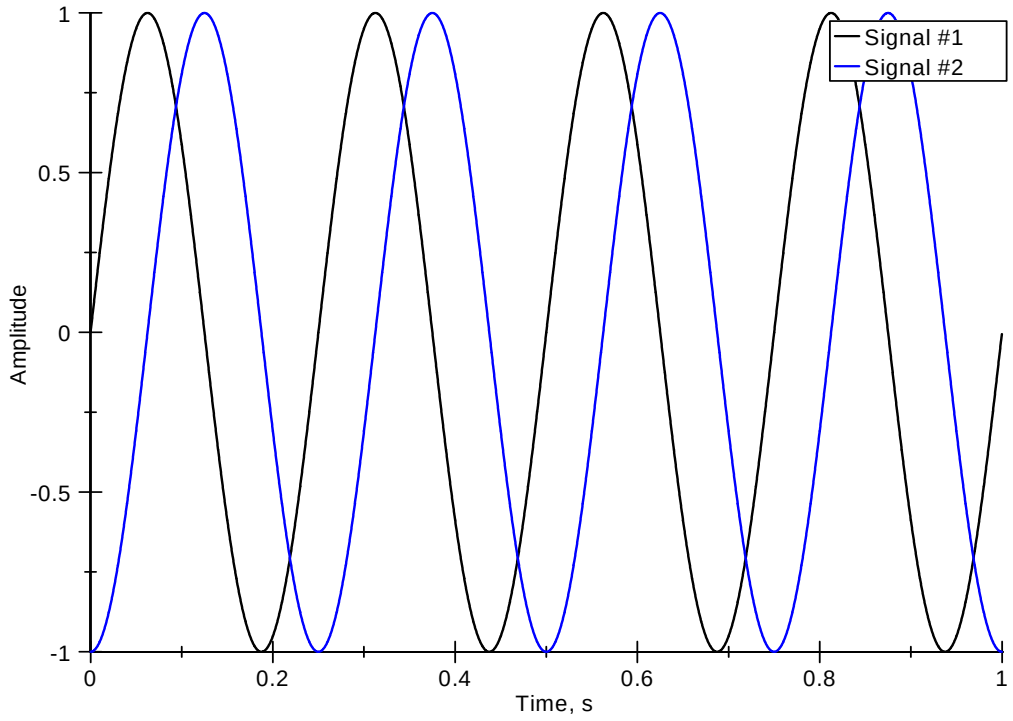

Figure 4.2. Generated sinusoidal functions at 4 Hz that are 90 degrees out of phase.

An unbiased estimate that corrects for the error near the edges of the window is

$$\hat{R}_{xy}\left(i_\tau\right) = \frac{1}{N - |i_\tau|} \sum_{i=0}^{N-1} x\left(i\right) y\left(i + i_\tau\right), \quad i_\tau = -(N-1), -(N-2), \ldots, N-2, N-1 \tag{4.5}$$

The unbiased estimate of the CCF output is for the given signals is displayed in Fig. 4.4. Unlike the biased estimate, the unbiased estimate of the CCF has uniform correlated peaks for the signals, as in the analytical solution of two infinite, continuous sine as mentioned above. Uncertainty for large time delays has been removed since the peaks do not broaden. The unbiased estimate also provides more accurate estimates of the time delay as is shown in Table 4.1 for the pair of signals. Referring to the table's row with an actual time delay of 0.0624 seconds, the biased estimate provides a skewed result of the time delay that is off by 0.0016 seconds. The unbiased estimate

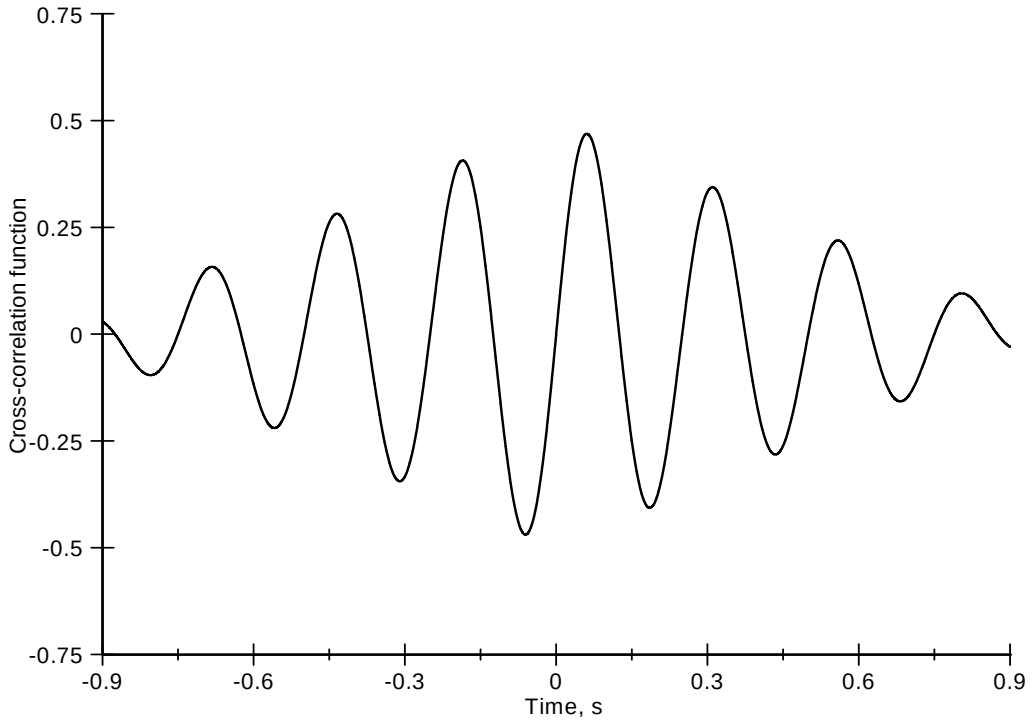

Figure 4.3. The biased estimate of the CCF for the generated signals provided in Fig. 4.2.

Table 4.1. Time delay estimates for the biased and unbiased CCF

Actual, s	Biased, s	Δt_{biased}	Unbiased, s	$\Delta t_{unbiased}$
−0.9376	−0.9194	0.0182	−0.9376	0.0000
−0.6876	−0.6826	0.0050	−0.6876	0.0000
−0.4376	−0.4348	0.0028	−0.4376	0.0000
−0.1876	−0.1856	0.0020	−0.1876	0.0000
0.0624	0.0608	0.0016	0.0624	0.0000
0.3124	0.3102	0.0022	0.3124	0.0000
0.5624	0.5590	0.0034	0.5624	0.0000
0.8124	0.8046	0.0078	0.8124	0.0000

on the other hand has correctly identified the time delay. The table also shows that the biased estimate provides a poorer estimate of the time delay than the unbiased estimate, worsening with increasing time delay. Since the unbiased estimate provides the superior results, it will be the estimate used for the CCC.

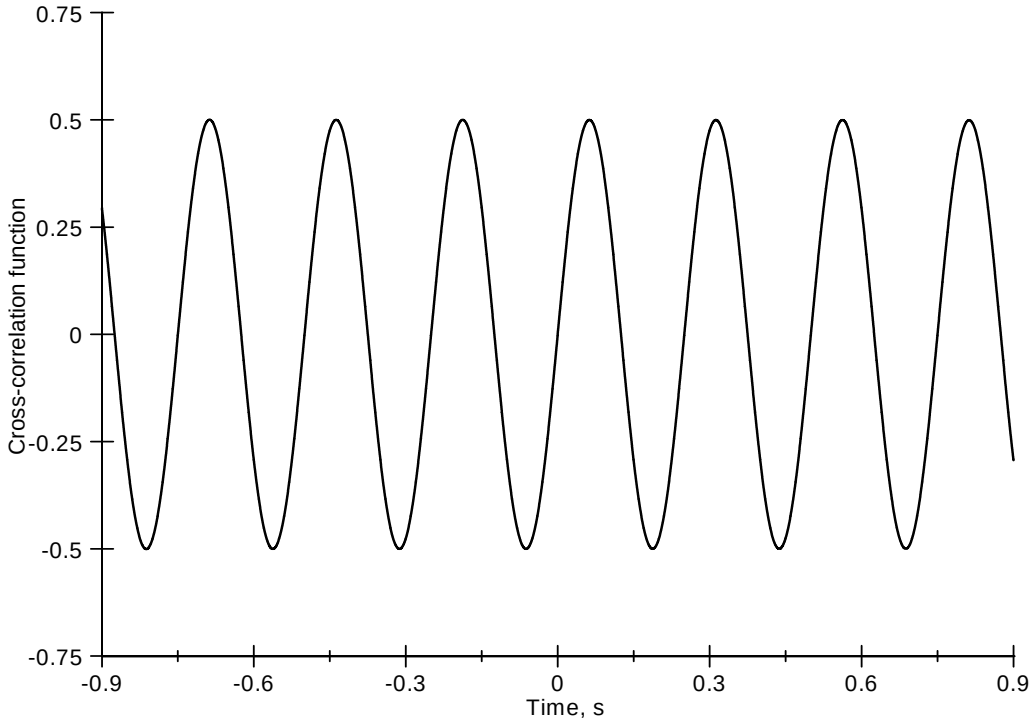

Figure 4.4. The unbiased estimate of the CCF for the generated signals provided in Fig. 4.2.

The unbiased estimate of Eqn. (4.5) has to be modified for nonstationary signals. The nonstationary CCF can be written as

$$\hat{R}_{xy}\left(l, i_\tau\right) = \frac{1}{N - |i_\tau|} \sum_{i=k}^{N-1} x\left(i\right) y\left(i + i_\tau\right), \quad l = 0, 1, \ldots, N-1 \tag{4.6}$$

where $M \leq N$ and l is the time index value. The nonstationary CCF accounts for the CCF varying with time. In other words, it relaxes the stationary assumption. The time delay estimate is now achieved by averaging the peak values for the ensemble of CCF through different values of l. The time delay estimate is given by

$$\hat{\tau} = \frac{1}{M} \sum_{i=0}^{M-1} \hat{\tau}_{i\ Max} \tag{4.7}$$

where $\hat{\tau}_{i\ Max}$ is the time delay value for the maximum correlated point for the given CCF.

A variation of the nonstationary CCF was proposed in [26] that provided criteria for analyzing nonstationary events. The three criteria proposed were

1. Isolate the nonstationary event by not including any other events,
2. apply Chauvenet's acceptance criterion, and
3. exclude the region where the nonstationary event does not occur for either signal [26].

The proposed nonstationary CCF was slightly modified to account for the time window and is given by

$$\hat{R}_{xy}\left(L, U, i_\tau\right) = \frac{1}{\left(U - L + 1\right) - \left|i_\tau\right|} \sum_{i=L}^{U} x\left(i\right) y\left(i + i_\tau\right) \tag{4.8}$$

where L and U are the lower and upper time index value. An example of the time window with the proposed criteria is shown in Fig. 4.5. The figure shows a nonstationary event that propagates followed by a reflection propagating in the opposite direction. The main window covering the nonstationary event is shown by the rectangular window (black solid lines) with the lower and upper time limits. The lower and upper time limits are used to define all the possible windows for the nonstationary CCF.

A pair of transducers spaced 4 inches apart was used to record the detonation wave. The signals were sampled at 240 kHz, and are provided in Fig. 4.7. The figure shows both signals capturing the nonstationary event as the detonation wave propagates. Both signals exhibit a von Neumann spike with an oscillating exponential decay. The maximum value from the nonstationary CCF for each window is used to generate a time delay surface as a function of T_U and T_L as shown in Fig. 4.6 for the data of Fig. 4.7. The time delay surface is relatively flat for a large percentage of the surface. The time delay surface contains portions that have significant variations in the estimate of the time delay. The large variations occur as the edges of the window approach the nonstationary event, which provides limited information for the CCF to properly

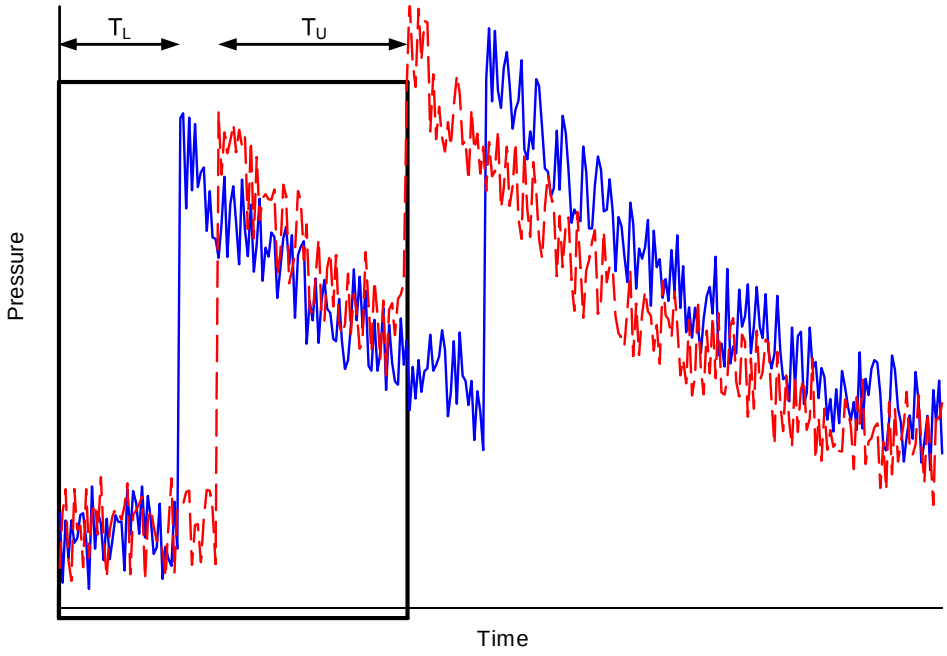

Figure 4.5. An example of the time varying window imposed by the three criteria for nonstationary signals.

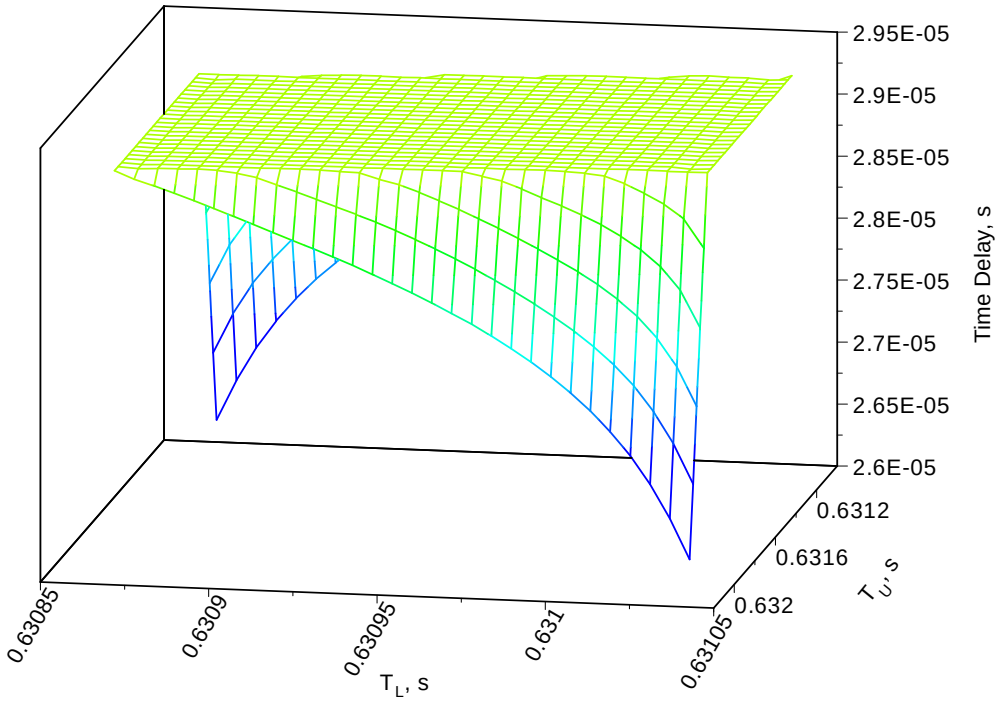

Figure 4.6. An example of the time delay surface for the nonstationary CCF.

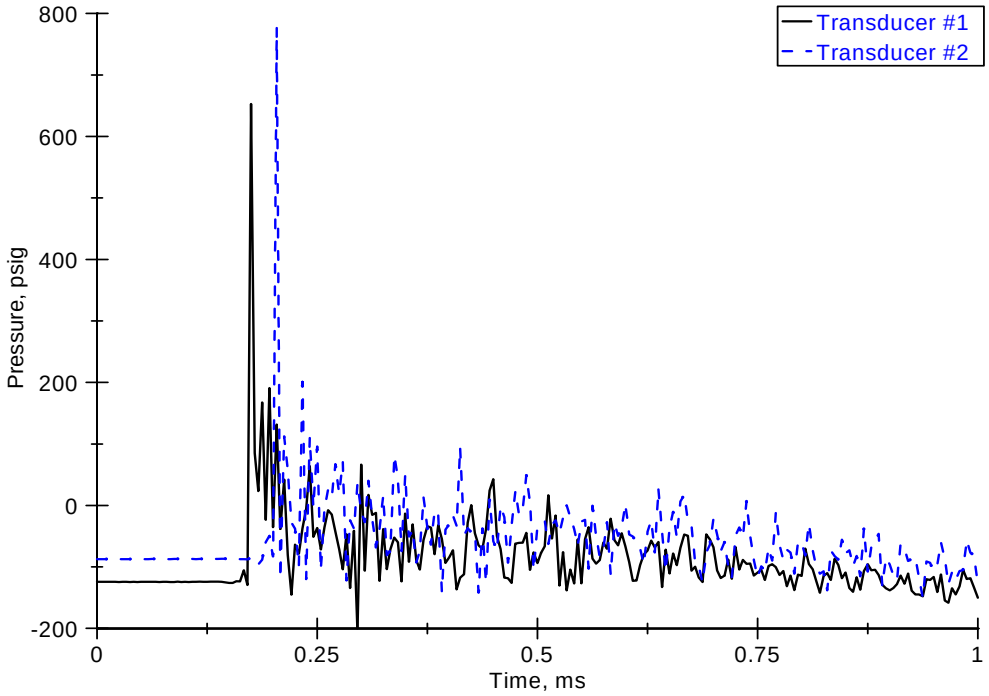

Figure 4.7. Pressure history for a detonation wave propagating by two transducers.

capture the time delay. Chauvenet's criterion can then be applied to this surface to eliminate bad data in the nonstationary crosscorrelation that occurs due to the limits of the varying window approaching the shock front of the disturbance.. The accepted data can then yield an estimate of the time delay as well as an estimate of the uncertainty of its value.

The nonstationary CCF is then normalized with repsect to the mean square values for the pair of signals to form the CCC. The CCC is defined as

$$\hat{\rho}_{xy}\left(L,U,i_{\tau}\right)=\frac{\hat{R}_{xy}\left(L,U,i_{\tau}\right)}{\sqrt{\hat{R}_{xx}\left(L,U,0\right)\hat{R}_{yy}\left(L,U,0\right)}} \tag{4.9}$$

The CCC has a range from -1 to 1, where the sign dictates if the signals are negatively or positively correlated. A CCC value of 1 signifies a perfect positive correlation; whereas a value of zero provides no correlation between the pair of records. An example of a nonstationary CCC output is shown in Fig. 4.8. The figure shows the

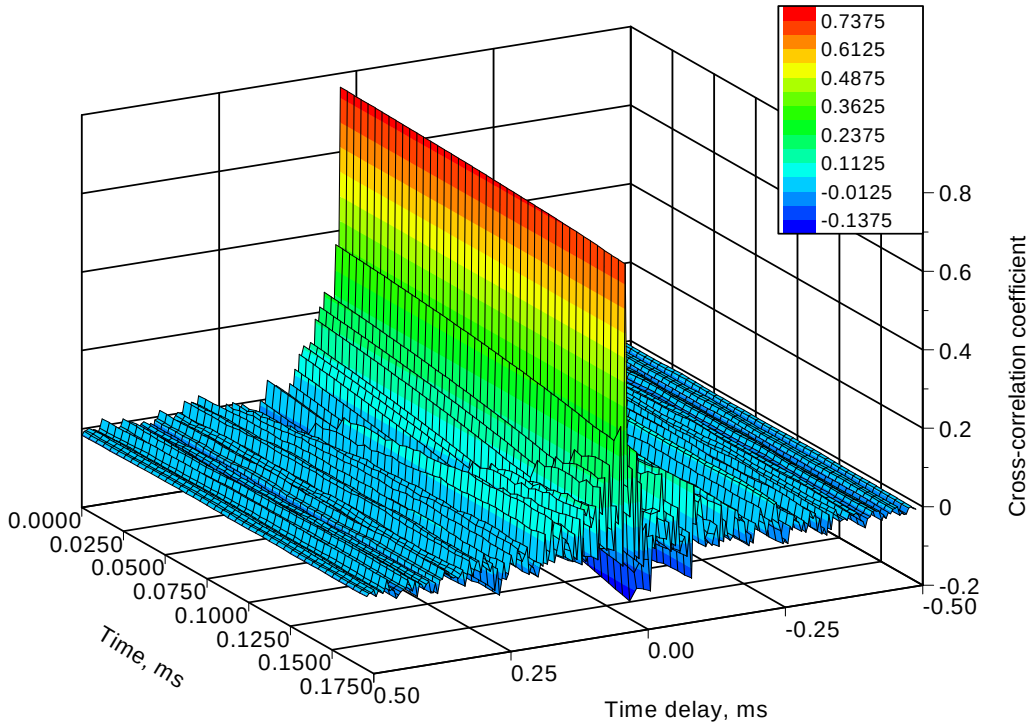

Figure 4.8. A nonstationary CCF for a constant U value.

nonstationary CCC for a varying time window that has a moving lower limit and a constant upper limit. The maximum value of the CCC signifies the time delay estimate for the given time window. The maximum value of the CCC is less than 0.8 that indicates a strong correlation. The signal is not perfectly correlated as noise is introduced as well as the propagation of the disturbance is not constant as it is an unsteady process.

The CCC also has a more defined peak for when the lower time limit is at a maximum value. However, as the lower time index approaches the disturbance, the peak value decreases slightly with an increase of the values surrounding the maximum CCC that can create an increase of uncertainty in the time delay estimate.

4.3 Hilbert Cross-Correlation Coefficient

A Hilbert transform of the CCC is another method for determining the time delay. The nonstationary Hilbert cross-correlation coefficient (HCCC) can be defined as

$$\widehat{\widetilde{\rho}}_{xy}(L, U, i_\tau) = \mathcal{H}\left[\hat{\rho}_{xy}(L, U, i_\tau)\right] \tag{4.10}$$

Unlike the CCC that uses the maximum correlated point for determining the time delay estimate, the time delay estimate for the HCCC is achieved at a zero-crossing between the highest and lowest peak. An example of the nonstationary HCCC output is shown in Fig. 4.9. The figure shows the same varying time window that was used in Fig. 4.8. The time delay estimate occurs at the zero-crossing between the maximum extreme (light red) and the minimum extreme (dark blue). Similar to the nonstationary CCC, the time delay estimate uncertainty increases as the time window approaches the shock front of the disturbance. The effect of the moving time window is believed to be minimized with the application of the nonstationary HCCC method. In Ref. [28], the HCCC method was proven in theory to provide a better time delay estimate due to the reduced variances by the zero-crossing. Similar to the nonstationary CCC, the nonstationary HCCC also produces a time delay surface for the varying window in time.

4.4 Envelope Correlation Coefficient

An envelope correlation coefficient (ECC) method was proposed in [13] that correlates the envelopes for the pair of signals. An envelope for a given signal is determined with the use of the Hilbert transform as shown in Eqn. (3.16b). The

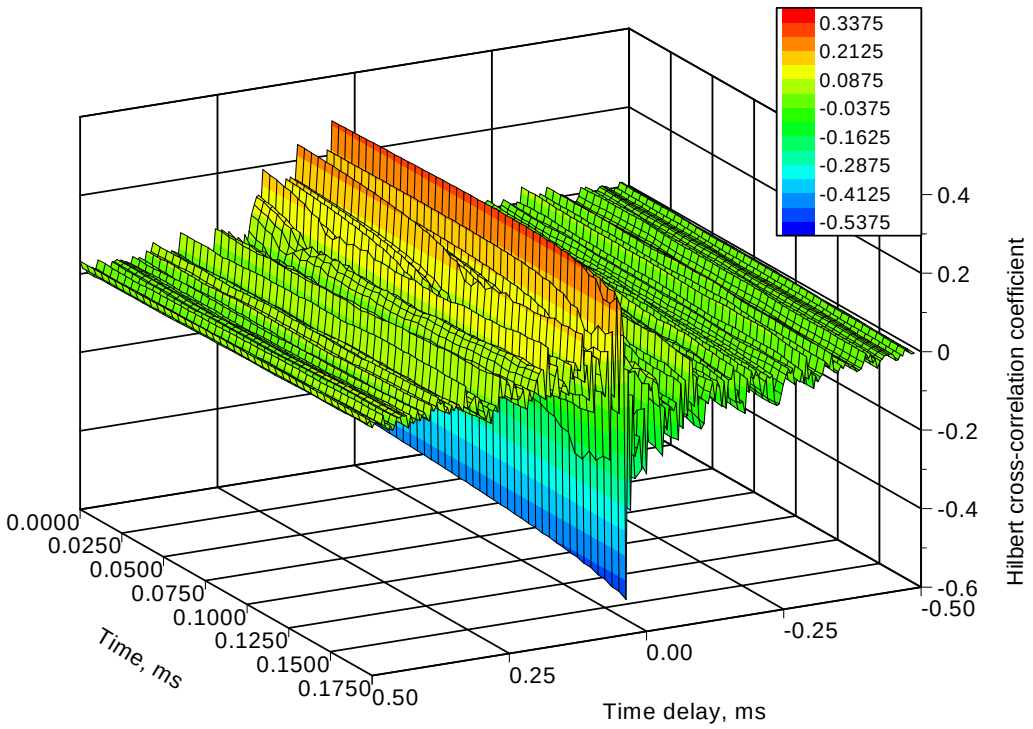

Figure 4.9. A nonstationary HCCF for a constant U value.

ECC uses the square of the envelope for each signal, and determines the CCC. The ECC is given by

$$\hat{\rho}_{uv}\left(L,U,i_{\tau}\right)=\frac{\hat{R}_{uv}\left(L,U,i_{\tau}\right)}{\sqrt{\hat{R}_{uu}\left(L,U,0\right)\hat{R}_{vv}\left(L,U,0\right)}} \tag{4.11}$$

where u and v are the squared envelopes of the signals x and y which are

$$u\left(t\right) = x\left(t\right)^{2}+\tilde{x}\left(t\right)^{2} \tag{4.12a}$$

$$v\left(t\right) = y\left(t\right)^{2}+\tilde{y}\left(t\right)^{2} \tag{4.12b}$$

It can be shown that the nonstationary ECC can also be represented as a function of the nonstationary CCC and HCCC as

$$\hat{\rho}_{uv}\left(L,U,i_{\tau}\right)=\hat{\rho}_{xy}^{2}\left(L,U,i_{\tau}\right)+\widehat{\widetilde{\rho}}_{xy}^{2}(L,U,i_{\tau}) \tag{4.13}$$

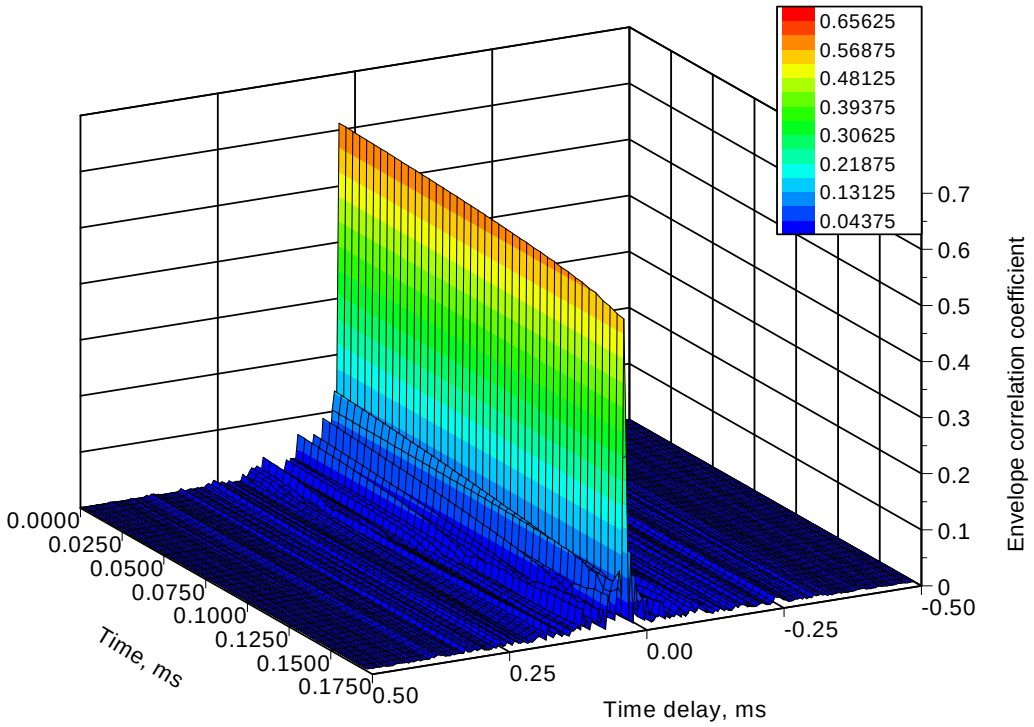

Figure 4.10. A nonstationary ECC for a constant U value.

An example of the nonstationary ECC is shown in Fig. 4.10. The advantage to this method is clearly shown by its more distinct peaks for the maximum correlated points. The maximum value compared to the nonstationary CCC has decreased, but the surrounding values have significantly reduced to create a better defined correlation function for determining the time delay estimate. Similar to the nonstationary CCC and HCCC, the ECC value decreases as the limit of the lower time window approaches the disturbance.

4.5 Cross-Spectral Density Phase

Another technique used for determining the propagation time for a disturbance is with the nonstationary cross-spectral density phase (NCSDP) method. Unlike the previous methods that determine the time delay in the time domain, the NCSDP

utilizes the frequency spectrum for providing an estimate of the time delay for the pair of signals. The NCSDP used is a modified version of the original cross-spectral density technique in [13].

The cross-spectral density is obtained by applying the Fourier transform on the cross-correlation function and is given by

$$S_{xy}(f) = \int R_{xy}(\tau)\, e^{-j2\pi f\tau} d\tau \tag{4.14}$$

The cross-spectral density can also be written in complex polar notation as

$$S_{xy}(f) = |S_{xy}(f)|\, e^{-j\theta_{xy}(f)} \tag{4.15}$$

where the phase angle is related to the time delay. The relationship between the phase angle and the time delay is

$$\theta_{xy}(f) = 2\pi f \tau(f) \tag{4.16}$$

For nondispersive signals, the time delay remains constant for all frequencies; thus, the phase angle remains linear throughout the spectrum.

The double-sided nonstationary cross-spectral density function presented in [13], which is a slight alteration of the original cross-spectral density function of Eqn. (4.14), is given by

$$W_{xy}(f,t) = \int R_{xy}(\tau,t)\, e^{-j2\pi f\tau} d\tau \tag{4.17}$$

Equation (4.17) is discretized to yield

$$\widehat{\mathcal{W}}_{xy}(k,L,U) = \sum_{i_\tau=-(N-1)}^{N-1} \hat{R}_{xy}(L,U,i_\tau) \exp\left(-j\frac{2\pi k i_\tau}{N}\right) \tag{4.18}$$

Since the discrete Fourier transform algorithm FFT starts its lower bound index at zero as shown in Eqn. (3.3), the discrete version of the NCSDP has to be altered

to satisfy this condition. The modified discrete version of the nonstationary cross-spectral density function is

$$\widehat{\mathcal{W}}_{xy}(k,L,U) = \sum_{m=0}^{2N-2} \hat{R}_{xy}(L,U,m) \exp\left(-j\frac{2\pi km}{N}\right) \tag{4.19}$$

where

$$m = i_\tau + N - 1 \tag{4.20}$$

The phase angle can then be computed by

$$\hat{\theta}_{xy}(k,L,U) = \tan^{-1}\left[\frac{\Im\left[\widehat{\mathcal{W}}_{xy}(k,L,U)\right]}{\Re\left[\widehat{\mathcal{W}}_{xy}(k,L,U)\right]}\right] \tag{4.21}$$

where the quadrant is determined according to the sign of the imaginary and real components.

Similar to the stationary case, the cross-spectral density can also be written in complex polar notation as

$$\widehat{\mathcal{W}}_{xy}(k,L,U) = \left|\widehat{\mathcal{W}}_{xy}(k,L,U)\right| e^{-j\theta_{xy}(k,L,U)} \tag{4.22}$$

The time delay can then be related to the phase angle for a nondispersive propagation as

$$\hat{\theta}_{xy}(k,L,U) = 2\pi km\Delta f\Delta t \tag{4.23}$$

which after substitution for m is

$$\hat{\theta}_{xy}(k,L,U) = 2\pi k\Delta f\left[i_\tau\Delta t + (N-1)\Delta t\right] \tag{4.24}$$

Substitution of Eqns. (3.8), (4.3) and (4.4) into the discrete phase angle in Eqn. (4.24) forms

$$\hat{\theta}_{xy}(f,t) = 2\pi f\left[\hat{\tau} + \frac{(N-1)}{f_s}\right] \tag{4.25}$$

which can be used as a comparison to the analog phase angle.

The discretized version of the phase angle has additional terms that are not present in the analog version in Eqn. (4.16). These additional terms present a problem in the time delay estimate. For simplicity, a case with no time delay is considered and the phase angle reduces to

$$\hat{\theta}_{xy}(f,t) = 2\pi f\left(\frac{N-1}{f_s}\right) \tag{4.26}$$

The discrete version of the phase angle is

$$\hat{\theta}_{xy}(k,L,U) = 2\pi k\Delta f\left(\frac{N-1}{f_s}\right) = 2\pi k\frac{f_s}{N}\left(\frac{N-1}{f_s}\right) \tag{4.27}$$

that simplifies to

$$\hat{\theta}_{xy}(k,L,U) = 2\pi k\left(\frac{N-1}{N}\right), \quad k = 0,1,\ldots,N-1 \tag{4.28}$$

In the limit as the sample size approaches infinity, the phase angle estimate approaches a multiple of 2π. This represents an equivalent result for an autocorrelation function. The autocorrelation function represents the simple case of no time delay. With a positive time delay, the phase angle will exceed 2π, which creates an uncertainty of 2π in the phase estimate. The 2π uncertainty is known as phase aliasing. Due to phase aliasing, the time delay estimate is impossible to determine directly. An example of phase aliasing is shown in Fig. 4.11. In this figure, the actual phase angle (solid black line) is an infinite sawtooth function. The discrete phase aliased representation of this data is shown as a red dashed-line with markers. Since the discrete phase angle is sampled at a rate that exceeds the range of the phase angle $-\pi \leq \hat{\theta}_{xy} \leq \pi$, the true phase to frequency relationship is lost. Unfortunately, modifying the sampling rate or the amount of samples acquired will be unable to prevent phase aliasing.

A zoom transform is used to overcome phase aliasing. The phase-frequency relationship remains the same with the application of a zoom transform, but the zoom

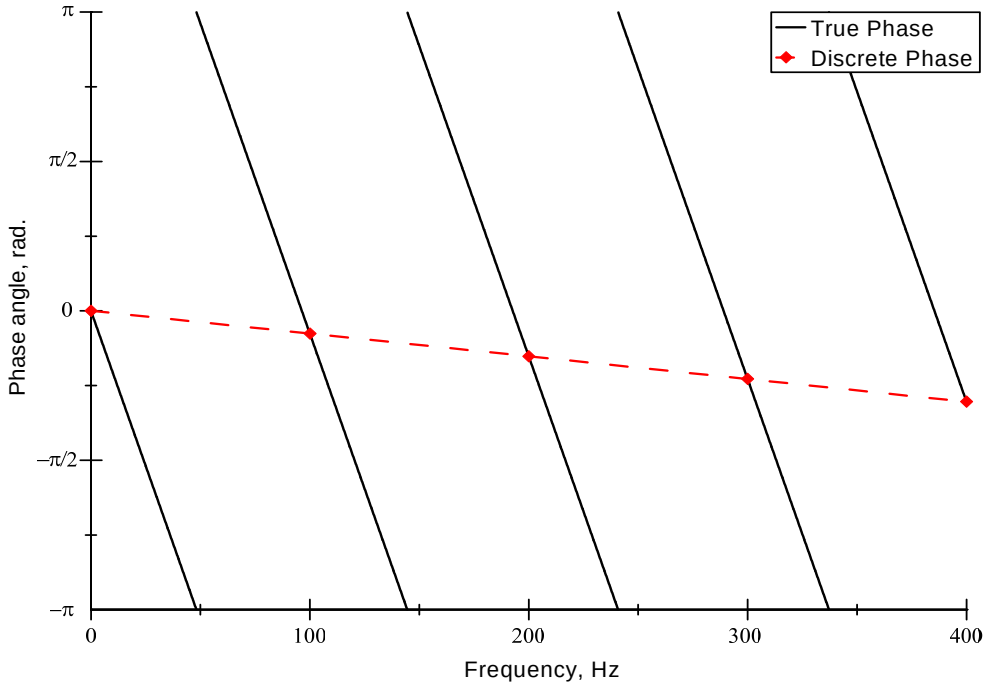

Figure 4.11. An example of phase aliasing that is caused by the discretizing the equations.

transform now improves the frequency resolution. It is recommended to improve the spectral resolution by a factor of four. This recommendation is based off using the maximum time delay value, and setting the phase equation equal to π. The process for determining the factor is derived from Eqn. (4.25), and is the following:

$$\hat{\theta}_{xy} = 2\pi k \Delta f \left(f_{ratio}\right) \left(\frac{N}{f_s} + \frac{N-1}{f_s}\right) = 2\pi k f_{ratio} \left(\frac{f_s}{N}\right) \left(\frac{2N-1}{f_s}\right) \tag{4.29a}$$

$$\hat{\theta}_{xy} = 2\pi k f_{ratio} \left(\frac{2N-1}{N}\right) \approx 4\pi k f_{ratio} \tag{4.29b}$$

Setting the phase angle and the frequency index equal (k) to π and one respectively reduces Eqn. (4.29b) to

$$\pi \approx 4\pi f_{ratio} \tag{4.30a}$$

$$f_{ratio} = 1/4 \tag{4.30b}$$

The frequency ratio is defined as

$$f_{ratio} \equiv \Delta f_{zoom}/\Delta f \tag{4.30c}$$

where Δf_{zoom} is the frequency resolution of the zoom transform.

4.5.1 Phase Uncertainty

The discretized phase angle Eqn. (4.25) is an exact solution, which only occurs in an ideal case with a very high SNR with the signals being highly coherent. Since this is not the case most of the time, a way of estimating the phase uncertainty needs to be determined. A way of determining the phase uncertainty was proposed in [12] and is given by

$$\Delta\hat{\phi}_{xy}(f) \approx \sin^{-1}\left[\frac{\sqrt{1-\gamma_{xy}^2(f)}}{|\gamma_{xy}(f)|\sqrt{2n_d}}\right] \tag{4.31}$$

According to Eqn. (4.31), the phase uncertainty can be reduced by having highly coherent signals or by using a large number of averages. Tables for several numbers of averages at various coherence values are provided in Table 4.2. Referring to Table 4.2, for signals with low coherence values a large number of averages are needed to improve the phase estimate. For example, if the desired phase uncertainty is set to 0.033 radians, a coherence value of 0.9 can achieve the phase uncertainty with 50 averaged records. A much larger number of records (200 in this example) are needed for the exact same uncertainty in the phase angle at a lower coherence value of 0.7.

Table 4.2. The phase uncertainty in radians for various coherence values

	Number of averages (n_d)				
γ^2	1	10	50	100	200
0.1	2.121	0.671	0.300	0.212	0.150
0.3	1.080	0.342	0.153	0.108	0.076
0.5	0.707	0.224	0.100	0.071	0.050
0.7	0.463	0.146	0.065	0.046	0.033
0.9	0.236	0.075	0.033	0.024	0.017
1.0	0.000	0.000	0.000	0.000	0.000

4.5.2 Coherence Function

The uncertainty in the phase estimate is dependent on the coherence between the signals. The coherence function is a measure of degree of correlation between the signals in the frequency domain [29]. The coherence function is

$$\gamma_{xy}^2(f) = \frac{|S_{xy}(f)|^2}{S_{xx}(f)\,S_{yy}(f)} \tag{4.32}$$

that is within $0 \leq \hat{\gamma}_{xy} \leq 1$ throughout the spectrum. A coherence value of zero indicates pure noise that is uncorrelated. A coherence value of unity signifies perfect correlation. Typically the coherence of the signals is less than one due to noise present in the given measurement, resolution bias errors in the spectral estimates, a nonlinear relation between the given signals, or the second sensor is receiving other inputs that were not previously present for the initial sensor [12]. An example of a coherence function is shown in Fig. 4.12. It is also noted in [30] that frequencies near the structures resonant frequency have highly incoherent signals due to the amplification of the noise.

4.5.3 Coherence Limit

Since the coherence of the signals influences the uncertainty in the phase angle estimate, a coherence limit has to be imposed that discards areas of low coherence.

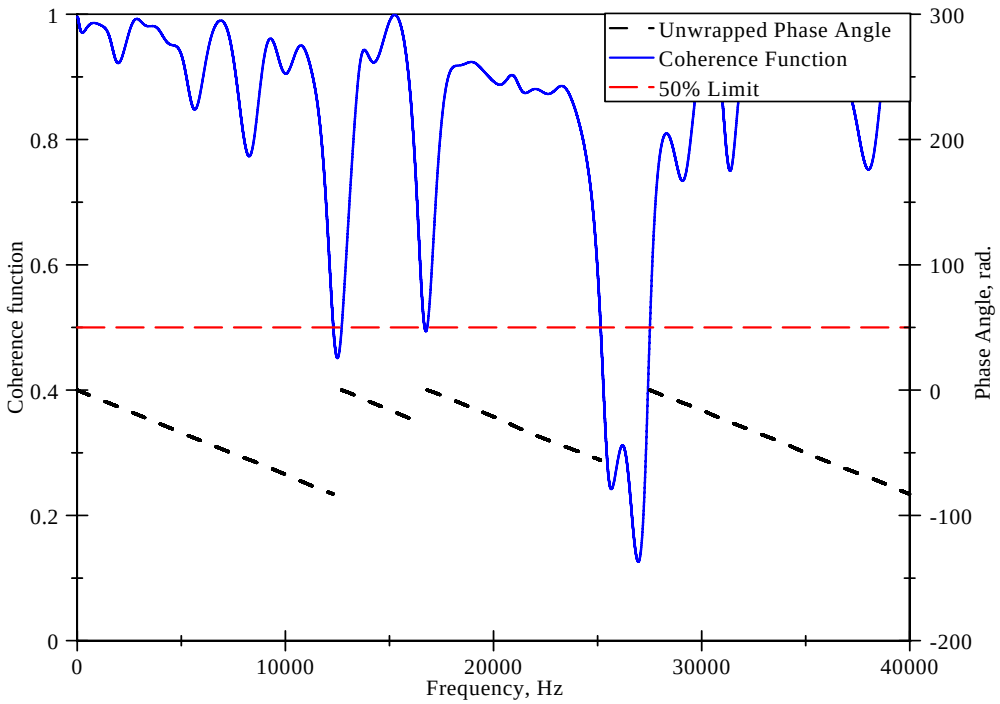

Figure 4.12. An example of the phase angle being unwrapped according to the coherence of the signals and coherence limit.

An example of this coherence limit is provided in Fig. 4.12. A 50% coherence limit was used, and it is recommended not to use a more generous coherence limit as the 50% already signifies a very poor SNR.

4.5.4 Weighting Function

A weighting function is needed for transforming the correlation function from the time to the frequency domain. The weighting function is used mainly for two reasons. It is needed to reduce the spectral leakage that degrades the coherence between the signals, and to smooth the edges that may be erratic due to the limited information near the edge of the defined lower and upper bounds.

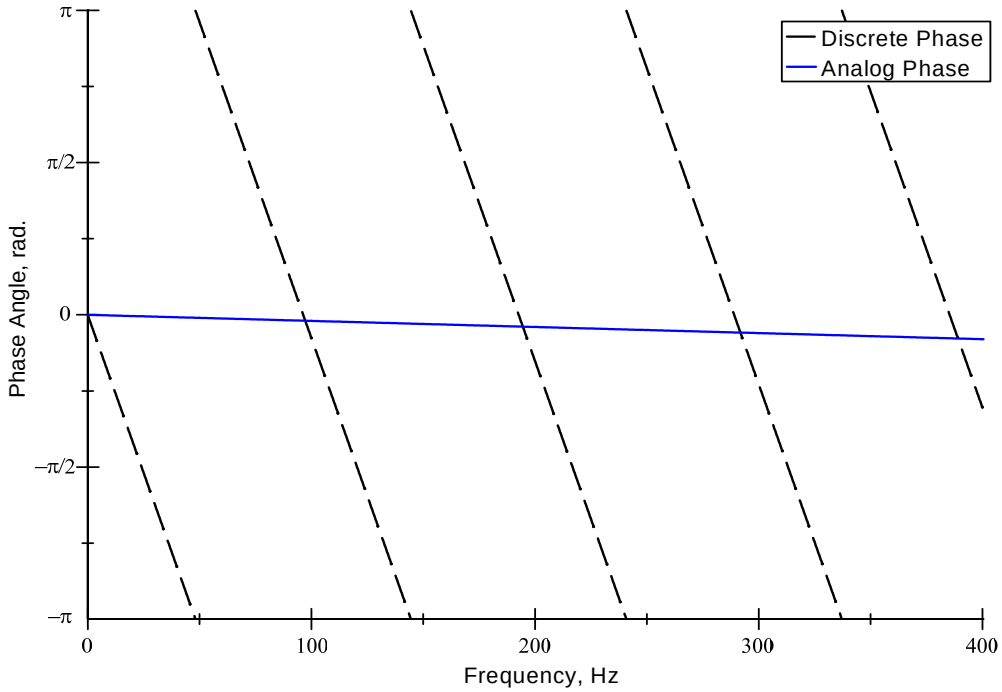

Figure 4.13. An example of the phase-frequency relationship difference between the analog and discrete phase estimates for the same time delay signal as Fig. 4.11.

4.5.5 Unwrapping Phase

Typically in the analog version, the phase angle does not need to be unwrapped because it has an adequate amount of samples before a phase jump. For the discrete phase version, leaving the phase angle wrapped leads to few samples before a phase jump, which increases the error in the estimate for determining the slope of the phase angle. The difference in the slopes between the analog and discrete version is shown in Fig. 4.13. The discretized version has a much steeper slope than the analog version for the same time delay. The samples for the discrete version also decrease depending on the coherence of the signals at a particular frequency. For this reason, a weighted-resetting unwrap of the phase angle method was developed.

The weighted-resetting unwrap of the phase angle method consists of unwrapping the phase angle continuously till the coherence value drops below the coherence

limit, and once the limit has been crossed the phase angle is reset and offset to have the initial phase angle at zero. All of the values below the coherence limit are discarded. An example of the result of applying this method is provided in Fig. 4.12. Referring to Fig. 4.12, the phase angle (dashed black line) is unwrapped multiple times and is reset back to zero every time the coherence (solid blue line) of the signals drops below the coherence limit (dashed red line). With a less tolerant coherence limit, more portions of the phase angle will be reset with smaller samples due to the increase of discarding of values below the coherence limit.

4.5.6 Linear Fit

A linear least squares fit (LLSF) was applied to extract the phase-frequency relationship in order to determine the time delay. Since there exists a possibility to have multiple portions of the unwrapped phase as shown in Fig. 4.12. that contains four unwrapped portions, a weighting scheme was used based off the number of samples for a given segment. For this method, the sections for 0–12 and 28–40 kHz in Fig. 4.12 would be weighted the most as they contain a larger portion of frequencies above the coherence limit, while the section 13 to 15 kHz would have less significance in the overall determination of the phase-frequency relationship since it contains the least amount of samples. This process is continued for each time step, which generates a single phase-frequency relationship for an individual time step.

4.5.7 Time Delay

Determining the time delay between the given signals with Eqn. (4.24) is problematic for signals with poor coherence. A more appropriate method would utilize the phase-frequency relationship for the autospectral density functions in determining the time delay. The time delay can be determined by computing the average

difference between the phase-frequency relationships for the cross-spectral and autospectral density functions. This method does not require previous knowledge of the sampling properties and is given by

$$\widehat{\bar{\tau}}_{xy}(t) = \frac{\left(\left.\frac{d\theta}{d\omega}\right|_{xx} - \left.\frac{d\theta}{d\omega}\right|_{xy}\right) + \left(\left.\frac{d\theta}{d\omega}\right|_{yy} - \left.\frac{d\theta}{d\omega}\right|_{xy}\right)}{2} \tag{4.33}$$

The estimate in Eqn. (4.34) is now used to determine the time delay for each individual time step for the nonstationary signals. Chauvenets criterion is then applied to eliminate outliers in order to prevent bad estimates that are highly influenced by the edge of the window near the disturbance.

4.6 Cross-spectral Density Phase Version 2

A more common variation of the CSDP technique is to bypass the cross-correlation function by applying the Fourier transformation directly to the raw data. The technique described here will be referred to as CSDP-2. The time-averaged cross-spectral density function is defined as

$$\bar{S}_{xy}(f) = \lim_{T\to\infty} \frac{1}{T} \int_0^T W_{xy}(f,t)\, dt \tag{4.34}$$

The time averaged cross-spectral density function can also be represented as

$$\bar{S}_{xy}(f) = \mathcal{F}\left[\bar{R}_{xy}(\tau)\right] \tag{4.35}$$

where

$$\bar{R}_{xy}(\tau) = \lim_{T\to\infty} \frac{1}{T} \int_0^T R_{xy}(\tau,t)\, dt \tag{4.36}$$

Similar to the convolution, the autocorrelation and cross-correlation function can be determined by the inverse Fourier transform of the signals in the frequency domain. Since the cross-spectral density function is the Fourier transform of the

cross-correlation function, the time averaged cross-spectral density function can then be defined as

$$\bar{S}_{xy}(f) = \frac{1}{T} E\left[X^*(f)\, Y(f)\right] \tag{4.37}$$

The time averaged cross-spectral density function can be discretized for the entire ensemble as

$$\widehat{\bar{S}}_{xy}(k) = \frac{1}{n_d N \Delta t} \sum_{i=1}^{n_d} X_i^*(k)\, Y_i(k) \tag{4.38}$$

The advantage to Eqn. 4.37 is the significant reduction in the amount of computations required to determine a proper estimate for the time delay.

Since the raw data is now being transformed directly to the frequency domain by a FFT, a weighting function must be applied to the raw data. The weighting function is needed to provide a better estimate. The selection of the weighting function is determined by the random signal being analyzed, and an exponential window function was selected since it provides the best results for impact signals that decay.

Similar to the CCCF, the CSDP-2 has a moving window frame due to the signals being nonstationary. The weighted data is then transformed to the frequency domain for each case, and averaged to provide an estimate of the cross-spectral density function. The coherence function is then determined, and used to eliminate the highly incoherent frequency components in the signals. The phase angle can then be computed by

$$\widehat{\bar{\theta}}(k) = \tan^{-1}\left[\frac{\Im\left(\widehat{\bar{S}}_{xy}\right)}{\Re\left(\widehat{\bar{S}}_{xy}\right)}\right] \tag{4.39}$$

The phase angle for the CSDP-2 method does not require an alteration to the phase-frequency relationship like the CSDP method, and follows the relationship provided

in Eqn. 4.16. Similar to the CSDP method, the CSDP-2 may require the application of the zoom transform to avoid phase aliasing. The discretized phase angle is

$$\widehat{\bar{\theta}} = 2\pi k i_\tau \Delta f \Delta t \tag{4.40}$$

which has a range $-2\pi < \widehat{\bar{\theta}} < 2\pi$. The maximum value for the range for the CSDP-2 is half the maximum value for the CSDP method, so the amount of computations for the zoom transform is reduced. Similar to the CSDP method, the phase angle is unwrapped according to the coherence function. A LLSF is then applied to determine an estimate of the time delay between the signals.

4.7 Wavelet Cross-Correlation Function

Another method for determining the time delay between a pair of signals is with a wavelet cross-correlation coefficient (WCCC) as described in [11]. The WCCC method determines the correlation between the pair of signals in the frequency domain like the nonstationary CSDP method, but it does not depend on the phase information for determining the time delay estimate. The WCCC utilizes the wavelet coefficients to determine on a scale basis the correlation between the pair of signals. The WCCC is

$$\widehat{WR}_{xy}(a,\tau) = \frac{\widehat{WC}_{xy}(a,\tau)}{\sqrt{\widehat{WC}_{xx}(a,0)\,\widehat{WC}_{yy}(a,0)}} \tag{4.41}$$

, where the wavelet cross-correlation function is defined as

$$\widehat{WC}_{xy}(a,\tau) = \lim_{T\to\infty} \frac{1}{T} \int_{T/2}^{T/2} CWT_x^*(b,a)\, CWT_y(b+\tau,a)\, db \tag{4.42}$$

Similar to the previous correlation coefficients, the WCCC has a range from $-1 \leq \widehat{WR}_{xy} \leq 1$ where one signifies a strong correlation between the pair of signals. The unbiased WCCC function can be discretized and is

$$\widehat{WC}_{xy}(a, i_\tau) = \frac{1}{N - |i_\tau|} \sum_{i=0}^{N-1} CWT_x(i, a) CWT_y(i + i_\tau, a), \quad i_\tau = -(N-1), -(N-2), \ldots, N-2, N-1 \tag{4.43}$$

The WCCC provided in Eqn. (4.41) is a general equation for the correlation function. The WCCC has many variations dependent on the mother wavelet utilized to transform the pair of signals. Each mother wavelet will compute different wavelet coefficients that provide similar results, and may also provide added detail depending on how well the particular basis function models the signal. A Haar wavelet for transducer # 1 from the detonation wave record in Fig. 4.7 is provided in Fig. 4.14. Referring to Fig. 4.14, the Haar wavelet is able to capture the von Neumann spike as all the frequencies (scales) are excited when the detonation wave arrives at the given sensor. The influence of the expansion is small compared to the von Neumann spike for all scales, and the expansion appears to have an effect on the COI produced by the spike.

The figure shows a contour plot of the WCCC for the signals provided in Fig. 4.17. The time delay estimate for each scale occurs at the largest WCCC value represented in red. For low scales (high frequencies), a more defined correlation function is provided because of the better time localization at lower scales (high frequencies). A Morlet wavelet function for the same transducer is provided in Fig. 4.16. Referring to Fig. 4.16, the Morlet wavelet is also able to capture the von Neumann spike. The Morlet wavlet shows multiple areas of significance due to shape of the basis function. The figure also shows the maximum wavelet value varying slightly in the vicinity of the von Neumann spike. A possible reason for the wave

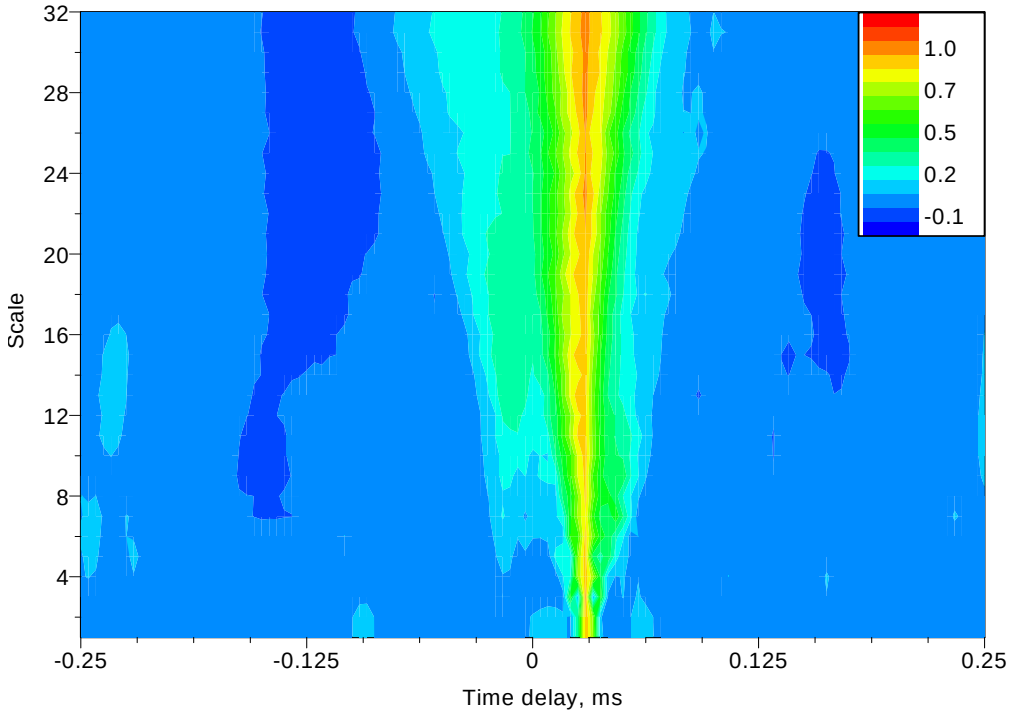

Figure 4.14. The Haar wavelet scalogram for transducer # 1 in Fig. 4.7.

like motion with increasing scale for the maximum value is due to the reduced time localization from the Morlet wavelet.

The figure shows a contour plot of the Morlet WCCC for the signals provided in Fig. 4.17. The Morlet WCCC also identifies the correlation of the von Neumann spike for both the signals, as a strong WCCC exists at the appropriate time delay for all scales. However, there also exists a strong correlation between the signals surrounding the area of the correlated von Neumann spike at several scales. One such incident occurs at a scale from 8 to 10 (in light orange) on the right-hand side of the frequently dominant time delay for all scales. The anomaly occurs due to the combination of the COI from the von Neumann spike as well as a correlated frequency band during the expansion. Since the correlated frequency band for the expansion is limited to a small scale range, the estimate of the time delay is not significantly affected.

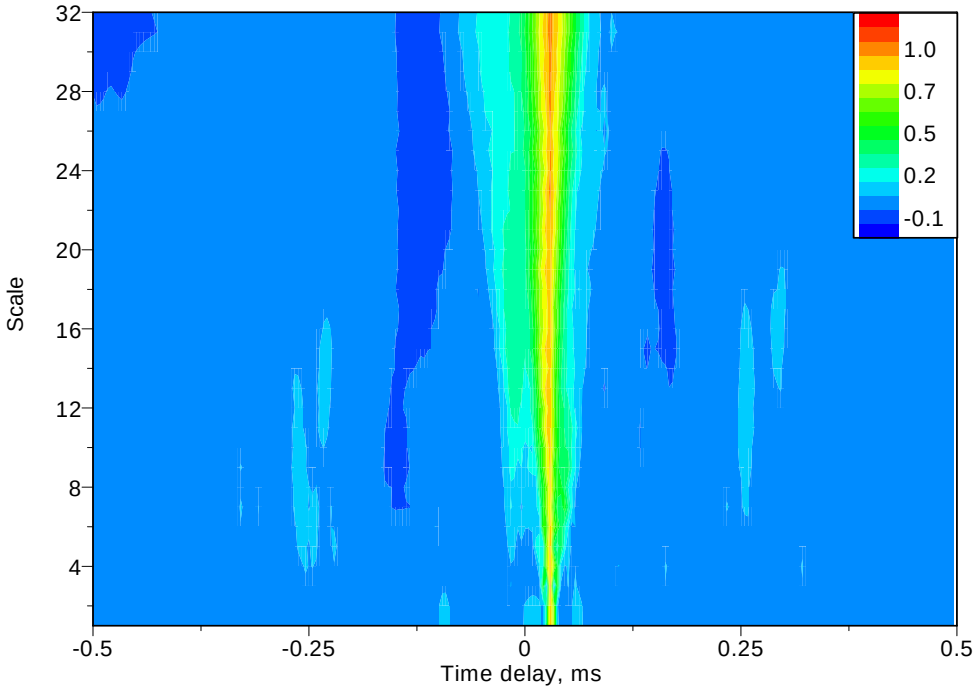

Figure 4.15. The Haar WCCC scalogram for a detonation wave record.

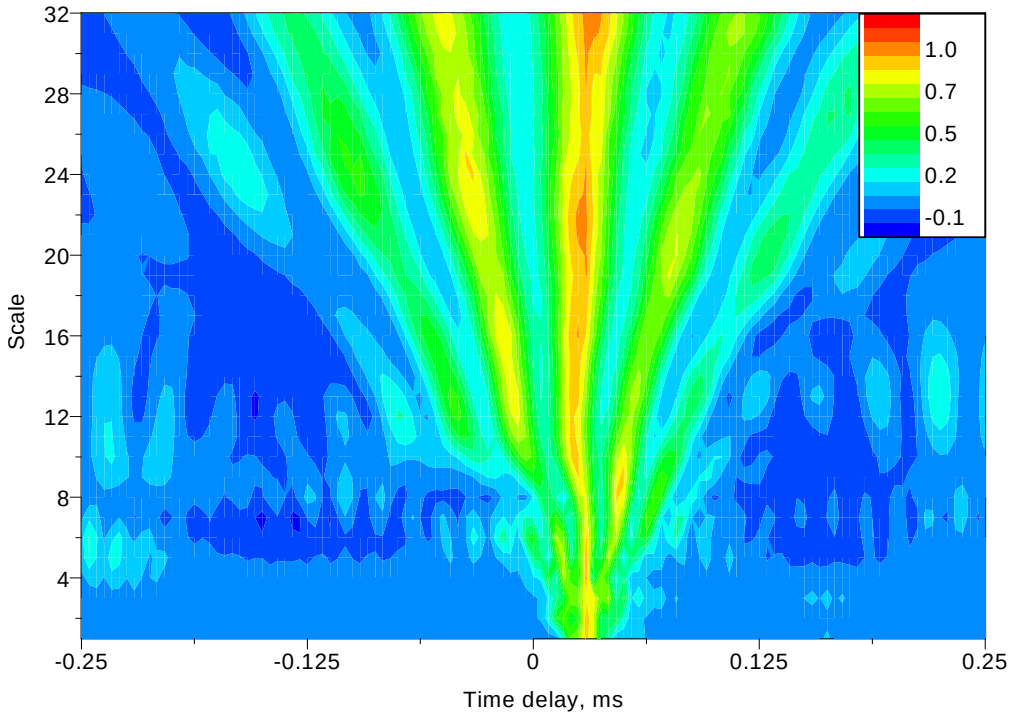

Figure 4.16. The Morlet wavelet scalogram for transducer # 1 in Fig. 4.7.

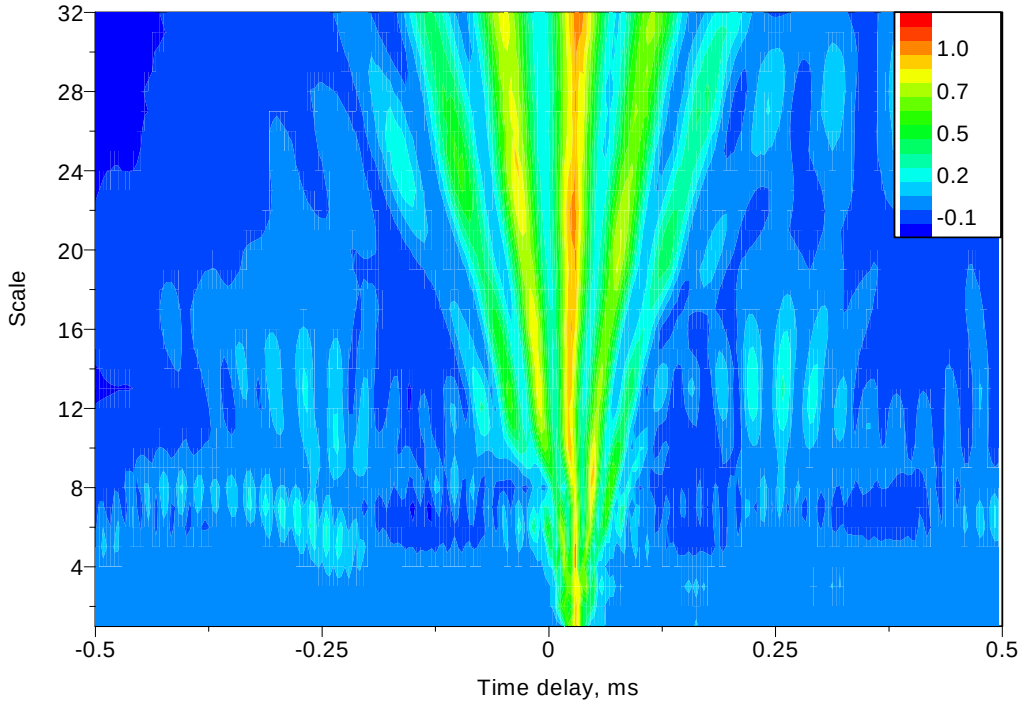

Figure 4.17. The Morlet WCCC scalogram for a detonation wave record.

An advantage to the application of the WCCC is the ability to determine the time delay for various frequency bands. Since the WCCC can determine the time delay for various frequency bands, the WCCC provides the ability to analyze dispersive signals that is difficult with the NCSDP method.

CHAPTER 5

RESULTS

5.1 Shock Tube Results

A comparison of the results for the nonstationary methods are presented in this section. The methods will be used to determine the propagation time for a shock tube experiment. The shock tube consisted of a driver and a driven section that both had an inner diameter of one inch. The driven section was filled with air at atmospheric pressure, while the driver section was filled with air at approximately 150 psig. Both tubes were sealed. Therefore, when the diaphragm separating the driver and driven sections broke, multiple shock reflections resulted which eventually died down. Thus, a nonstationary process was set up. This is clearly seen in the pressure histories obtained from four transducers located in the driven section, Fig. 5.1.

5.1.1 Incident Shock

The time delay estimates for the incident shock wave, that is, the very first set of waves in Fig. 5.1, are presented in Table 5.1. The table shows each particular method's mean and standard deviation estimates of the time delay for the incident shock wave. The TOF estimate was determined by the difference in the time between the peak of the propagating shock wave for each sensor. The TOF method has no statistical variance in time. The data show an increase in the time delay between transducers 1–2 and between transducers 3–4. This may be because the shock wave is slowing down due to viscous damping as it propagates along the length of the tube.

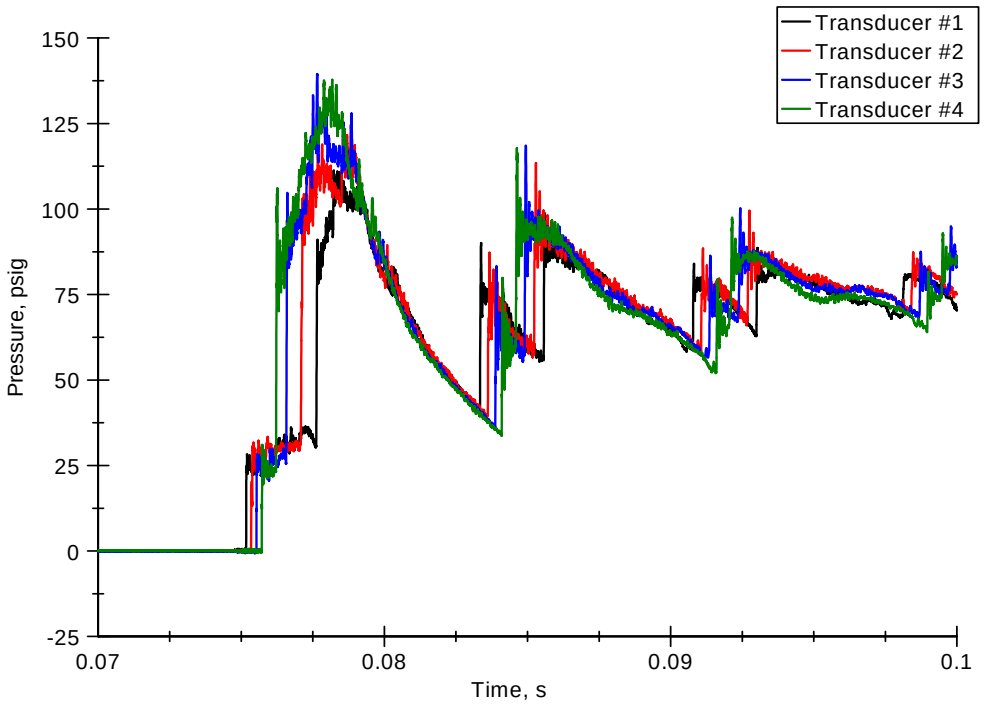

Figure 5.1. Pressure history for a shock tube experiment.

Table 5.1. Time delay values for the incident shock wave using various methods

	Transducers 1–2		Transducers 2–3		Transducers 3–4	
Method	$\bar{\tau}$, ms	$\sigma(\tau)$, ms	$\bar{\tau}$, ms	$\sigma(\tau)$, ms	$\bar{\tau}$, ms	$\sigma(\tau)$, ms
TOF pk-pk	0.148	–	0.158	–	0.190	–
NCCC	0.175	0.003	0.151	0.003	0.181	0.003
NHCCC	0.117	0.003	0.087	0.011	0.120	0.005
NECC	0.177	0.001	0.171	0.055	0.191	0.004
NCSDP	0.055	0.124	0.082	0.087	0.063	0.092
NCSDPE	0.080	0.020	0.145	0.020	0.077	0.034
CSDP-2	0.143	0.054	0.110	0.082	0.121	0.089
CSDP-2E	0.123	0.059	0.080	0.081	0.101	0.097
WCCC-Haar	0.175	0.001	0.188	0.001	0.184	0.002
WCCC-Morlet	0.190	0.020	0.172	0.021	0.187	0.008
WECC-Haar	0.175	0.001	0.188	0.001	0.184	0.002
WECC-Morlet	0.190	0.020	0.172	0.021	0.187	0.008

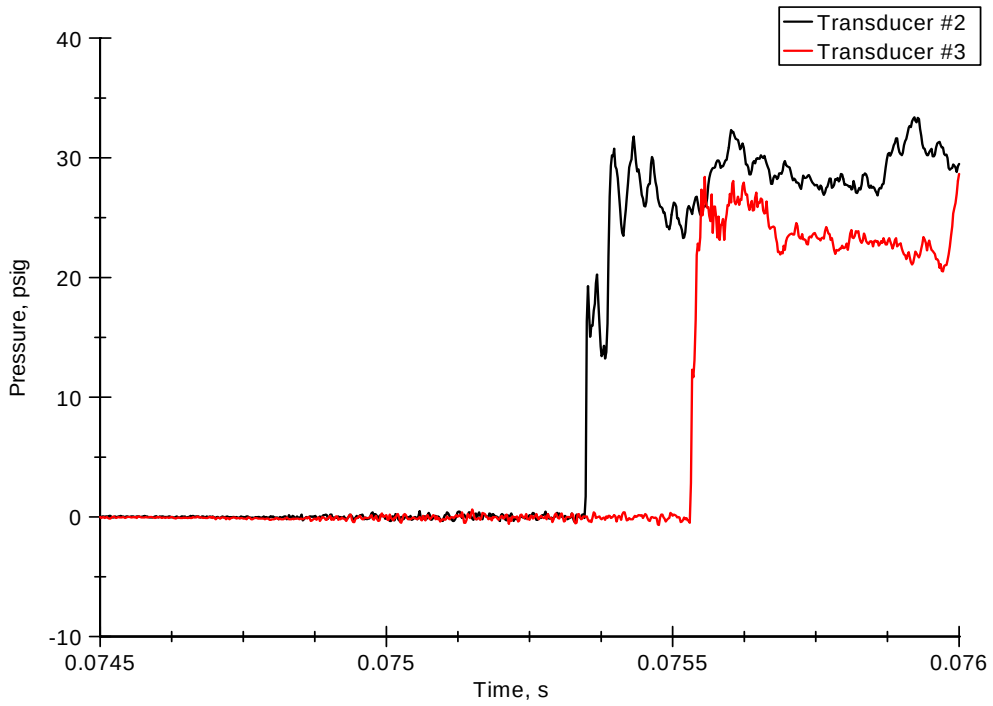

Figure 5.2. Pressure history window for incident shock wave for transducers # 2 and 3.

The pressure history for transducers 2 and 3 is provided in Fig. 5.2. The figure shows the time window for these transducers, from 0.0745 to 0.076 s, that was used to determine the time delay estimate for the propagating incident shock wave.

The NCCC for the incident shock past transducers 2 and 3 is represented by a contour plot where red and blue indicate the maxima and minima respectively. The NCCC contour plot is shown in Fig. 5.3. The ordinate represents the varying lower time index L, which corresponds to the time scale of the pressure history shown in Fig. 5.2. The upper time index was kept constant at the maximum time index value for plotting purposes. The abscissa represents an imposed time delay between the signals. The time delay for a given lower time index is determined by the maximum correlated value. The maximum value is graphically represented by the color closest to red in the color spectrum. Referring to Fig. 5.3, the correlation peak appears to be

broad as it has wide bands. The broad peak can present a problem as the lower time index (ordinate) approaches the shock front. As the lower time index approaches the disturbance, less information is used to determine the correlation between the signals. Since less information is utilized at larger values for the lower time index, the broad peaks become less distinct. The problem arises when the broad peak approaches a plateau-like surface that does not have a well-defined peak. The time delay estimate becomes susceptible to noise and smaller correlated events, which introduces incorrect time delay estimates. The CCC is clearly varying with time (lower time index) as shown in Fig. 5.3. The correlated peak is also shown to become less distinct as the time (lower time index) approaches the shock front. Even though the correlated peak is reducing in magnitude near the shock front, the peak value remains relatively unphased by the varying time (lower time index) since the time delay estimate has a small variance. The time delay estimate for the NCCC can be seen to be close to the arbitrary TOF estimate.

The result for transducers 2–3 with the NHCCC method is displayed in Fig. 5.4. The axes for the NHCCC coutour are similar to the ones used for the NCCC plot. The only difference is that the contours represent the NHCCC. The time delay estimate is determined at the zero crossing between the maxima shown in red and the minima shown in blue. Isolines and the contour values were added to the figure to help identify graphically the zero crossing. The zero crossing contour remains fairly constant with time delay. However, as the lower time index (ordinate) approaches the shock front, the zero crossing varies significantly towards zero time delay. The strong fluctuations recorded by transducer 2 appears to influence the time delay estimate for the NHCCC. These flucuations are providing a stronger correlation with the signal from transducer 3 than the initial shock front from transducer 2. The time delay estimate is reduced because of the fluctuations occurring between the two shock

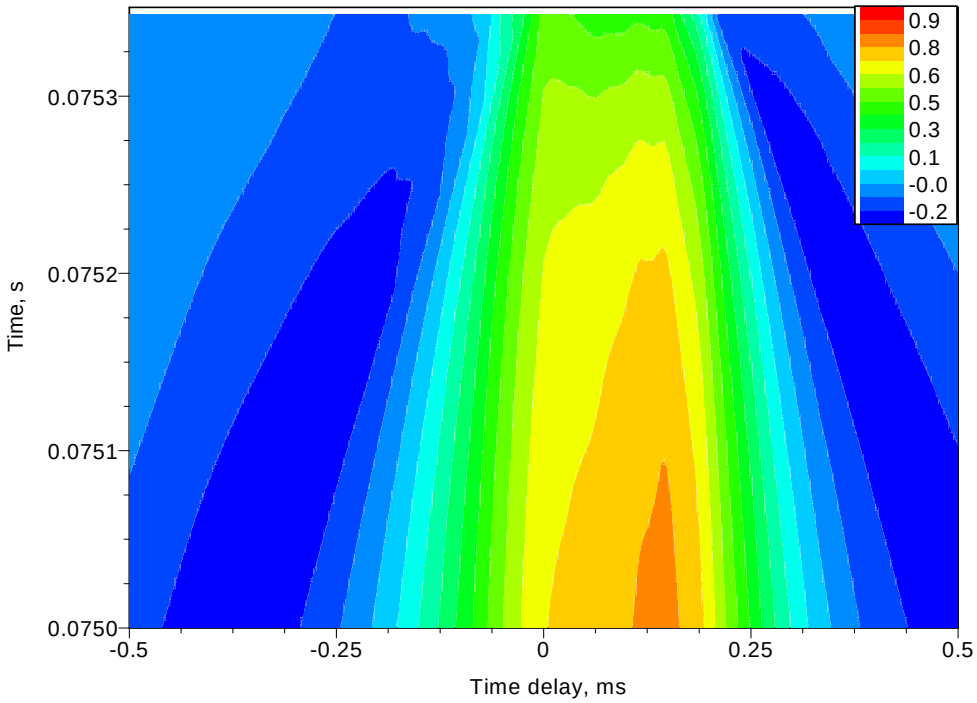

Figure 5.3. The NCCC result with a constant upper time limit for the incident shock wave in Fig. 5.2.

fronts, as shown in Fig. 5.2. Thus, for this case, the NHCCC may be a bad choice for determining the time delay estimate as it is influenced by the oscillations after the shock front.

The NECC result for transducers 2–3 are shown in Fig. 5.5. The abscissa and ordinate remain the same as the axes used for the NCCC and NHCCC methods. The envelope correlation function appears more defined than the correlation function provided by the NCCC method in Fig. 5.3 because the peak is more distinct. Since the envelope correlation function contains a faster roll-off surrounding the peak value, several other peaks that were difficult to notice or unnoticeable with the NCCC method are now clearly visible. Two strong correlated peaks appear relatively close to each other at time delay values between 0.15 and 0.20 ms. The two correlated peaks correspond to the time difference between the two pressure spikes from transducer

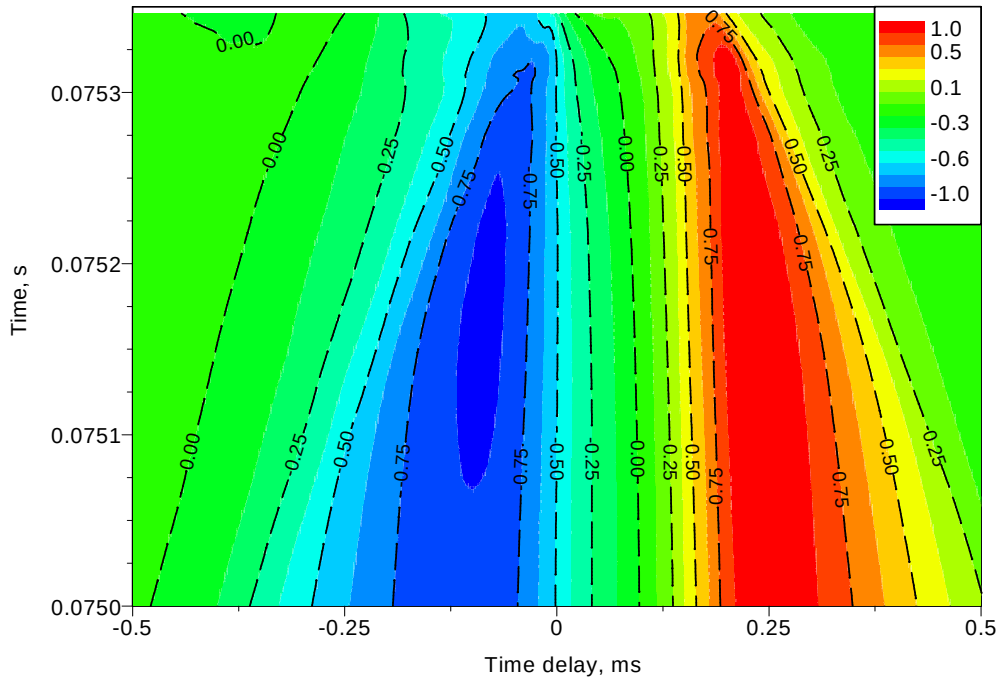

Figure 5.4. The NCCC result with a constant upper time limit for the incident shock wave in Fig. 5.2.

2 to the shock front from transducer 3. Also, a smaller correlation is located at around zero time delay (yellow shade) that was not revealed in the NCCC method. The magnitude difference between the peaks and the surrounding values decreases as the lower time index (ordinate) approaches the shock front. Unlike the NCCC method, the time delay estimate for the NECC does vary significantly with time for transducers 2–3, see Table 5.1. The large variance is due to the multiple pressure spikes exhibited by transducer 2. For small lower time index values, the NECC favors the initial shock front for a time delay value of approximately 0.192 ms. For larger lower time index values that approach the disturbance, the NECC favors the second pressure rise. Thus, the time delay estimate for the larger index values are closer to the NCCC and TOF method estimates at approximately 0.154 ms.

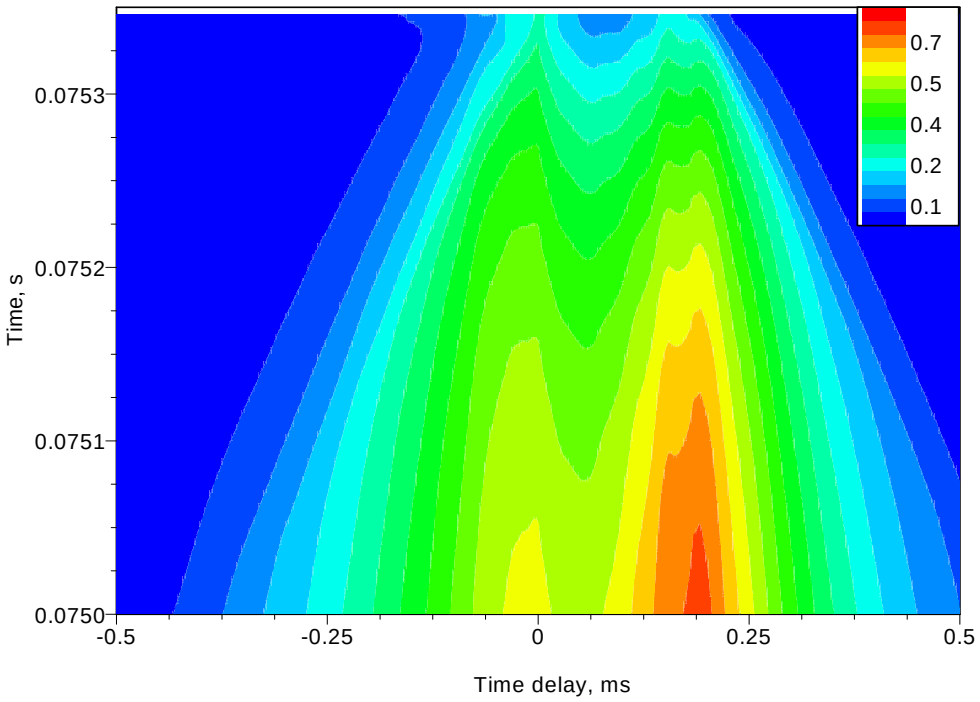

Figure 5.5. The NECC result with a constant upper limit for the incident shock wave in Fig. 5.2.

Next, the coherence function for transducers 2–3 is shown in Fig. 5.6. The figure shows that the coherence between the signals is very poor. The poor coherence is because the coherence crosses the imposed minimum threshold of 50% multiple times and fluctuates significantly with frequency. Referring to Table 5.1, the phase results for transducers 2–3 are very poor compared to the other methods. The combination of the poor coherence between the signals and the multiple correlated peaks for the NCCC method contribute to the poor estimate. Unlike the NCCC and NECC methods that depend only on the peak correlation value, the NCSDP and NCSDPE account for all the peaks exhibited by the correlation function. So the time delay estimate is dependent on the entire correlation function, which for transducers 2–3 exhibit large correlated peak values within the broad region ranging over a large time delay from 0.0 to 0.2 ms. The multiple correlated peaks contribute to the large

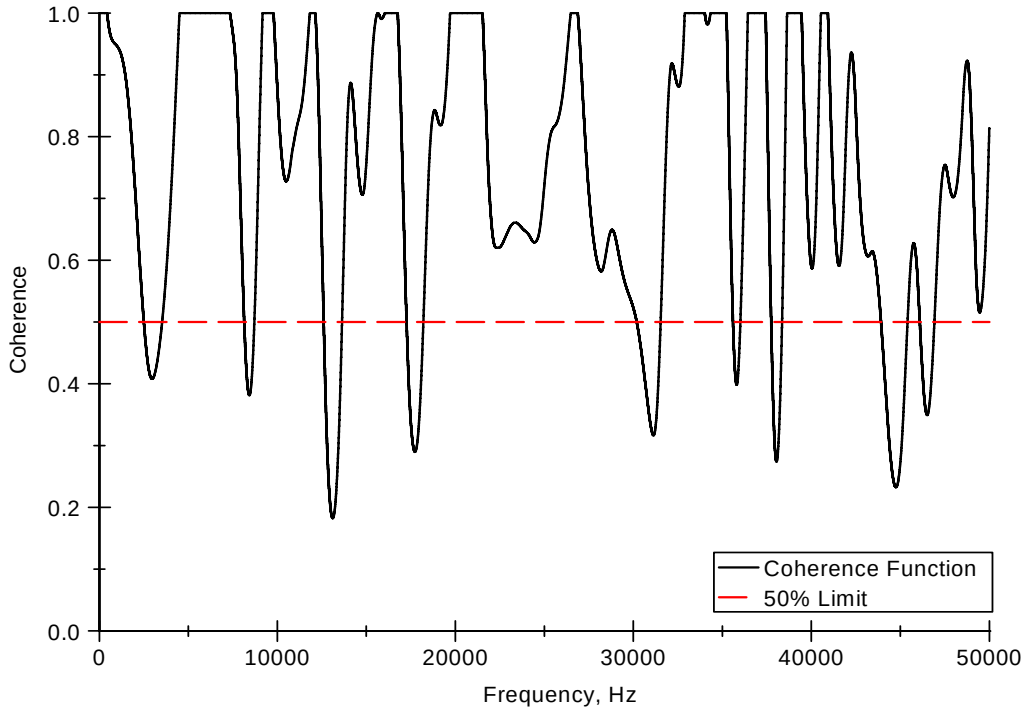

Figure 5.6. The coherence function for the incident shock wave displayed in Fig. 5.2.

variances for both methods. For the NCSDPE method, the error is reduced due to the more distinct correlation function which has a faster roll-off rate provided by the NECC method. Both the NCSDP and NCSDPE methods vary significantly with the lower time index (ordinate) as can be seen by the standard deviation column in Table 5.1 for transducers 2–3. The variance is large as the lower time index approaches the shock front. Turning to the CSDP-2 and CSDP-2E methods, these also have difficulties in providing a good estimate for the time delay. The poor estimates provided by the CSDP-2 and CSDP-2E methods is due to a combination of the poor coherence between the signals and the strong oscillations with multiple pressure spikes recorded by transducer 2. The two methods also appear to be more sensitive to time since the standard deviation is large for both methods as shown by the standard deviation column in Table 5.1.

The results for the WCCC-Haar method are displayed in Fig. 5.7. The contour plot is represented by a scale and a time delay axis. The abscissa is once again represented by the imposed time delay between the signals. The ordinate is now represented by the scales for the WCCC and WECC functions. The scales can be related to frequency as shown in Appendix C. A table relating the pseudo-frequencies to scales for the shock tube experiment is provided in Table 5.2. Figure 5.7 shows several bands of strong correlations at various time delays. The strong correlations seen to the far right are due to a combination of the large unsteadiness from transducer 2 and the effect of utilizing the so-called unbiased estimate. The unbiased estimate amplifies the small correlation value near the edges of the time window, which introduces an error in the estimate. However, two correlated bands (in green and yellow) are seen at a time delay approximately from 0.15–0.20 ms. These correlated bands correspond to the expected time delay from the signals. Unfortunately, using the envelope signals does not improve the results for the WECC-Haar method as shown in Fig. 5.8. The WECC method only further enhances the correlated peak for the time delay estimate to the right. The two correlated bands corresponding to the expected time delay are largely overshadowed by the artifacts with the use of the envelope signals.

A 50% cutoff was imposed on the WCCC and WECC results to exclude the artifacts occuring due to the limited information. The time delay estimates were then filtered to exclude the scales with erroneous results. The time delay results are provided in Table 5.1. Unlike the NCCC method, both the WCCC-Haar and WECC-Haar results indicated that they are influenced by the initial shock fronts. Referring to the standard deviation column for Table 5.1, the time delay variation amongst the selective scales for both the Haar methods is small with a standard deviation of 0.001 ms.

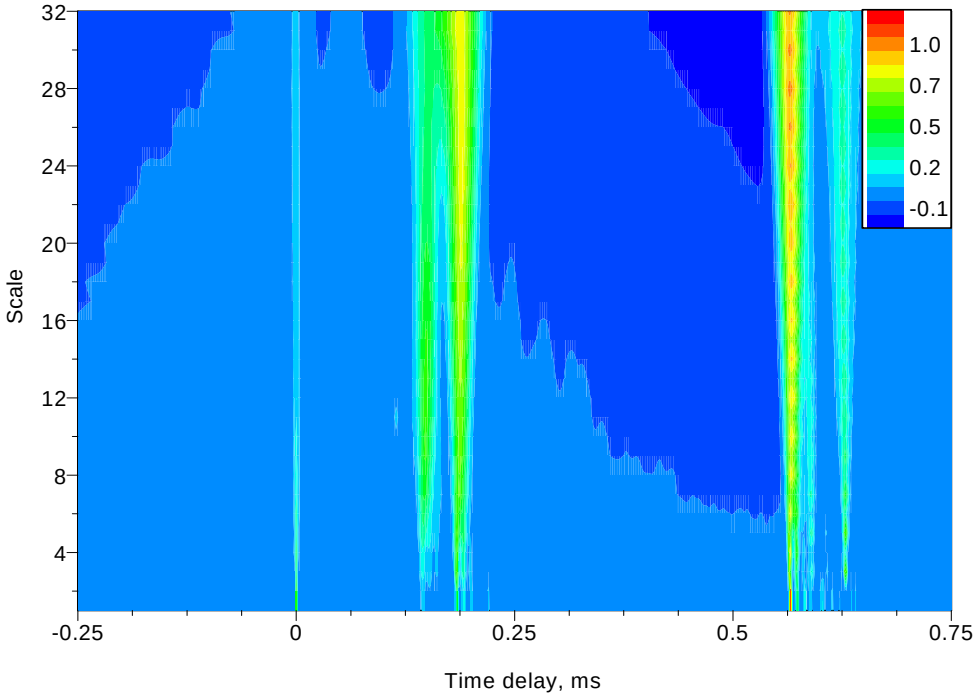

Figure 5.7. The WCCC-Haar result for the incident shock wave in Fig. 5.2.

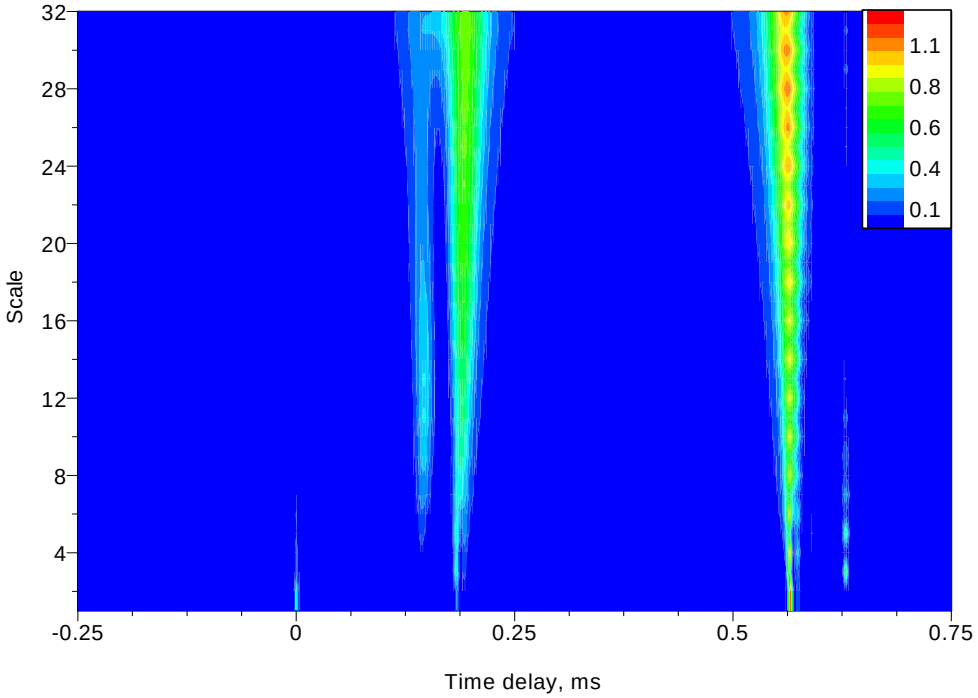

Figure 5.8. The WECC-Haar result for the incident shock wave in Fig. 5.2.

Table 5.2. A scale to pseudo-frequency relationship for the Haar and Morlet wavelet functions for the shock tube experiment

Scale	F_{aHaar}, Hz	$F_{aMorlet}$, Hz
4	124514	101563
8	162257	150781
12	41505	33854
16	31128	25391
20	24903	20313
24	20752	16927
28	17788	14509
32	15564	12695

The results for the Morlet method are shown in Figs. 5.9 and 5.10. The Morlet version also contains artifacts at large time delay values that influence the time delay estimate. Referring to Fig. 5.9, the influence is clearly seen in the dark red bands appearing at the larger scales (low frequencies) and the smaller scales (high frequencies). However, for intermediate scales (values of 10–22), the time delay estimate is in the vicinity of the expected time delay. Since the Morlet wavelet is not as well time localized as the Haar wavelet, the correlated peaks spread as a function of the center frequency defined by the Morlet function. So multiple bands are seen surrounding the maximum correlated values. Once again, the use of the envelope signals only enhances the artifact seen near the edge of the time window for the WECC-Morlet. The 50% cutoff was also utilized for the Morlet methods to improve the time delay results. Only the intermediate section provided feasible results, so only these correlated values were used for determining the statistical time delay estimate for the propagating shock wave that are displayed in Table 5.1. The results show that the Morlet methods were influenced by both pressure spikes recorded by transducer 2. For low scales, the second pressure spike is the primary influence on the correlation function with a time delay estimate of approximately 0.147 ms. For larger scales,

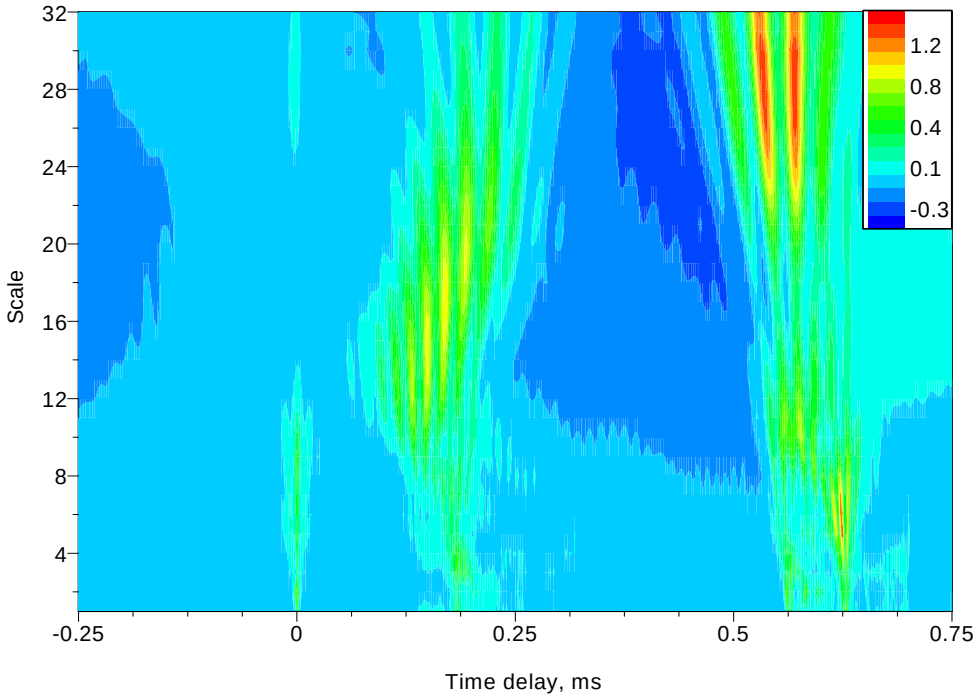

Figure 5.9. The WCCC-Morlet result for the incident shock wave in Fig. 5.2.

the initial shock front is the main influence for the wavelet methods. The time delay estimate for the larger scales is around 0.186 ms. Since the Morlet methods are influenced by both the pressure spikes recorded by transducer 2, the time delay estimate has a large standard deviation of 0.021 ms.

5.1.2 Reflected Shock

The time delay estimates for the first reflected shock are shown in Table 5.3. The time delay estimates are significantly larger for the reflected shock wave, which shows that the shock wave has slowed down as expected from gasdynamics theory. When a shock wave is reflected off a rigid surface, the shock strength as characterized by its pressure ratio is increased and so is the shock Mach number. A further attenuation occurs due to boundary layer development.

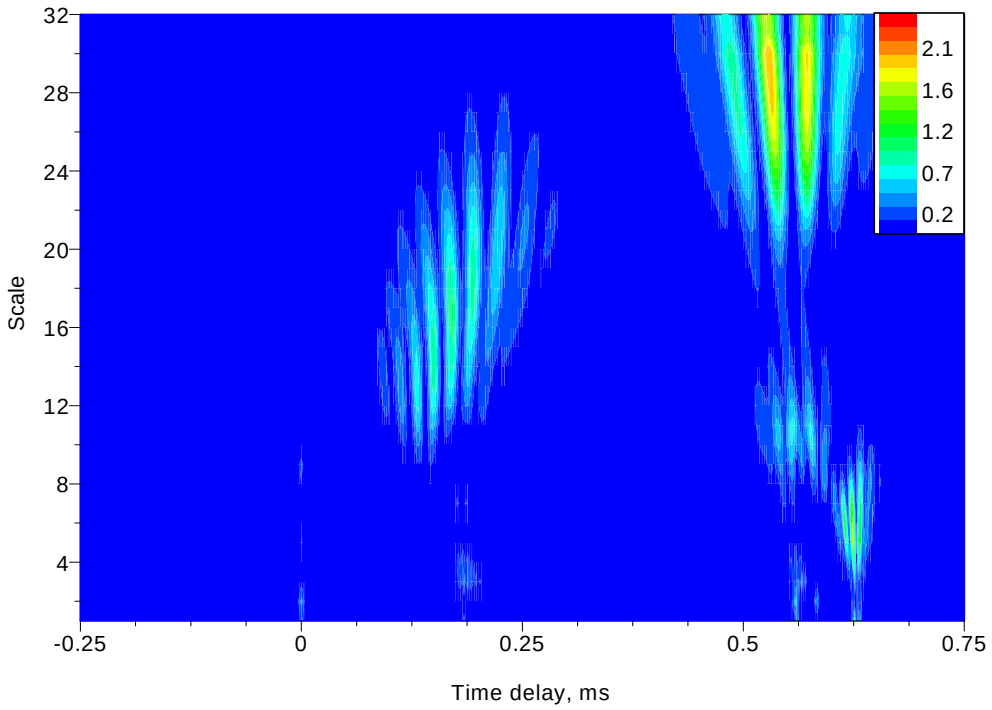

Figure 5.10. The WECC-Morlet result for the incident shock wave in Fig. 5.2.

The pressure histories of the reflected shock for transducers 2–3 are displayed in Fig. 5.11. Unlike the previous pressure histories for the incident shock wave, the pressure continues to rise after the shock. For estimating the propagation time, the time window was limited so as not to include the entire event of the reflected shock wave. The NCCC result for the transducers are shown in Fig. 5.12. The figure shows a correlation function that contains a very broad peak. The range of the peak is very large as it covers many time delay values. The correlation function also varies significantly with the lower time index (ordinate). The variation of the correlation function is clearly seen as the correlated peak shifts from around 0.5 ms at small lower time index values to values near zero time delay at larger time index values that are near the shock front.

Table 5.3. Time delay values for the reflected shock wave using various methods

	Transducers 1–2		Transducers 2–3		Transducers 3–4	
Method	$\bar{\tau}$, ms	$\sigma(\tau)$, ms	$\bar{\tau}$, ms	$\sigma(\tau)$, ms	$\bar{\tau}$, ms	$\sigma(\tau)$, ms
TOF pk-pk	−0.520	–	−0.532	–	−0.348	–
NCCC	−0.450	0.123	−0.260	0.243	−0.287	0.131
NHCCC	−0.170	0.037	−0.108	0.050	−0.104	0.036
NECC	−0.641	0.086	−0.630	0.067	−0.435	0.044
NCSDP	−0.057	0.064	−0.050	0.045	−0.016	0.014
NCSDPE	−0.001	0.002	−0.001	0.002	−0.009	0.004
CSDP-2	−0.226	0.083	−0.213	0.136	−0.201	0.092
CSDP-2E	−0.217	0.077	−0.209	0.110	−0.178	0.078
WCCC-Haar	−0.540	0.004	−0.510	0.004	−0.360	0.001
WCCC-Morlet	−0.941	0.010	−0.927	0.008	−0.358	0.000
WECC-Haar	−0.540	0.004	−0.510	0.004	−0.360	0.001
WECC-Morlet	−0.980	0.043	−0.927	0.008	−0.358	0.000

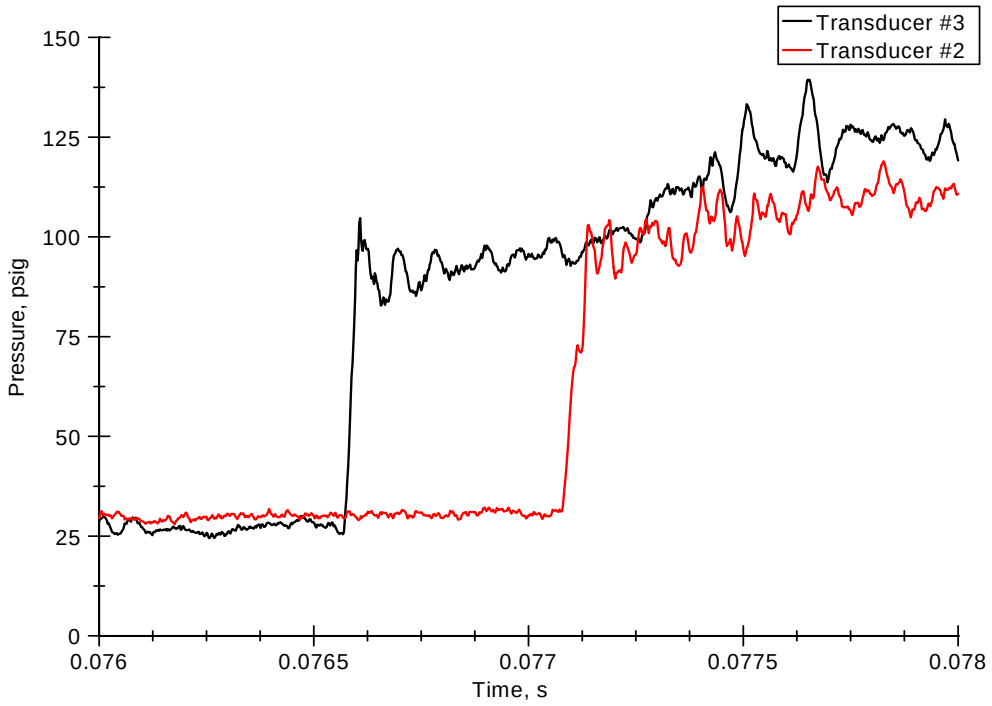

Figure 5.11. Pressure history window for reflected shock wave for transducers # 2 and 3.

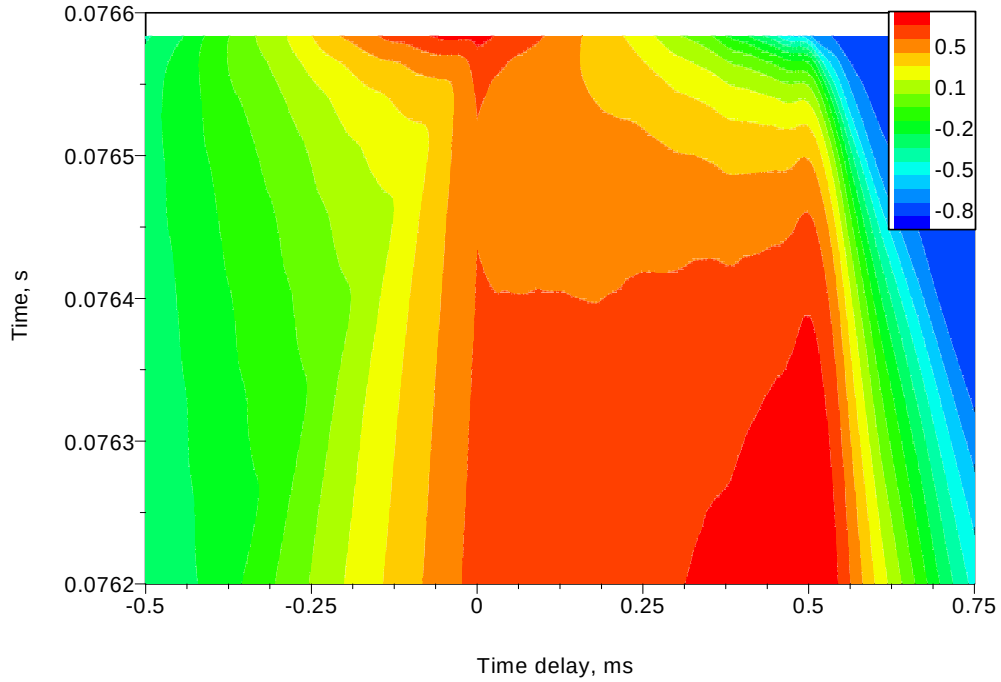

Figure 5.12. The NCCC result with a constant upper time limit for the reflected shock wave in Fig. 5.11.

The NHCCC for transducers 2–3 is shown in Fig. 5.13. Just as for the incident shock wave, the NHCCC is unable to correctly identify the time delay between the transducers. The estimate is significantly affected by the the combination of the pressure increase, the strong pressure fluctuations and when the lower time index approaches the shock front.

The results for the NECC for transducers 2–3 are provided in Fig. 5.14. Similar to the NCCC method, the correlation function has a broad peak over a large range of possible time delay values. However, the correlated peak for the NECC varies significantly less than the NCCC method as shown in the standard deviation column in Table 5.3.

The coherence function for the signals from the reflected shock past transducers 2–3 is shown in Fig. 5.15. The coherence for the signals is very poor, far poorer than

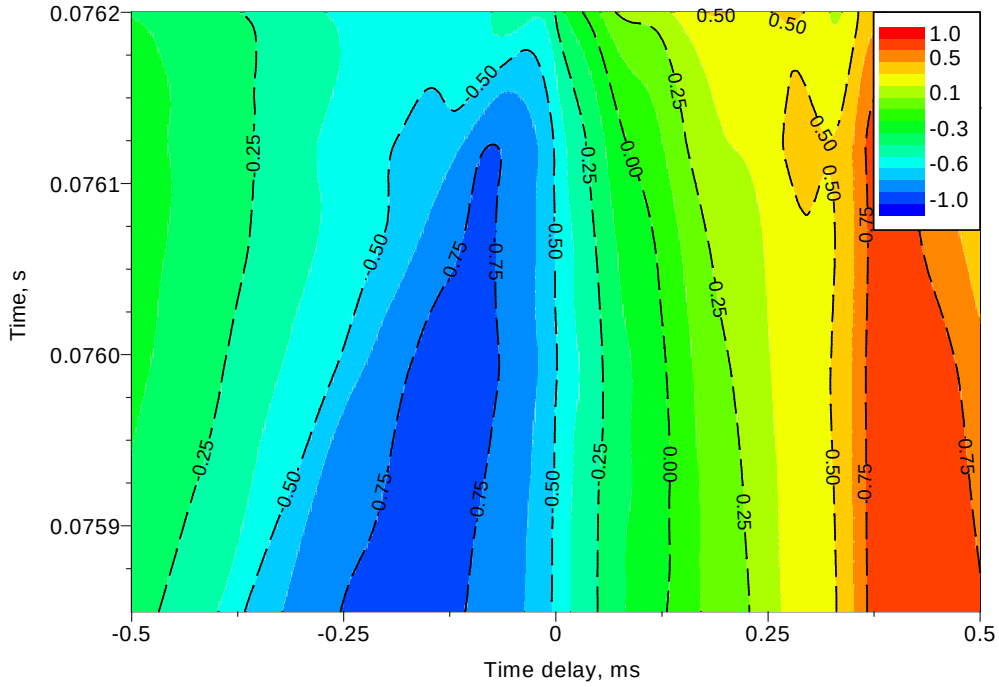

Figure 5.13. The NHCCC result with a constant upper limit for the reflected shock wave in Fig. 5.11.

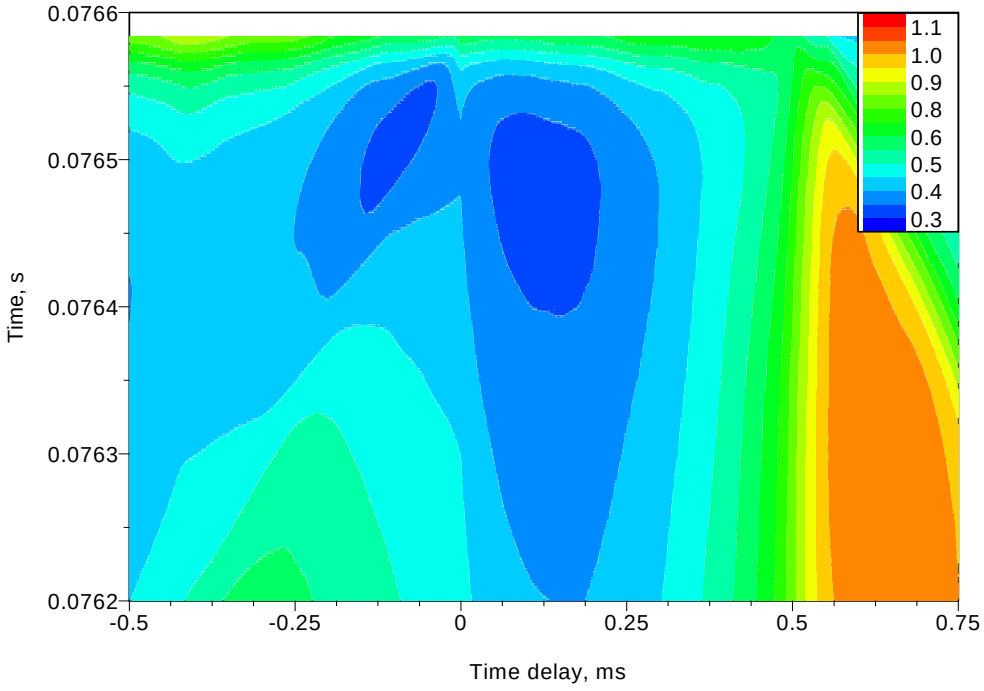

Figure 5.14. The NECC result with a constant upper limit for the reflected shock wave in Fig. 5.11.

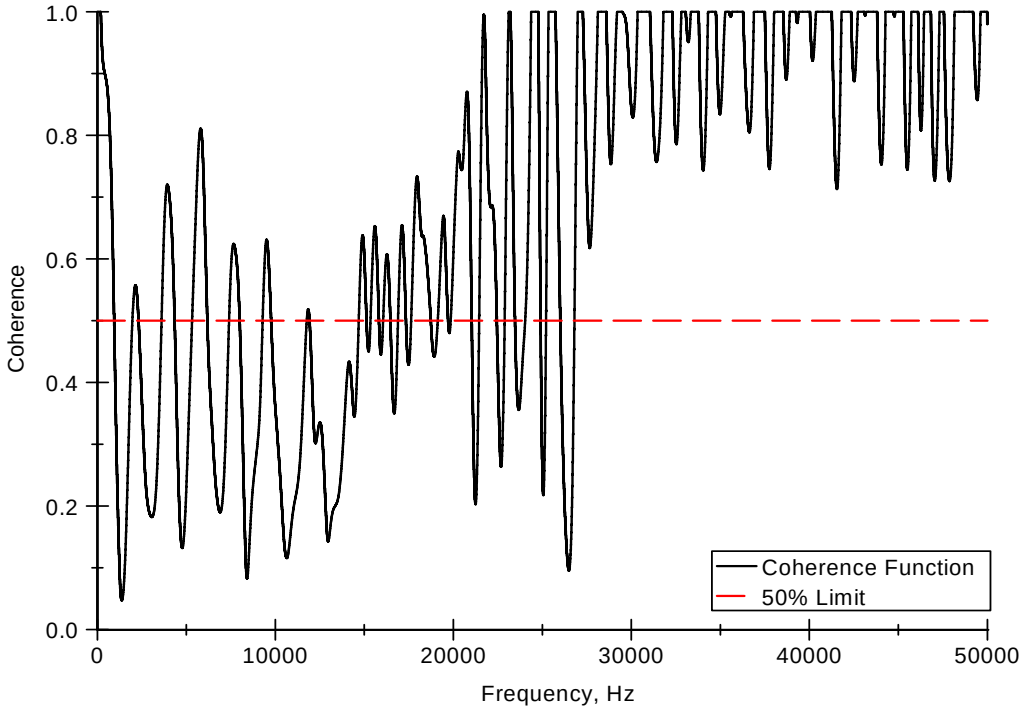

Figure 5.15. The coherence function for the reflected shock wave displayed in Fig. 5.11.

for the incident shock passage. The poor coherence is evident at lower frequencies were the coherence has multiple crossings to below the 50% limit and whose peaks do not exceed a coherence value of 0.8. The combination of the poor coherence and the poor correlation functions from the NCCC and NECC make for poor results for the NCSDP, NCSDP-E, CSDP-2 and CSDP-2E. All of these methods were unable to correctly identify the expected time delay for the reflected shock wave as shown in the results for transducers 2–3 in Table 5.3.

The results for the WCCC-Haar method are provided in Fig. 5.16. Similar to the incident wave, an artifact is seen near the edge of the window. The expected time delay is seen by a green band at around 0.5 ms. Unfortunately, the amplitude of the correct time delay value is significantly less than the artifact's amplitude. The use of envelope signals further amplifies the artifact, which overshadows the other

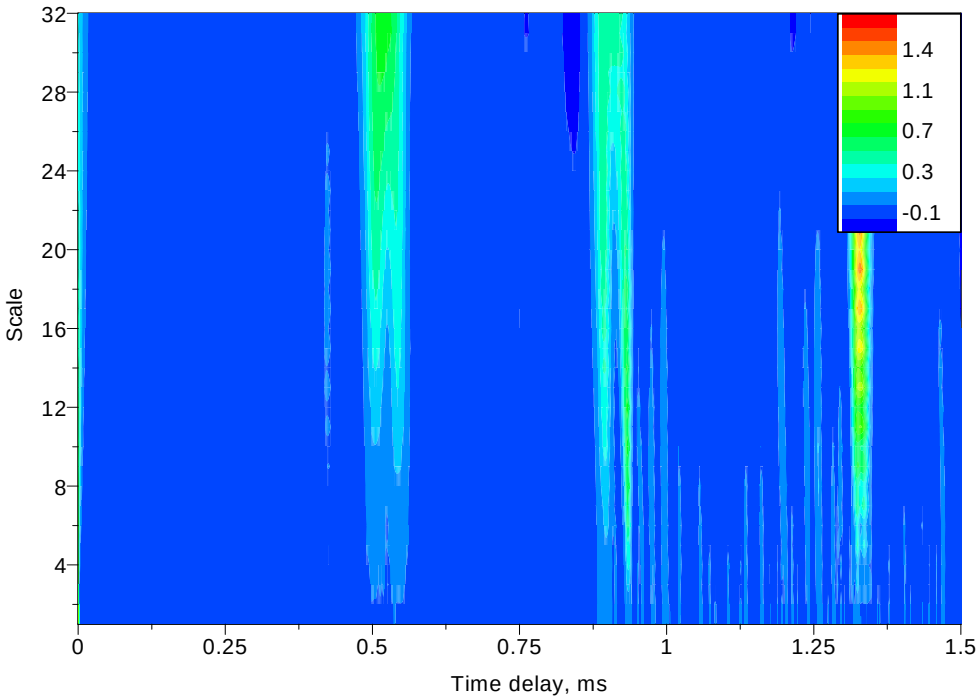

Figure 5.16. The WCCC-Haar result for the reflected shock wave in Fig. 5.11.

correlated peaks as seen in Fig. 5.17 for the WECC-Haar method. The 50% cutoff is once again used to provide improved time delay estimates for the wavelet methods. With the use of the cutoff and filtering of erroneous data, both Haar methods were able to successfully identify the shock front. Only large scale (19-32) values were used for determining the time delay estimate as they provided the only feasible results.

Similar results are shown for the Morlet versions in Fig. 5.18 and 5.19. The artifact near the edge of the window is once again present and resulted in an incorrect estimate of the time delay for the signals. A strong correlation is also exhibited at no time delay by a green band for all scales. The use of the envelope signal only enhances the artifact near the edge of the window, and the expected time delay is once again overshadowed. The application of the 50% cutoff and filtering was unable to improve the results for the Morlet methods. The Morlet methods were strongly influenced at

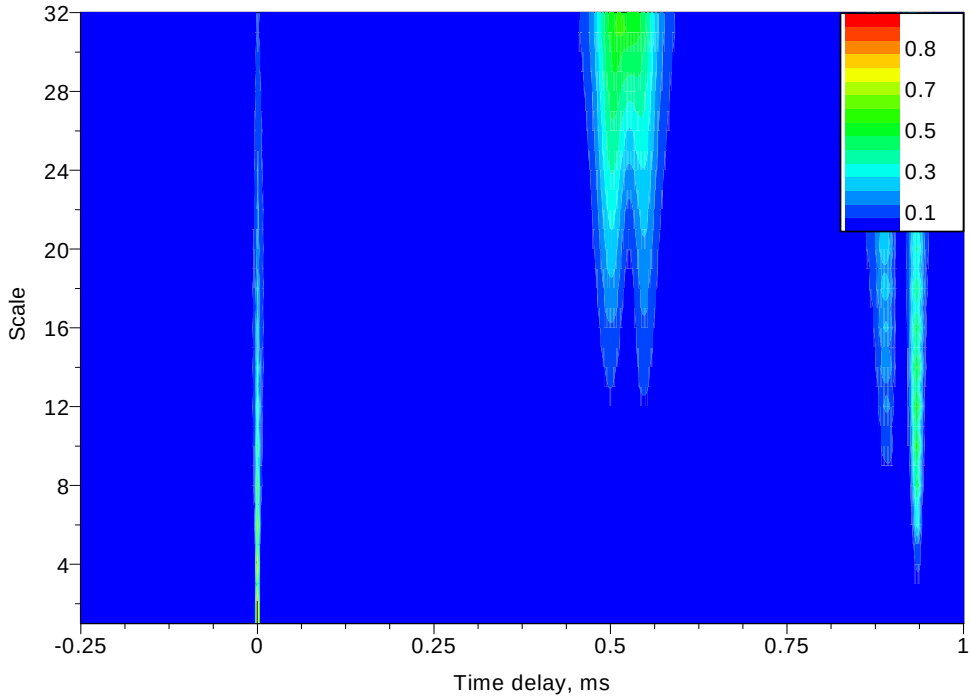

Figure 5.17. The WECC-Haar result for the reflected shock wave in Fig. 5.11.

zero time delay; zero time delay corresponds to the one point that utilizes the entire data for a given time window as it has the most arithmetic operations.

5.1.3 Second Reflected Shock Wave

Most of the methods were unable to identify the propagation time successfully. A larger time window that included the entire event may have allowed for some other methods to determine a valid estimate of the time delay. Only the WCCC-Haar and WECC-Haar methods were able to provide plausable time delay estimates. The result for the NCCC method provides a large variation that allows for a slim possibilty of successfully identifying the propagation time. The NECC improves the time delay estimate provided by the NCCC, but also has a large uncertainty in the time delay estimate. All of the phase methods provide bad results.

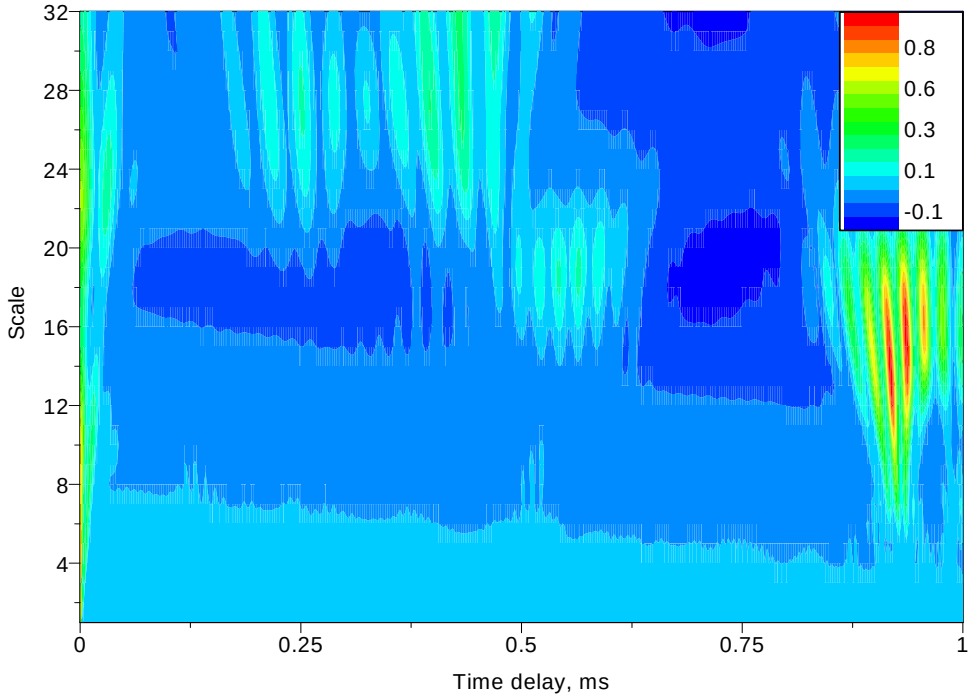

Figure 5.18. The WCCC-Morlet result for the reflected shock wave in Fig. 5.11.

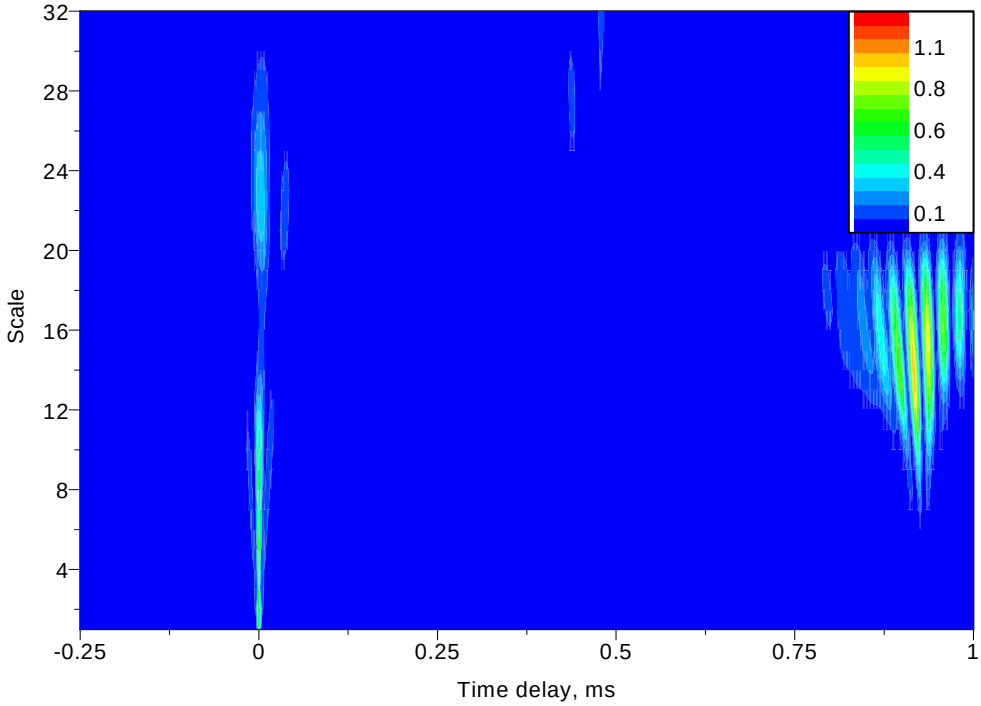

Figure 5.19. The WECC-Morlet result for the reflected shock wave in Fig. 5.11.

Table 5.4. Time delay values for the reflected shock wave using various methods

	Transducers 1–2		Transducers 2–3		Transducers 3–4	
Method	$\bar{\tau}$, ms	$\sigma(\tau)$, ms	$\bar{\tau}$, ms	$\sigma(\tau)$, ms	$\bar{\tau}$, ms	$\sigma(\tau)$, ms
TOF pk-pk	0.300	–	0.238	–	0.210	–
NCCC	0.271	0.047	0.235	0.021	0.223	0.006
NHCCC	0.200	0.013	0.208	0.004	0.167	0.030
NECC	0.299	0.009	0.244	0.007	0.232	0.003
NCSDP	0.076	0.202	0.070	0.139	0.058	0.144
NCSDPE	0.176	0.049	0.118	0.038	0.127	0.039
CSDP-2	0.190	0.088	0.151	0.074	0.178	0.073
CSDP-2E	0.200	0.093	0.148	0.069	0.178	0.064
WCCC-Haar	0.270	0.001	0.266	0.001	0.224	0.001
WCCC-Morlet	0.280	0.041	0.230	0.026	0.227	0.007
WECC-Haar	0.270	0.001	0.266	0.001	0.224	0.001
WECC-Morlet	0.280	0.041	0.230	0.026	0.227	0.007

The reflected wave time delay estimates are summarized in Table 5.4. Referring to Table 5.4, the shock wave appears to have increased in velocity after the second reflection, yet is still slower than the incident propagating shock. The reason for the increase in velocity is due to the first reflection moving upstream on an incoming flow that reduced the relative speed of the shock. The pressure histories for transducers 3–4 are shown in Fig. 5.20. Large fluctuations were present in the signals recorded by both transducers. A possible reason is that the valves in the shock tube were closed after the first reflected wave, and the abrupt closure introduced further, interfering waves.

The NCCC result for transducers 3–4 are shown in Fig. 5.21. The expected time delay is seen in red and is more distinct than the results for the NCCC for the incident and first reflected waves. A broad region still exists that covers a large portion of the possible time delay values. The broad region exists due to the signals having fluctuations of different amplitudes and frequencies. These frequencies create

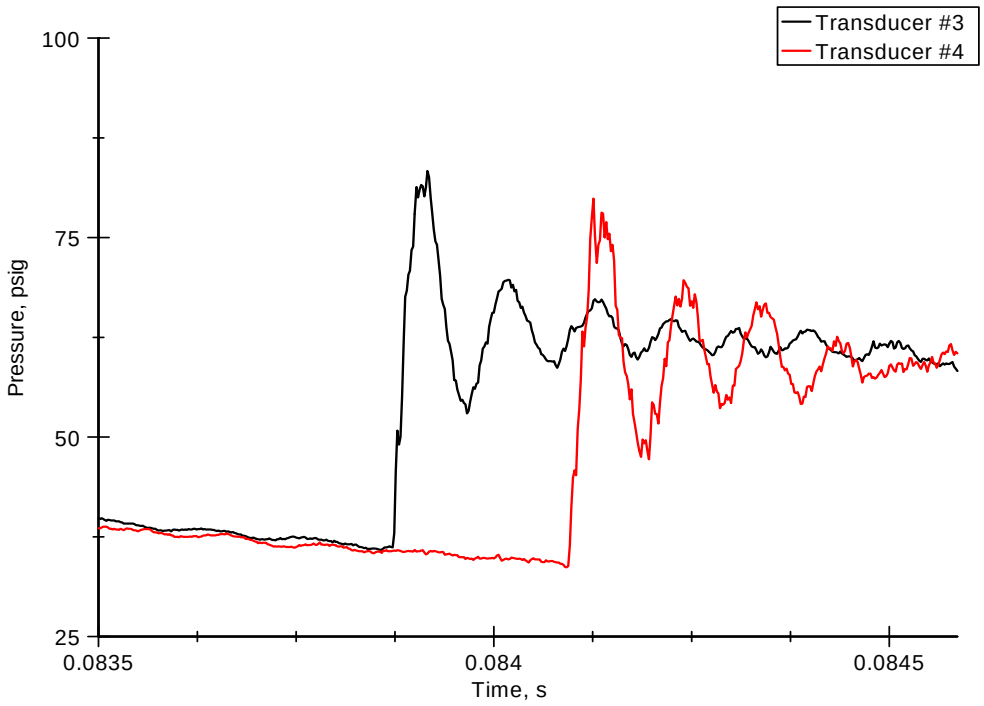

Figure 5.20. Pressure history window for second reflected shock wave for transducers # 2 and 3.

multiple correlated peaks at delay values other than the expected time delay. One of the strong correlated peaks from the fluctuations is seen by the yellow band to the left of the expected time delay. The fluctuations do not appear to affect the final result for the NCCC method as the time delay estimate is close to what was determined by eye (that is, the TOF method).

The results for transducers 3–4 with the NHCCC method are shown in Fig. 5.22. The NHCCC method appears to be affected by the strong fluctuations exhibited by the transducers. The zero-crossing range between the two extrema is large. Since the zero-crossing has a large range of time delay values, the NHCCC method yields a large uncertainty in the time delay estimate.

The results from the NECC method for transducers 3–4 are shown in Fig. 5.23. Once again, the NECCC method provides a sharper peak value for the correlation

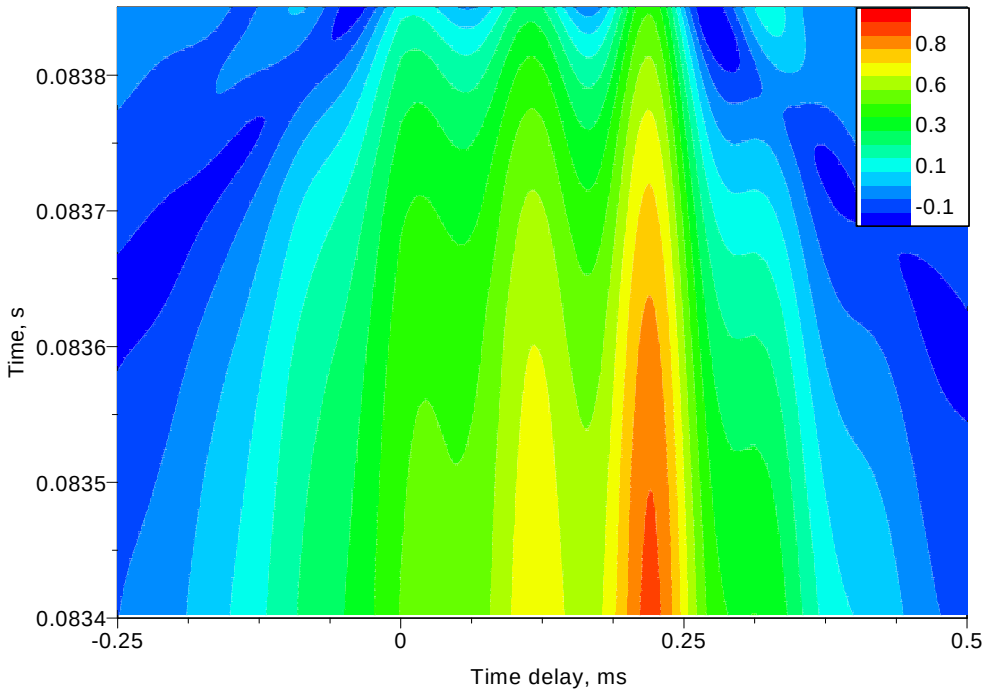

Figure 5.21. The NCCC result with a constant upper time limit for the second reflected shock wave in Fig. 5.20.

function that reduces the uncertainty in the time delay estimate. Since the NECC provides a better defined correlated peak, the correlated peaks due to the oscillations become visible. The correlated values due to the oscillations are shown (green) to the left and right of the expected time delay that were difficult to see with the NCCC method. The time delay estimate from the NECC is larger than the NCCC method.

The coherence for the signals is shown in Fig. 5.24. The coherence for the signals has only a tiny portion that crosses the 50% limit. However, the signals still have multiple regions that dip to values that signify very poor coherence. The results for the phase methods are still very poor compared to the other methods as shown in Table 5.4. The phase methods have a large variance with incorrect time delay estimates, and appear to be significantly affected by the strong fluctuations.

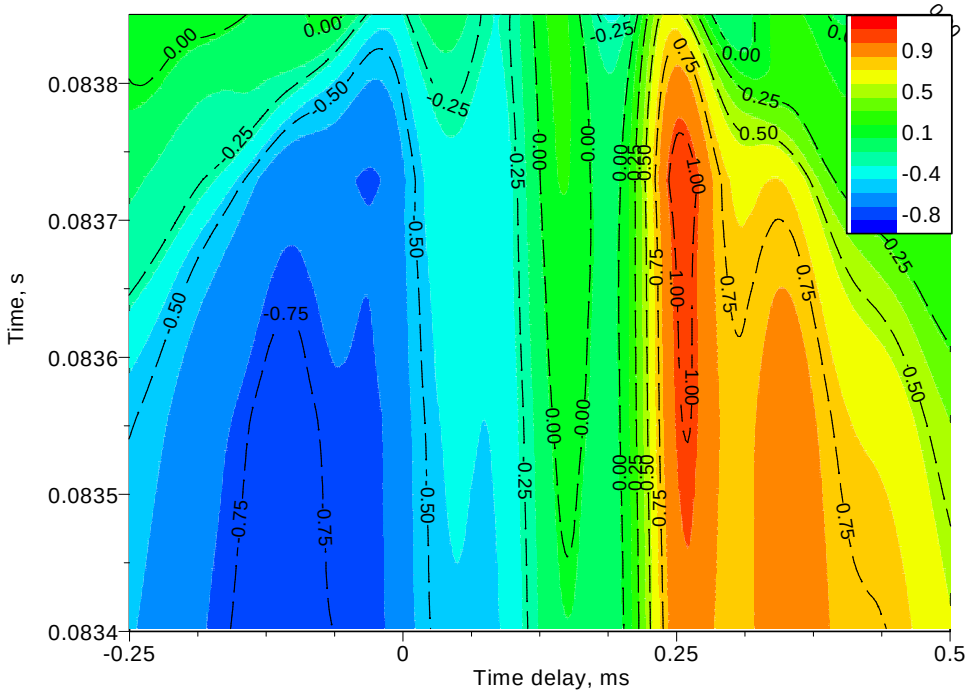

Figure 5.22. The NHCCC result with a constant upper limit for the second reflected shock wave in Fig. 5.20.

The WCCC-Haar results is shown in Fig. 5.25. Once again an artifact is seen at large time delays, but the artifact's magnitude for most scales is smaller than the expected time delay value shown in red. Strong fluctuations are also seen in the graph as green bands to the left and right of the expected time delay value. There appears to be two strong correlations in close proximity with each other as two strong peaks are seen at low scales (high frequencies). The use of the envelope correlation function makes the correlated peak more distinct for the WECC-Haar as seen in Fig. 5.26. The Haar wavelet correlation functions appear to be unaffected by the strong oscillations as both methods provide similar time delay estimates to the NCCC method as shown in Table 5.4. Application of the 50% cutoff with filtering had no effect on the time delay results for both Haar methods.

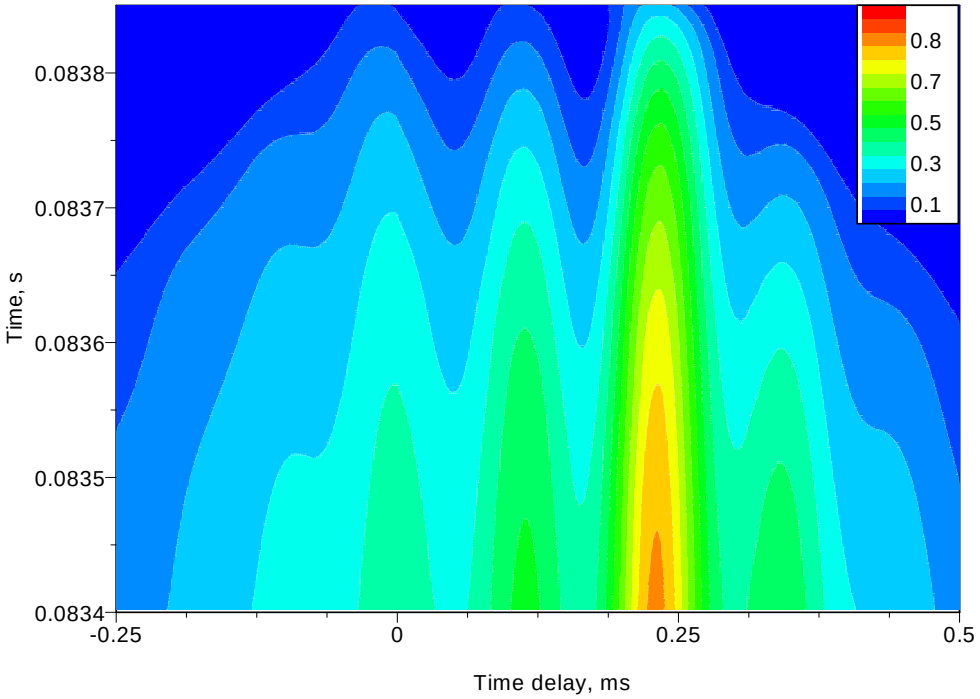

Figure 5.23. The NECC result with a constant upper limit for the second reflected shock wave in Fig. 5.20.

Results of the Morlet wavelet methods are displayed in Figs. 5.27 and 5.28. Similar to the Haar wavelet methods, an artifact is seen at large time delays. However, the significance of the artifact is much stronger for the low to intermediate scales (1–20). For high scales (that is, low frequencies), the WCCC-Morlet and WECC-Morlet methods appear to identify the expected time delay as shown in Table 5.4. An improvement for the time delay estimate was seen after applying the 50% cutoff and filtering as the scales influenced by the artifact were removed.

5.2 Detonation Results

The methods discussed above were also used to determine the time delay for a propagating detonation wave in a pulsed detonation engine. Three consecutive detonation pulses were analyzed and are shown in Fig. 5.29. Six pressure transducers

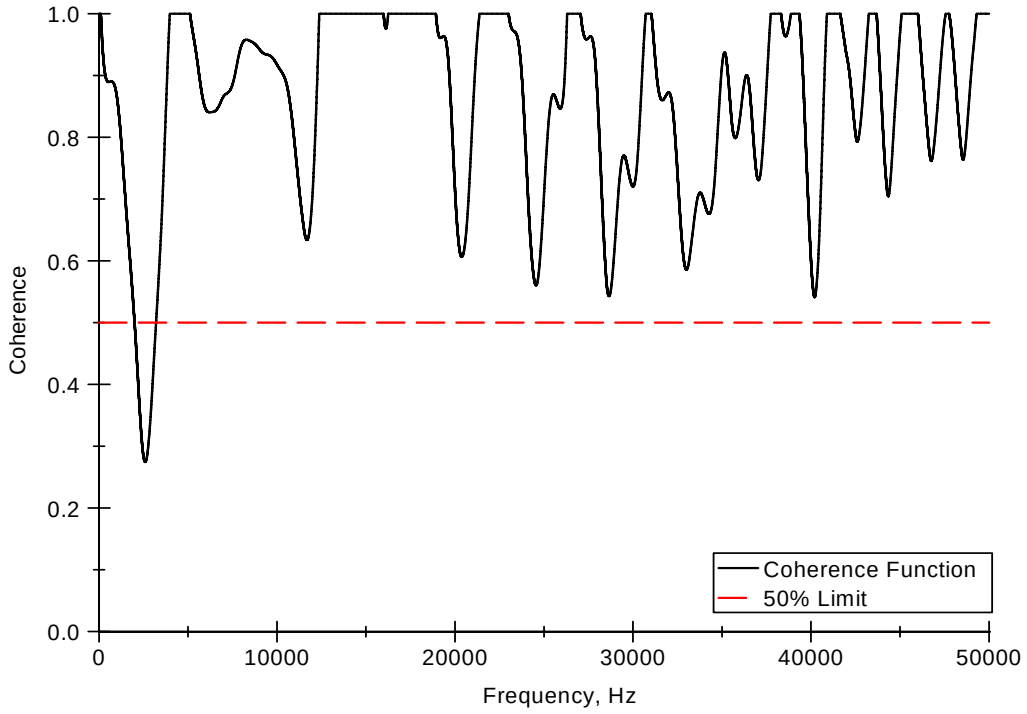

Figure 5.24. The coherence function for the second reflected shock wave displayed in Fig. 5.20.

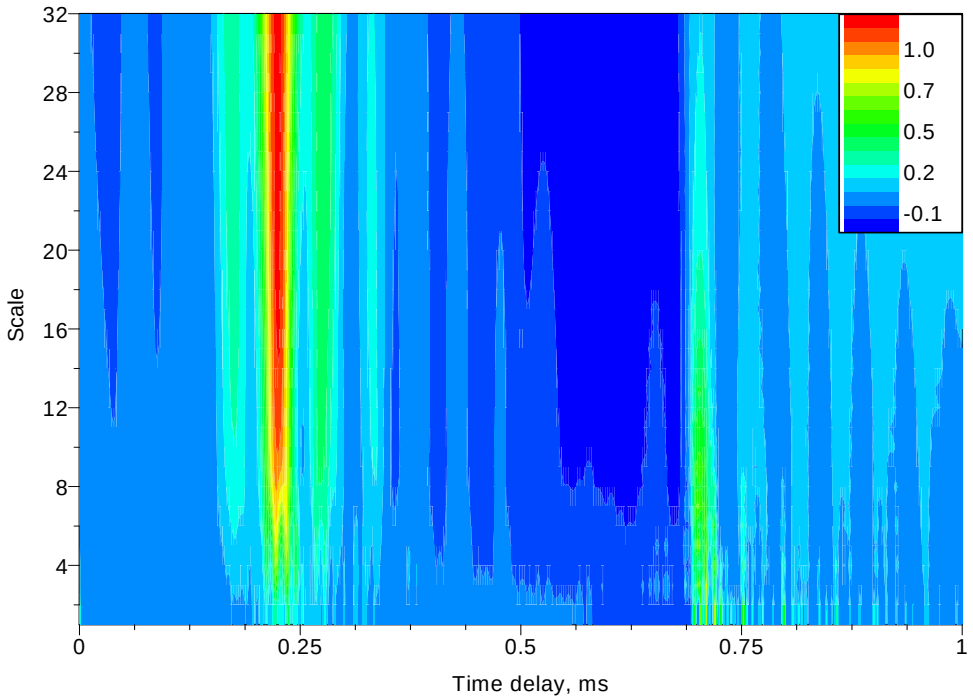

Figure 5.25. The WCCC-Haar result for the second reflected shock wave in Fig. 5.20.

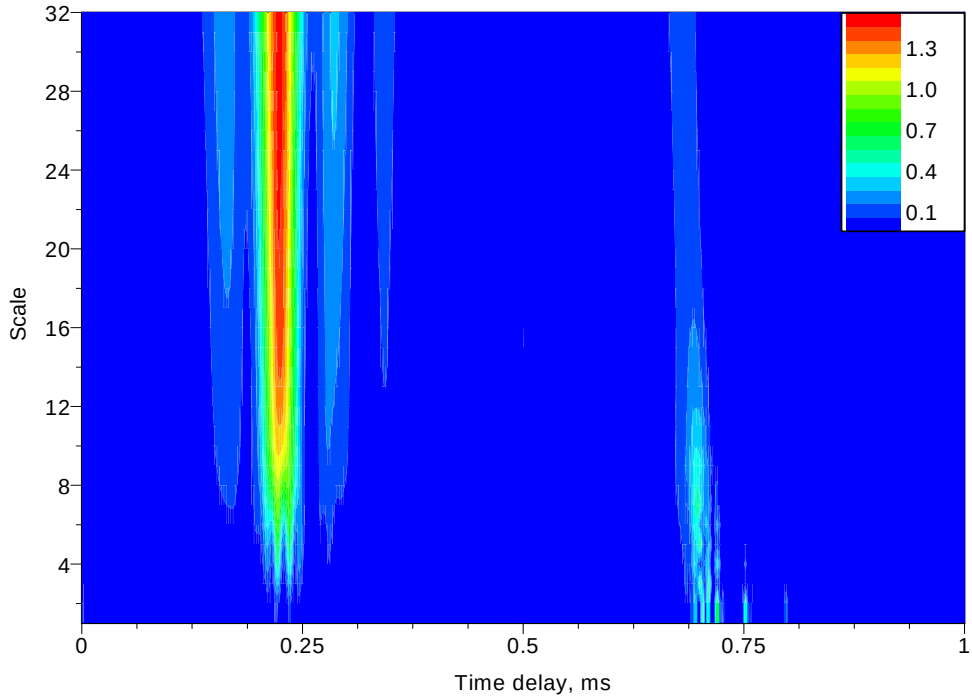

Figure 5.26. The WECC-Haar result for the second reflected shock wave in Fig. 5.20.

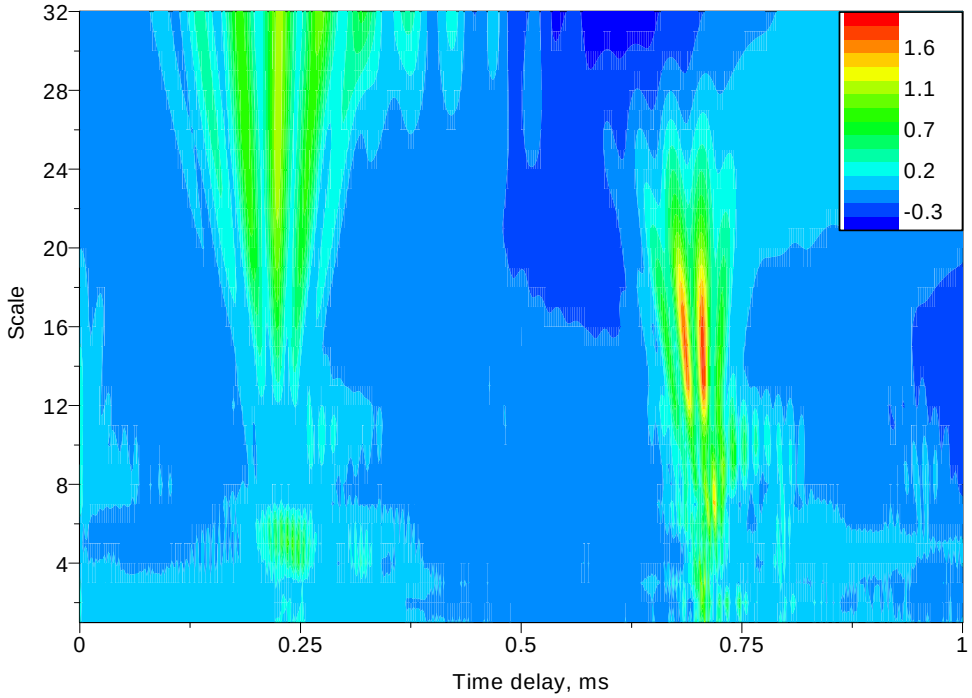

Figure 5.27. The WCCC-Morlet result for the second reflected shock wave in Fig. 5.20.

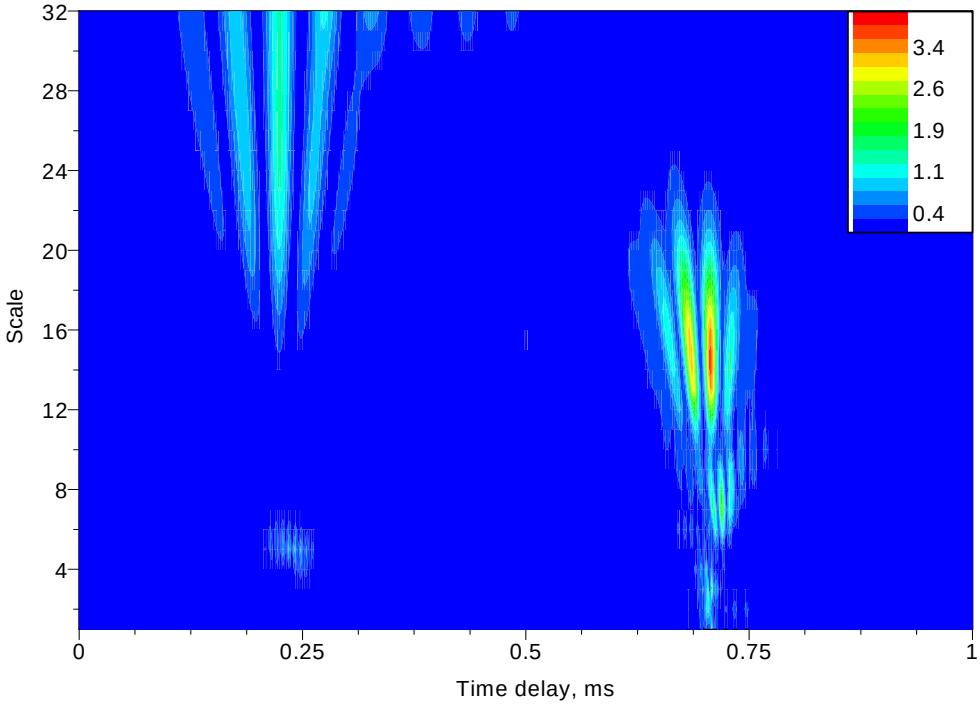

Figure 5.28. The WECC-Morlet result for the second reflected shock wave in Fig. 5.20.

were used that were equally spaced at four inches apart from each other. The data were captured at a sampling rate of 240 kHz.

The pressure history for the first detonation wave is provided in Figs. 5.30–5.34. Referring to the pressure history figures, the von Neumann spike [31] is clearly not captured properly and appears as a spike of different amplitude. The reason that the transducer is unable to capture the von Neumann spike is primarily because of the relative size of the transducer to the shock front and because the pressure rise is faster than the sensor's response time or the sampling rate of the data acquisition system. A table of the propagation time for the first detonation wave for all the methods is shown in Table 5.5. Unlike the shock tube experiments, the results for the detonation wave are generally the same. Only the NCCC, NCSDP, CSDP-2, and the Morlet wavelet results have difficulties in successfully determining the propagation

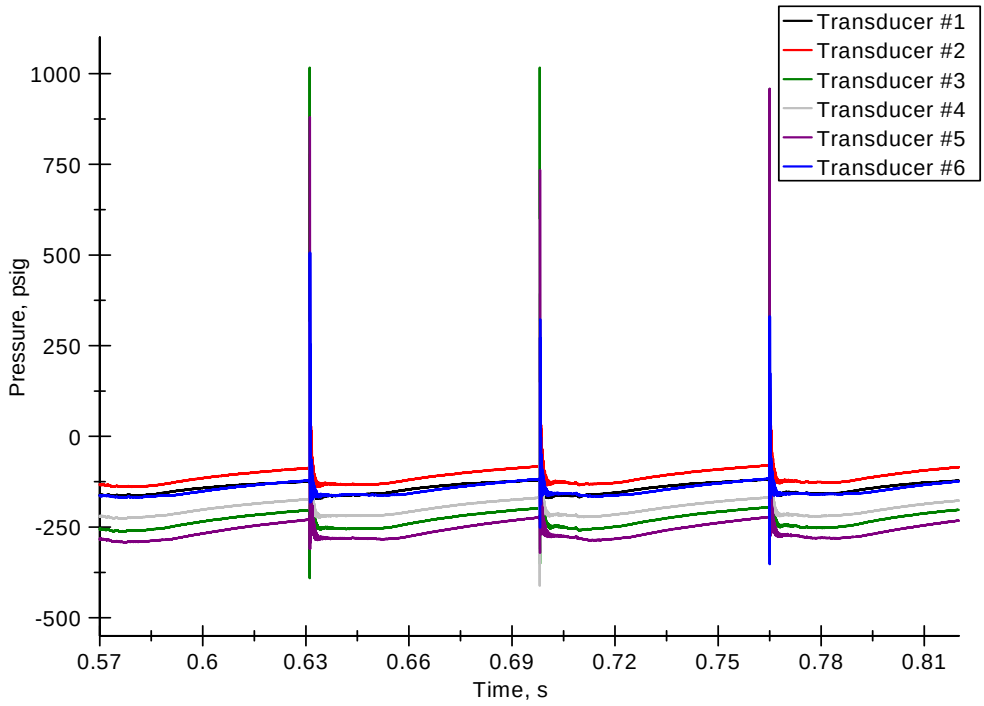

Figure 5.29. Pressure history for three detonation waves from a PDE.

time. These methods were unable to provide a good time delay estimate due to the violent oscillations during the Taylor expansion following the von Neumann spike. The oscillation peaks were slightly weaker (transducer 4) or stronger (transducer 6), which influenced the estimation of the time delay.

For transducers 3–4 and 5–6, the pressure wave with the violent oscillations is the following signal. Since the delayed part has the violent oscillations, the time delay will be equal to or greater than the expected time delay. For the NCSDP, CSDP-2, WCCC-Morlet and WECC-Morlet methods applied to transducers 3–4 and 5–6, the time delay estimate is greater than the other methods. The violent oscillations appear to have a greater influence than the von Neumann spike on the time delay estimate. For the NCSDP, CSDP-2, WCCC-Morlet and WECC-Morlet methods, the time delay estimate is less than expected for transducers 4–5 due to the presence of

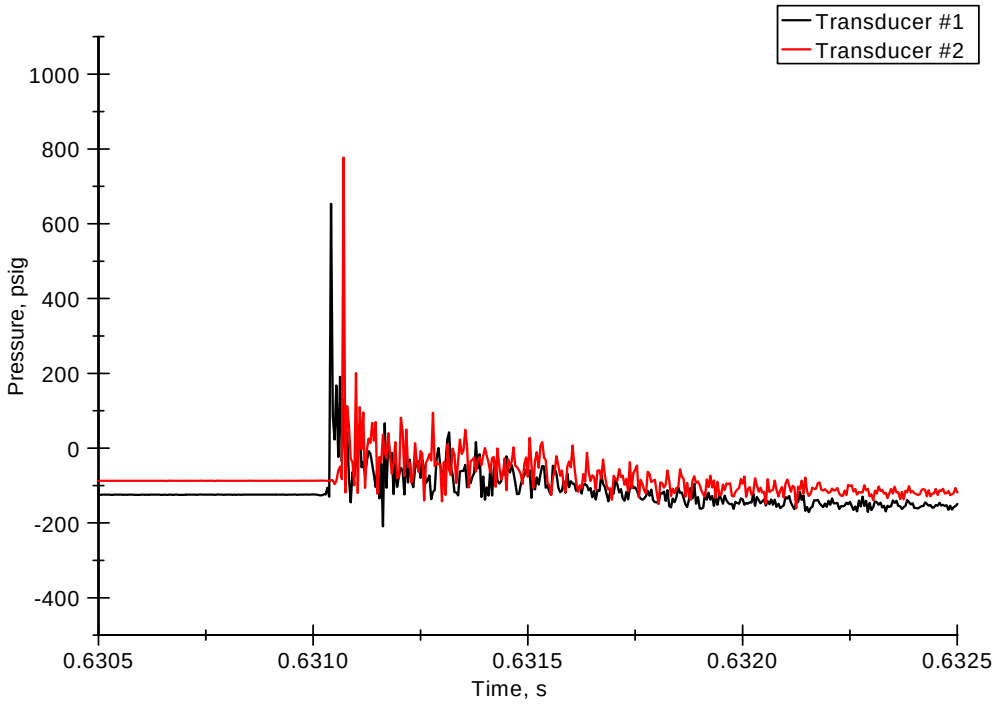

Figure 5.30. The first detonation wave pressure history for transducers #1 and 2.

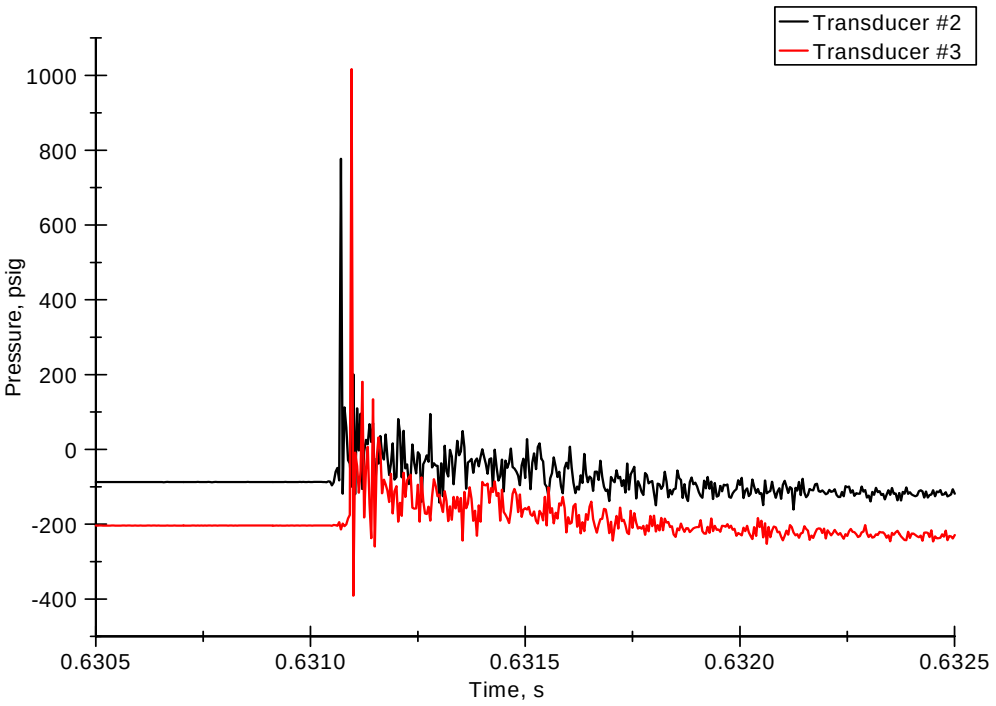

Figure 5.31. The first detonation wave pressure history for transducers #2 and 3.

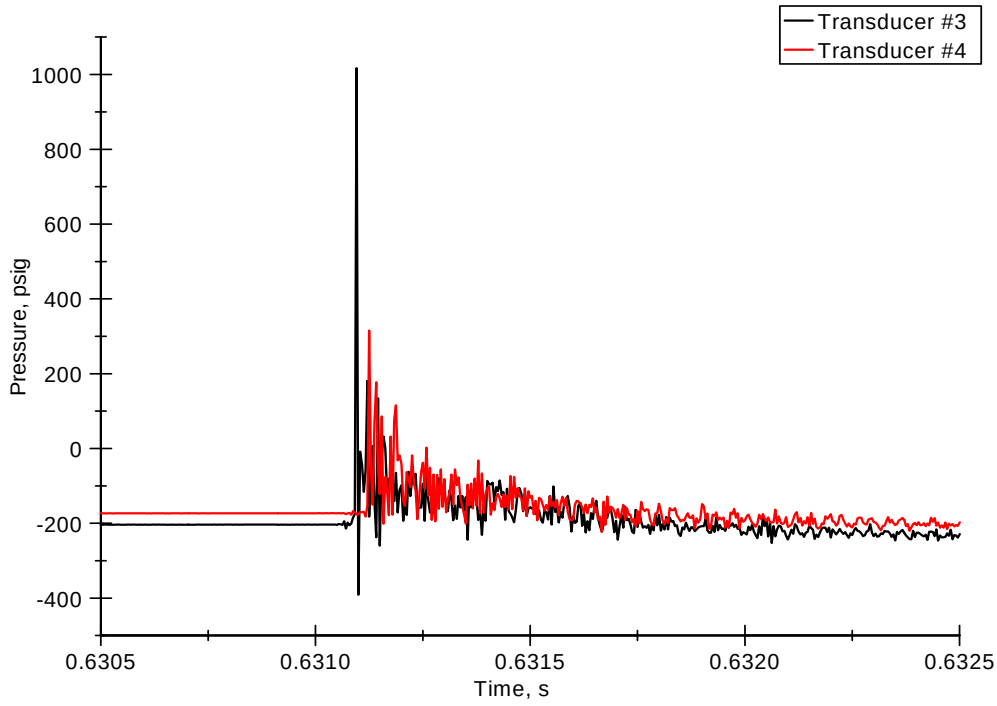

Figure 5.32. The first detonation wave pressure history for transducers #3 and 4.

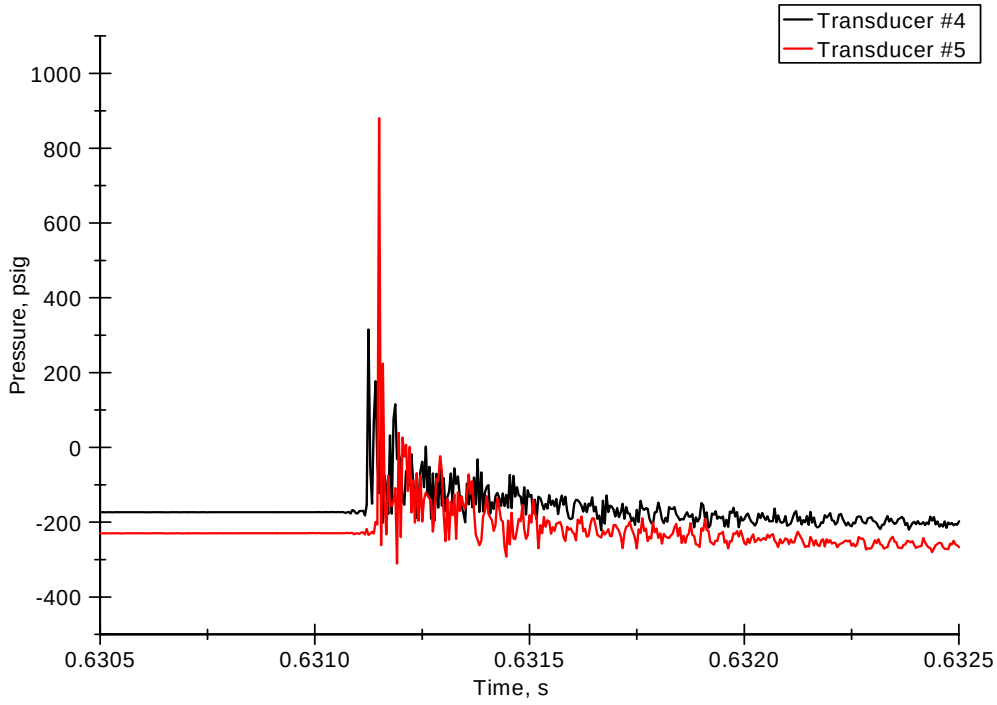

Figure 5.33. The first detonation wave pressure history for transducers #4 and 5.

Table 5.5. Time delay values for a detonation wave using various methods

	Transducers 1–2		Transducers 2–3		Transducers 3–4		Transducers 4–5		Transducers 5–6	
Method	$\bar{\tau}$, ms	$\sigma(\tau)$, ms	$\bar{\tau}$, ms	$\sigma(\tau)$, ms	$\bar{\tau}$, ms	$\sigma(\tau)$, ms	$\bar{\tau}$, ms	$\sigma(\tau)$, ms	$\bar{\tau}$, ms	$\sigma(\tau)$, ms
TOF pk-pk	0.029	–	0.025	–	0.029	–	0.025	–	0.029	–
NCCC	0.031	0.017	0.025	0.000	0.030	0.011	0.025	0.034	0.030	0.008
NHCCC	0.030	0.000	0.025	0.000	0.029	0.000	0.023	0.000	0.032	0.000
NECC	0.029	0.000	0.025	0.000	0.029	0.000	0.025	0.000	0.029	0.000
NCSDP	0.025	0.000	0.029	0.000	0.039	0.001	0.004	0.001	0.066	0.002
NCSDP-E	0.028	0.000	0.025	0.000	0.029	0.000	0.025	0.000	0.027	0.000
CSDP-2	0.028	0.000	0.024	0.000	0.043	0.001	0.007	0.002	0.040	0.000
CSDP-2E	0.028	0.000	0.023	0.000	0.028	0.001	0.024	0.000	0.031	0.001
WCCC-Haar	0.029	0.001	0.025	0.000	0.030	0.002	0.024	0.002	0.032	0.002
WCCC-Morlet	0.028	0.006	0.025	0.000	0.045	0.024	0.014	0.012	0.035	0.004
WECC-Haar	0.029	0.001	0.025	0.000	0.030	0.002	0.024	0.002	0.032	0.002
WECC-Morlet	0.028	0.006	0.025	0.000	0.045	0.024	0.014	0.012	0.035	0.004

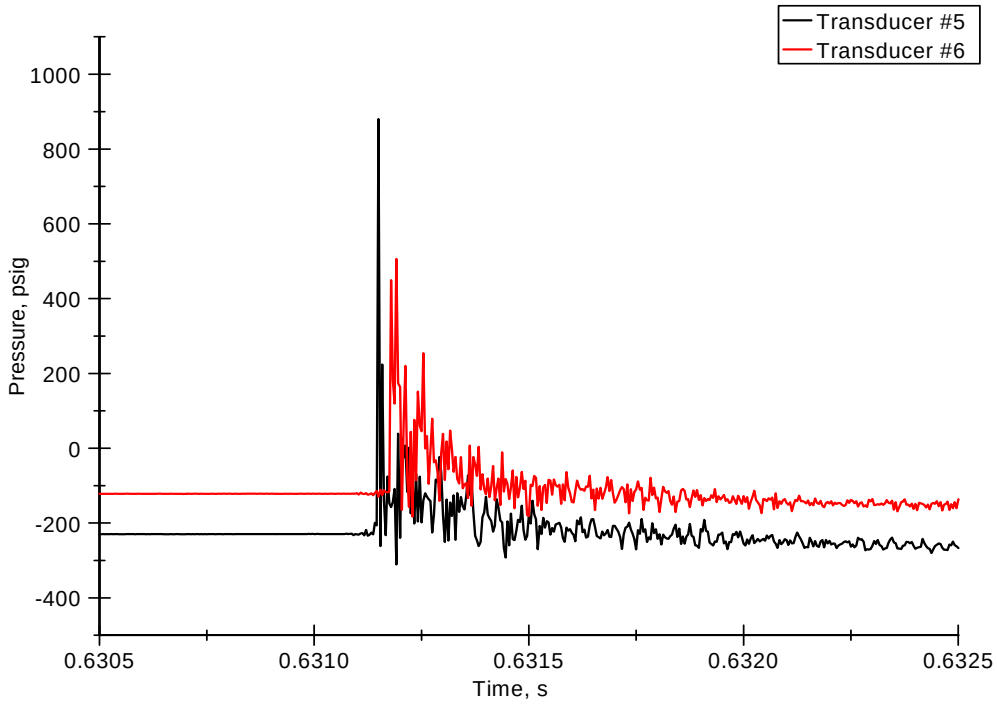

Figure 5.34. The first detonation wave pressure history for transducers #5 and 6.

violent oscillations in the leading wave. For transducers 4–5, the oscillations caused a negative time delay effect on the estimate.

The NCCC for these cases are shown in Figs. 5.35–5.37. The violent oscillations have an effect on the NCCC results as the variation for these cases are rather large as shown in the standard deviation column for Table 5.5. In Fig. 5.35, the expected time delay is seen in red. The correlation due to the oscillations are seen as the green band sections to the right of the expected time delay. The oscillations for the case where the upper time index value (U) is at a maximum appears to have a minimal effect on the time delay results as the expected time delay (red band) corresponds to the maximum value for all the lower time index values. However, the figure only represents one upper time index value that is not affected by the oscillations. This

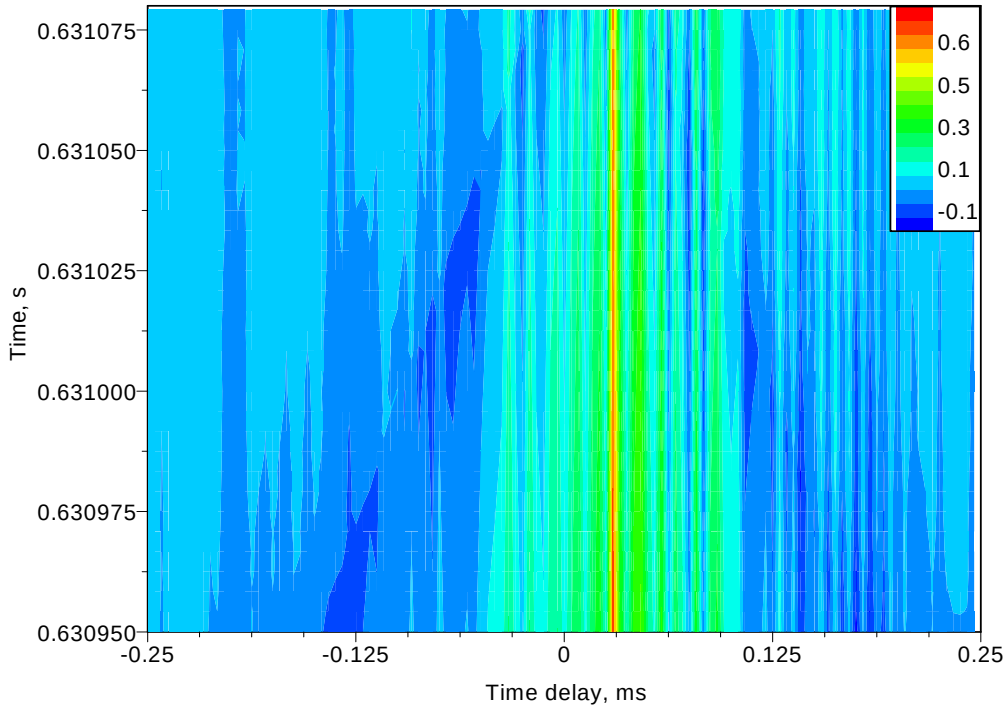

Figure 5.35. The NCCC result with a constant upper time limit for a detonation wave captured by transducers 3–4 shown in Fig. 5.32.

is misleading because the final time delay estimate has a large variation. The large variation is manifested by the standard deviation column in Table 5.5.

For transducers 4–5, the expected time delay results is also seen in red in Fig. 5.36. Since the initial pressure wave contained the violent oscillations, several correlated values exist to the left of the expected value. These correlated values are seen as yellow and light orange bands to the left of the expected time delay value (dark red). These spurious values are of concern because their significance is strong. Similar to transducer 3–4, the figure for transducer 4–5 is misleading as it represents only one upper time index (U) value. For other upper time indexes, the violent oscillation become significant enough to provide a stronger correlation for the NCCC method than the time delay between the shock fronts. These spurious values contribute to

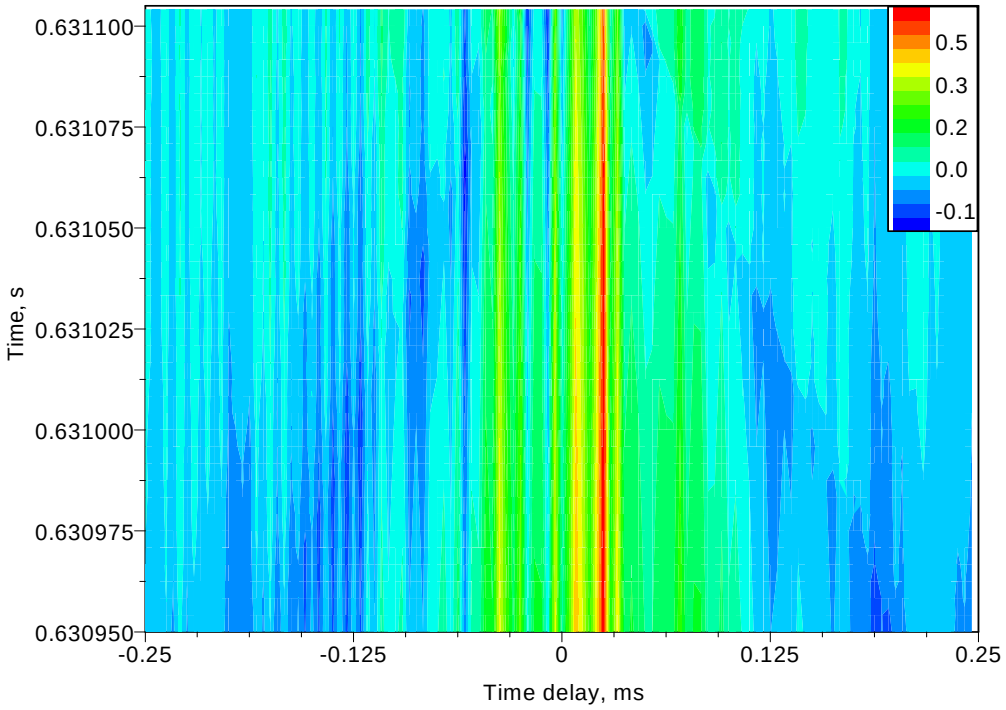

Figure 5.36. The NCCC result with a constant upper time limit for a detonation wave captured by transducers 4–5 shown in Fig. 5.33.

the large variance for the time delay estimate as shown by the standard deviation column for Table 5.5.

For transducers 5–6, a similar result occurs with the time delay seen in dark red in Fig. 5.37. Violent oscillations yielded a significant correlated band (light orange) to the right of the time delay estimate. The NCCC appears again to properly distinguish the time delay estimated by the TOF method without any variation. However, the violent oscillations have an effect on the time delay results at other values of the upper time index (U).

The NHCCC for transducers 3–4, 4–5 and 5–6 are shown in Fig. 5.38–5.40. Violent oscillations caused the NHCCC to have multiple zero crossings. For all the cases, the time delay estimate is determined by the zero crossing between the two extrema. The maximum HCCC value is shown in dark red and the minimum value is

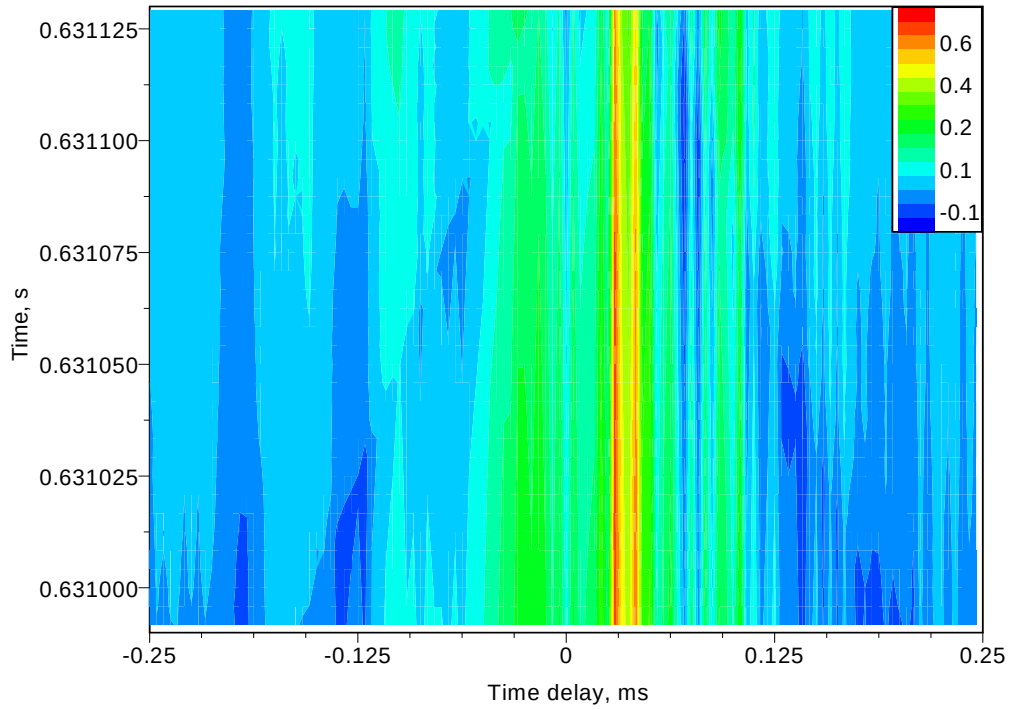

Figure 5.37. The NCCC result with a constant upper time limit for a detonation wave captured by transducers 5–6 shown in Fig. 5.34.

shown in dark blue. For transducers 3–4, the violent oscillations have multiple zero crossings that occur to the left of the expected time delay value as shown in Fig. 5.38, which represents larger time delay values. These multiple crossings are difficult to visualize with a contour plot, so a waterfall plot was used. The multiple zero crossings occur at larger time delay values due to the violent oscillations contained in the following signal.

For transducers 4–5 in Fig. 5.39, the oscillations are represented by multiple zero crossings that occur to the right (negative time delay) of the expected time delay value. Transducers 5–6 in Fig. 5.40 has multiple zero crossings occurring to the left of the expected time delay since the strong oscillations occur for the delayed signal as shown in Fig. 5.34. For all three cases of the NHCCC, the method was able

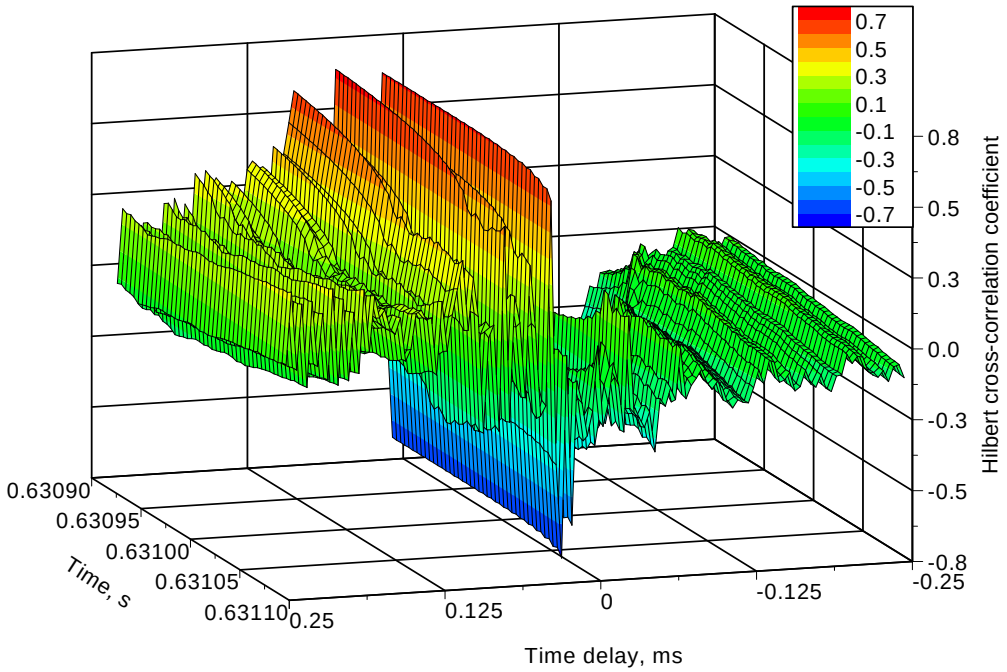

Figure 5.38. The NHCCC result with a constant upper time limit for a detonation wave captured by transducers 3–4 shown in Fig. 5.32.

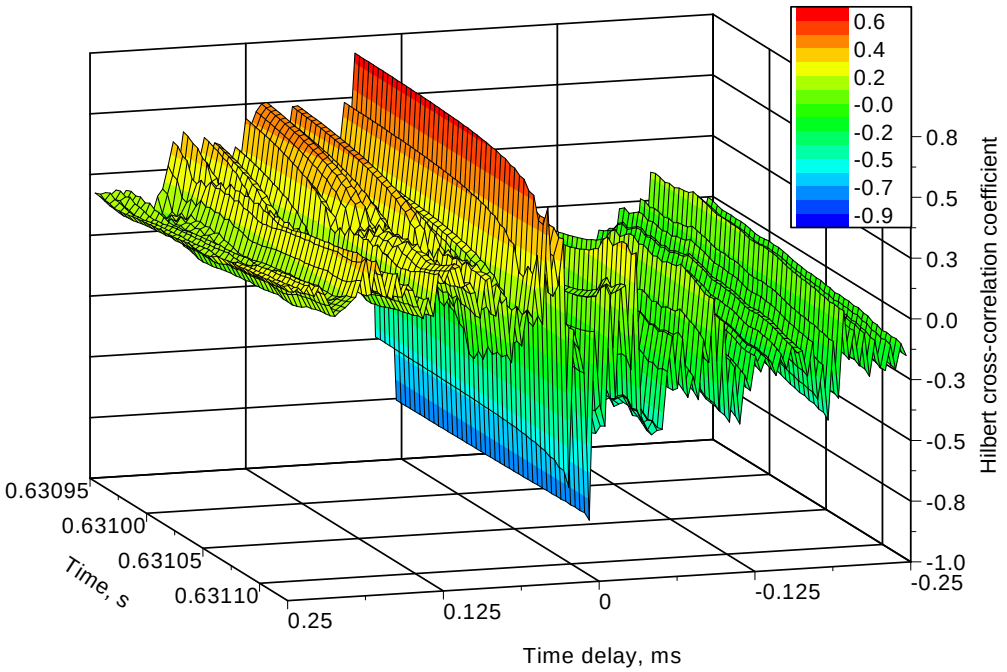

Figure 5.39. The NHCCC result with a constant upper time limit for a detonation wave captured by transducers 4–5 shown in Fig. 5.33.

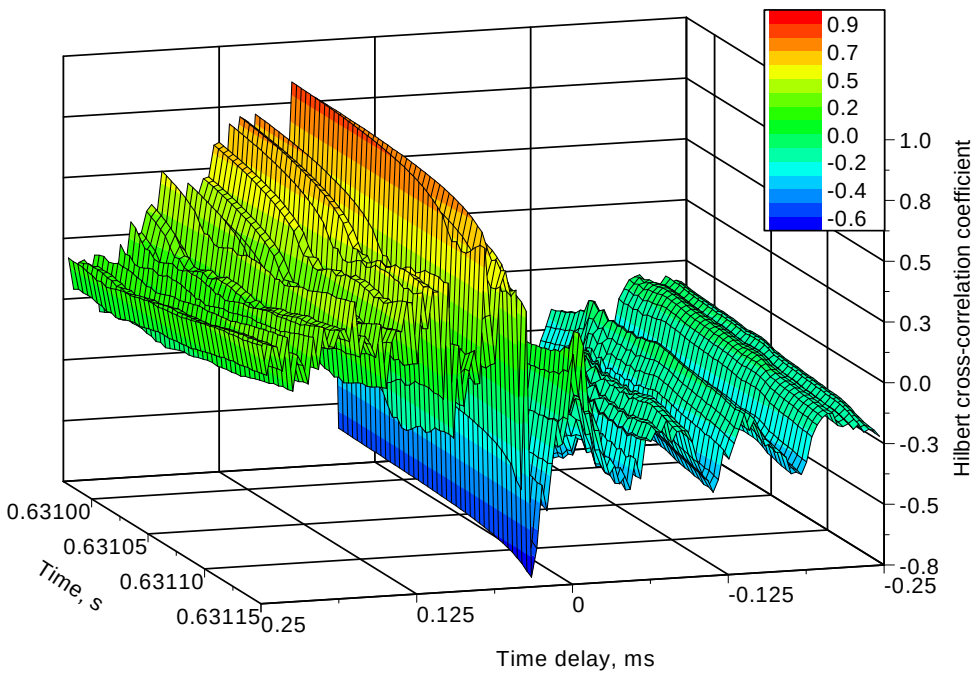

Figure 5.40. The NHCCC result with a constant upper time limit for a detonation wave captured by transducers 5–6 shown in Fig. 5.34.

to provide similar time delay results to the NCCC method, but was shown to be less prone to the varying lower time index by exhibiting zero variance.

The results for the NECC are shown in Figs. 5.41–5.43 for transducers 3–4, 4–5 and 5–6. The NECC provides similar time delay estimates to the NCCC, but the results are more distinct. The values surrounding the correlated peaks are reduced significantly, which help distinguish the time delay estimate. The violent oscillations also have an effect for the NECC method. The oscillations contributed to strong correlated peaks to the left or the right of the expected time delay. However, unlike the NCCC method that is influenced by these violent oscillations, the maximum value in the NECC method remained unphased with the varying time indexes (L and U).

The coherence of the detonation wave signals from consequent transducer pairs are shown in Figs. 5.44–5.46. The coherence value for these transducers appear to

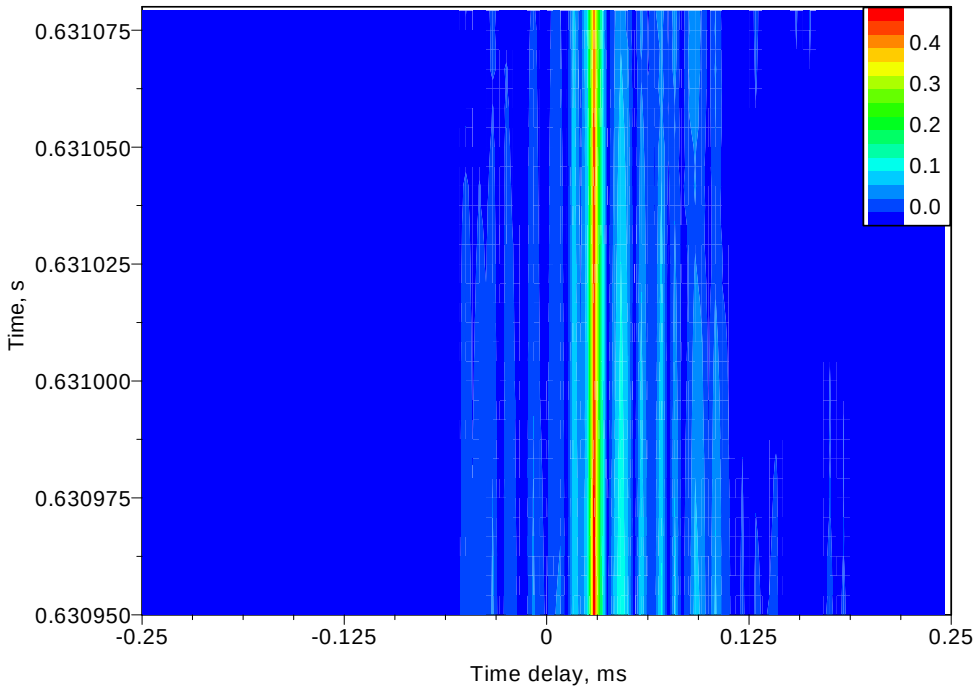

Figure 5.41. The NECC result with a constant upper time limit for a detonation wave captured by transducers 3–4 shown in Fig. 5.32.

have several areas of large uncertainty at high frequencies. Recalling from the unwrapping phase section (4.5.5) in chapter 4, all three of the coherence functions have two locations that cross the 50% limit, which requires that the phase angle to be reset to zero radians and the areas crossing the limit to be discarded to reduce the phase uncertainty. The Fourier transforms of the results from the NCCC and NECC provide the time delay estimate for the NCSDP and NCSDP-E. Since the violent oscillations influence the results for the NCCC method, the effect of the violent oscillations also translates to the NCSDP method that is a function of the NCCC. The oscillations are clearly seen to influence the estimate of the time delay for the NCSDP as displayed in Table 5.5. The effect of the oscillations caused an increase in the time delay estimate for transducers 3–4 and 5–6. The oscillations affected the time delay estimates for transducers 4–5 by skewing the estimate toward a negative delay. However, the

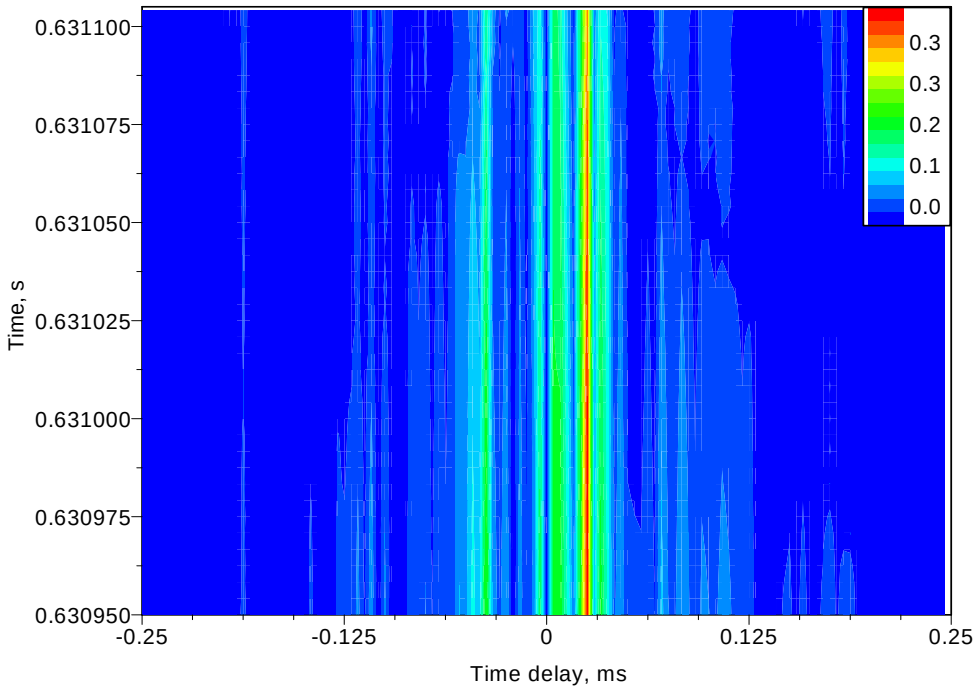

Figure 5.42. The NECC result with a constant upper time limit for a detonation wave captured by transducers 4–5 shown in Fig. 5.33.

oscillations had a minimal effect on the NCSDP-E method because the method is a function of the NECC that is less prone to the violent oscillations. The time delay results for the NCSDP-E provided similar estimates to the estimate provided by the TOF method.

The CSDP-2 and CSDP-2E methods show similar trends to that of the NCSDP and NCSDP-E methods. The CSDP-2, like the NCSDP, is influenced by the violent oscillations that skewed the time delay estimate. The CSDP-2E on the other hand is similar to the NCSDP-E. The influence of the oscillations is minimized, but it has a slight influence on the time delay estimate as it contains an uncertainty with time.

The results for the WCCC-Haar are displayed in Figs. 5.47–5.49. The relationship between the pseudo-frequencies and the scales for the PDE data is provided in Table 5.6. Further information about the scales and pseudo-frequencies is provided

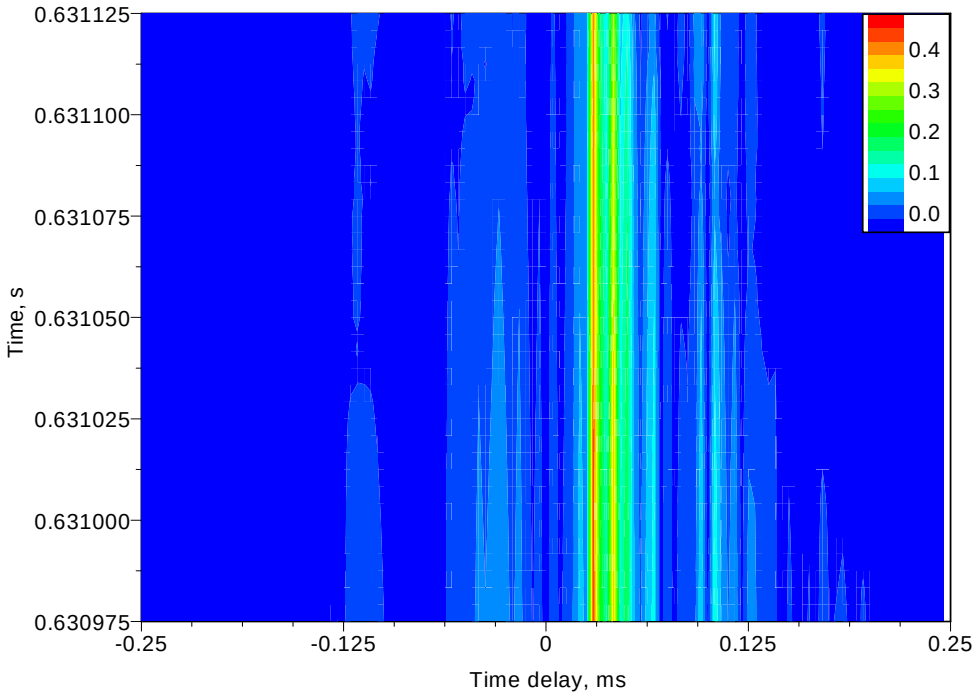

Figure 5.43. The NECC result with a constant upper time limit for a detonation wave captured by transducers 5–6 shown in Fig. 5.34.

in Appendix C. The WCCC-Haar yields results similar to the TOF method. The violent oscillations have an increased effect with the increasing scale. The effect of the oscillations can be seen graphically by the slower rolloff of the values to the left or the right of the peak value. A slower rolloff to the right indicates that the more violent oscillations are exhibited in the following signal. On the other hand, a slow rolloff to the left indicates the opposite. For transducer pairs 3–4 and 5–6, the rolloff rate was slower for the right half, which indicates that the following signal contained the oscillations. For low scales, that is, high frequencies, the effect of the oscillations was small. The opposite effect is represented by transducer pairs 4–5, where the oscillations influenced the WCCC with a slower rolloff to the left of the peak value.

The WECC-Haar results are shown in Figs. 5.50–5.52. The time delay estimates for the Haar WECC are similar to the results for the WCCC version. The envelope

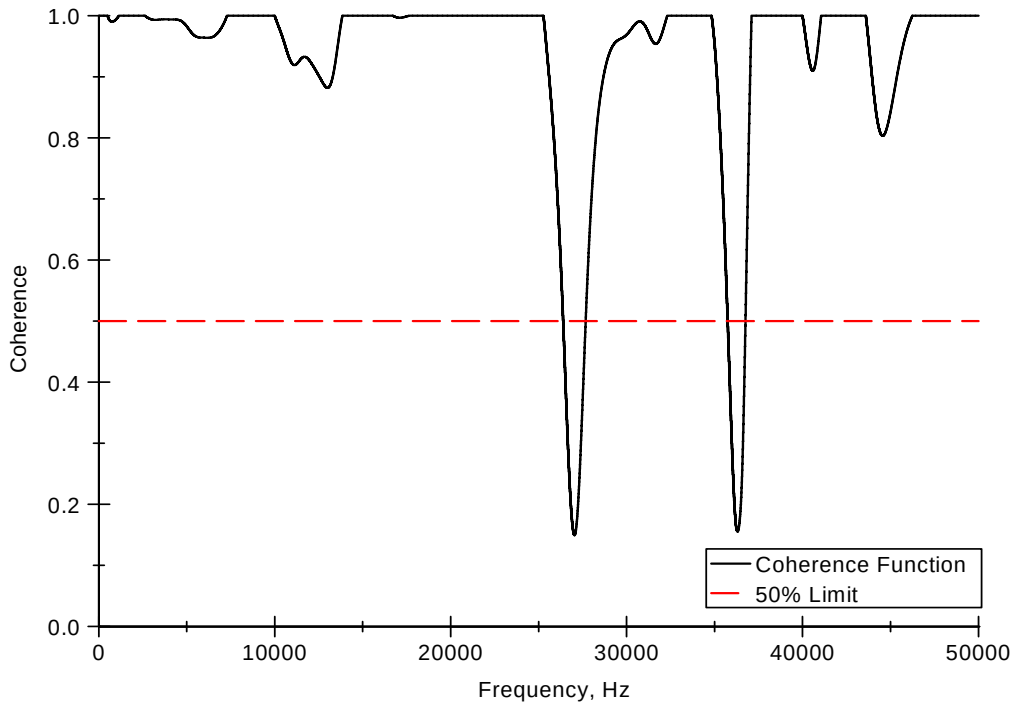

Figure 5.44. The coherence function for the first detonation wave captured by transducers 3–4 provided in Fig. 5.32.

Table 5.6. A scale to pseudo-frequency relationship for the Haar and Morlet wavelet functions for the PDE data

Scale	F_{aHaar}, Hz	$F_{aMorlet}$, Hz
4	59767	48750
8	29883	24375
12	19922	16250
16	14942	12188
20	11953	9750
24	9961	8125
28	8538	6964
32	7471	6094

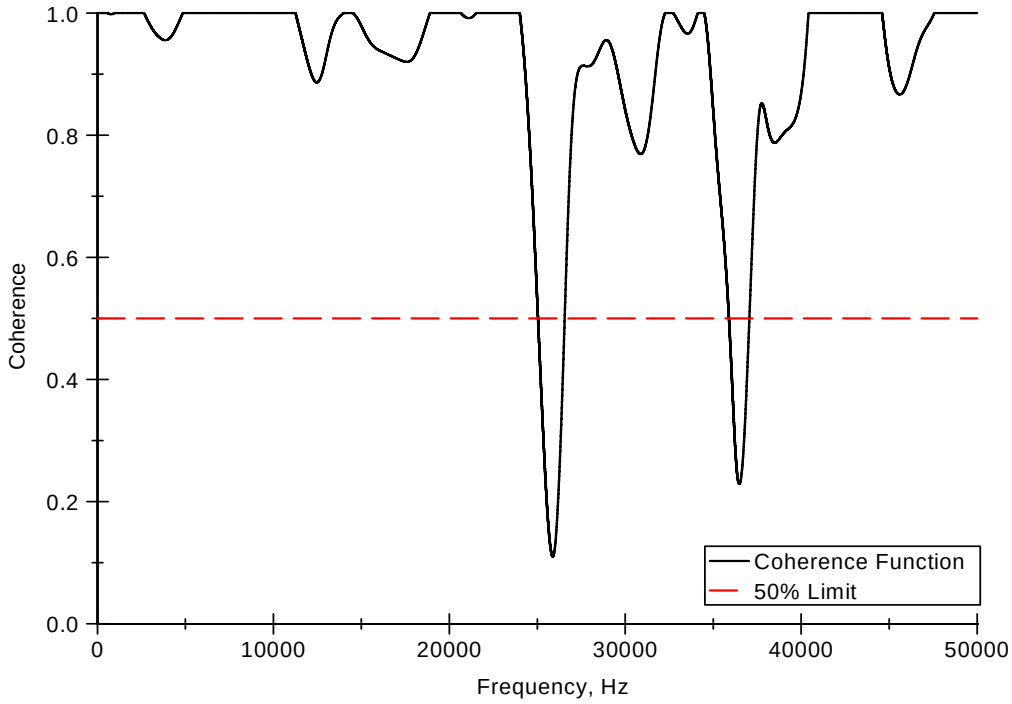

Figure 5.45. The coherence function for the first detonation wave captured by transducers 4–5 provided in Fig. 5.33.

creates a more distinctive result for the time delay estimate, as the peak value is sharper. The effect of the oscillations is also exhibited for the WECC-Haar method, but at a reduced magnitude relative to the peak value.

The WCCC-Morlet method results are shown in Figs. 5.53–5.55. Unlike the WCCC-Haar method, the Morlet variation yields large uncertainty in the time delay estimate. Like the WCCC-Haar and WECC-Haar, the effect of the oscillations can be seen graphically by a slower rolloff to the left or the right of the peak value. For transducers 3–4 and 5–6, the oscillations increase the time delay. The WCCC results for transducer 3–4 for scales 14 and higher have a distinct region that corresponds to the expected time delay. For lower scales (higher frequencies), the WCCC exhibits strong correlations at a larger time delay. The results from transducers 4–5 show many highly correlated values at various time delays. For low scales (high frequencies), the

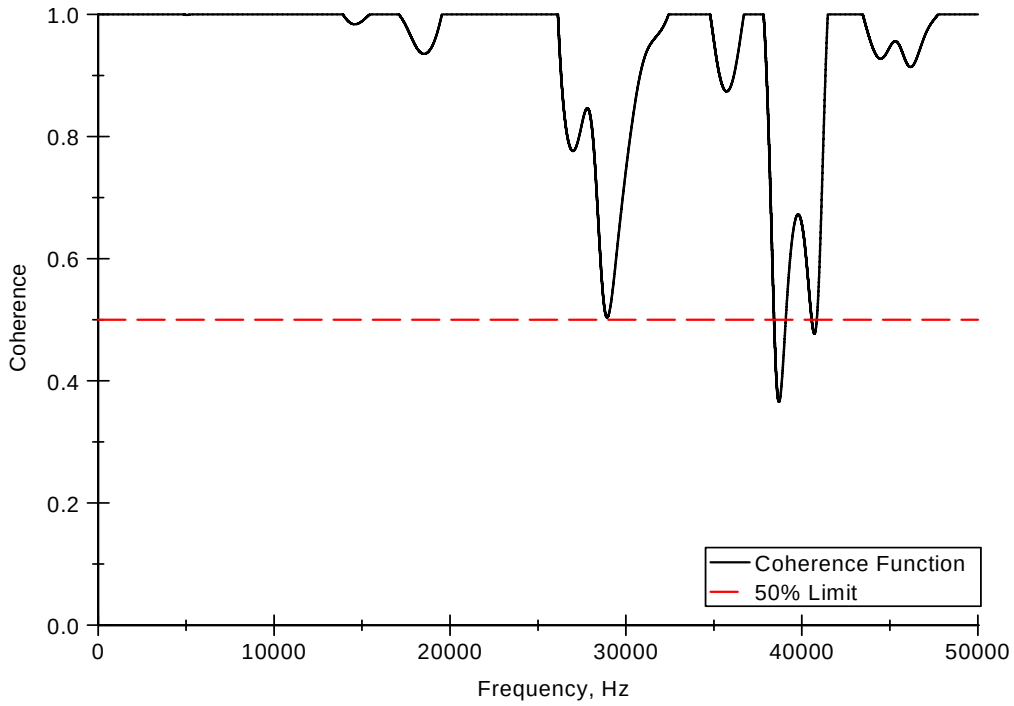

Figure 5.46. The coherence function for the first detonation wave captured by transducers 5–6 provided in Fig. 5.34.

time delay is shifted negatively. For intermediate scales (12–20), there is a positive shift. And for large scales (low frequencies), multiple regions contain highly correlated values. The results for transducers 5–6 are less influenced by the oscillations, but still have areas of large correlations outside the expected time delay. Similar to the phase methods described above, the oscillations increase the time delay estimate for transducers 5–6.

The results for WECC-Morlet are shown in Figs. 5.56–5.58. The results for the WCCC and WECC for the Morlet wavelet provide similar estimates. The violent oscillations still had an effect that skews the time delay estimate. The Morlet wavelet appears to be unable to properly yield the time delay estimate as the time localization of the wavelet is not adequate for impulse-like functions.

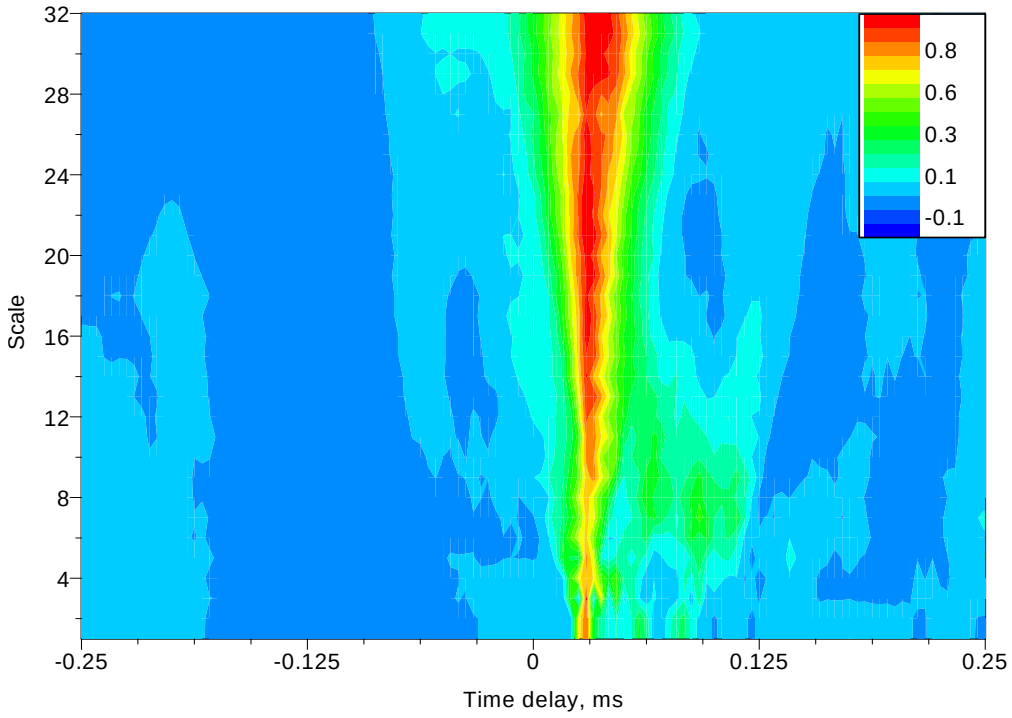

Figure 5.47. The WCCC-Haar result with a constant upper time limit for a detonation wave captured by transducers 3–4 is provided in Fig. 5.32.

The use of the 50% cutoff and filtering for both the Haar and Morlet methods had no effect on the time delay estimates. The cutoff was not required for any of the PDE cases because the signals power diminished near the edge of the window and the delay between the signals was relatively small compared to the size of the time window. Whereas for the shock tube experiment, the signal did not diminish near the edge of the time window. Also the time delay between the signals relative to the time window was much larger for the shock tube data.

The results for the following detonation waves are provided in Table 5.7 and 5.8. Referring to both tables, it appears that the NECC, WCCC-Haar and WECC-Haar method all provide similar results to the TOF method. The NECC tends to rarely have any variance for the time delay estimate. Whereas both the Haar methods

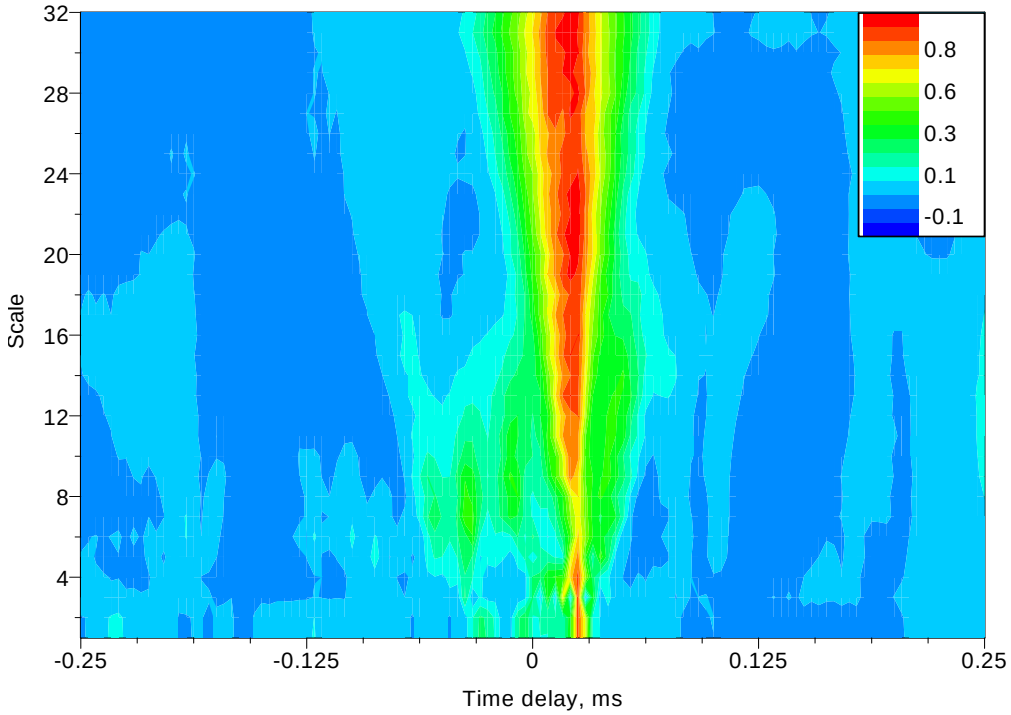

Figure 5.48. The WCCC-Haar result with a constant upper time limit for a detonation wave captured by transducers 4–5 is provided in Fig. 5.33.

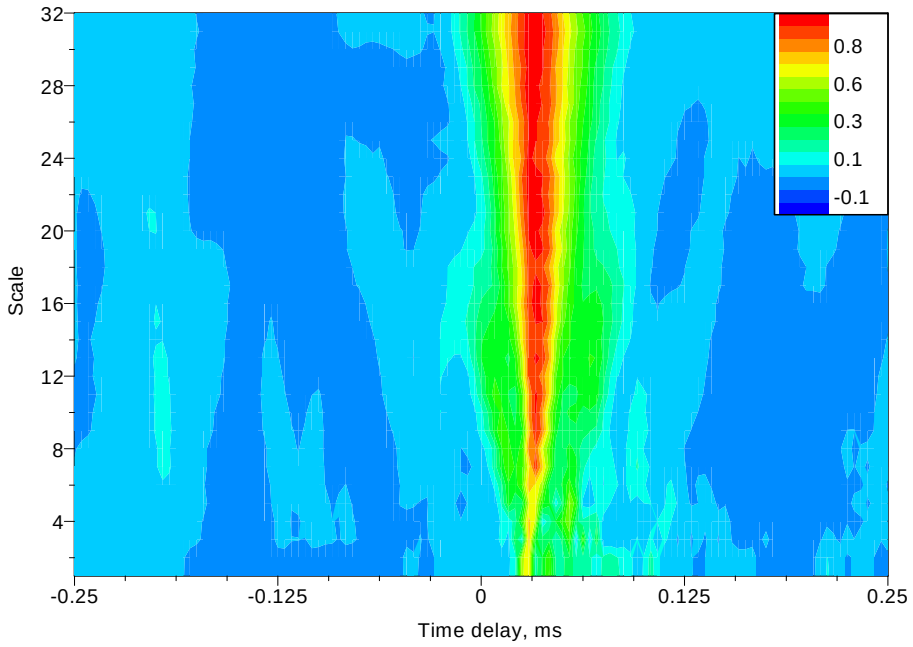

Figure 5.49. The WCCC-Haar result with a constant upper time limit for a detonation wave captured by transducers 5–6 is provided in Fig. 5.34.

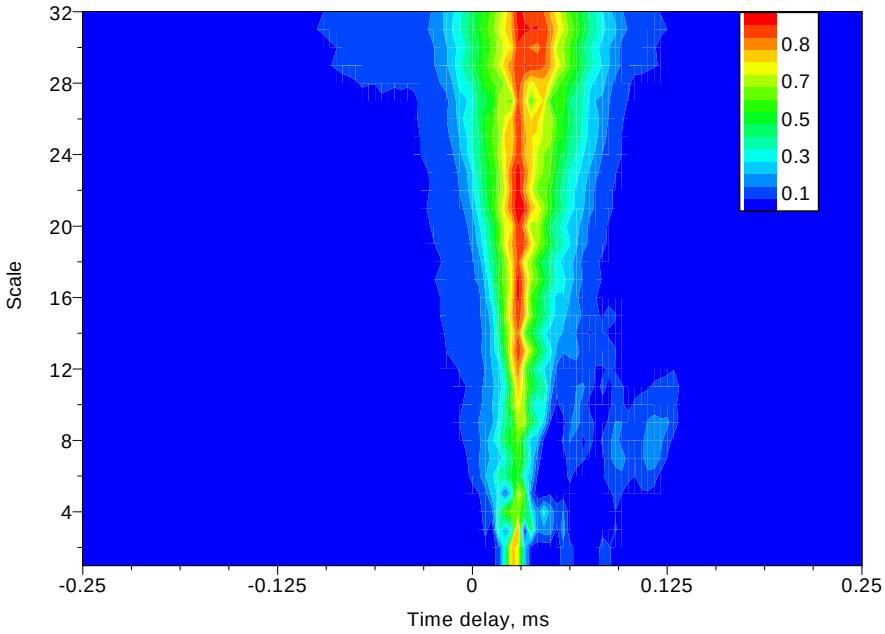

Figure 5.50. The WECC-Haar result with a constant upper time limit for a detonation wave captured by transducers 3–4 is provided in Fig. 5.32.

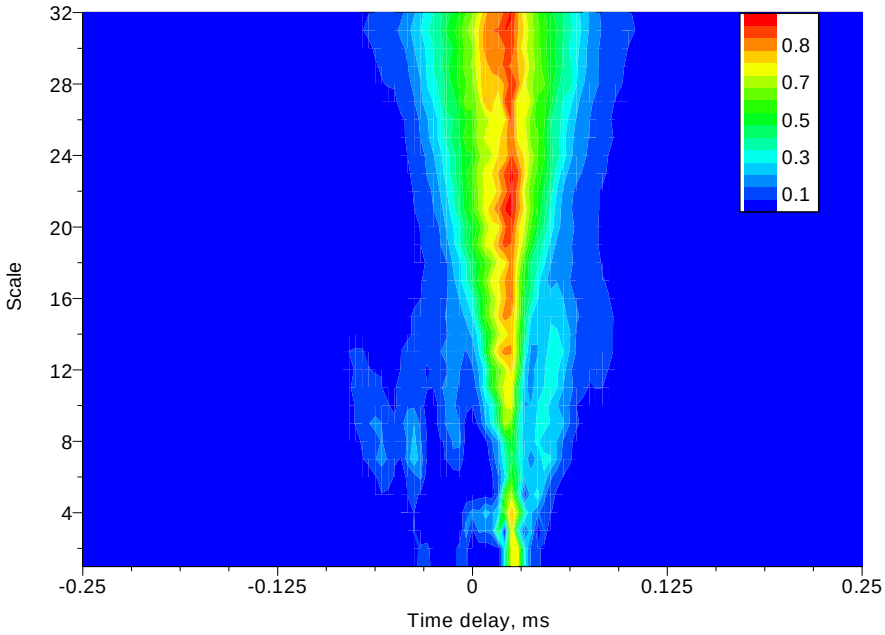

Figure 5.51. The WECC-Haar result with a constant upper time limit for a detonation wave captured by transducers 4–5 is provided in Fig. 5.33.

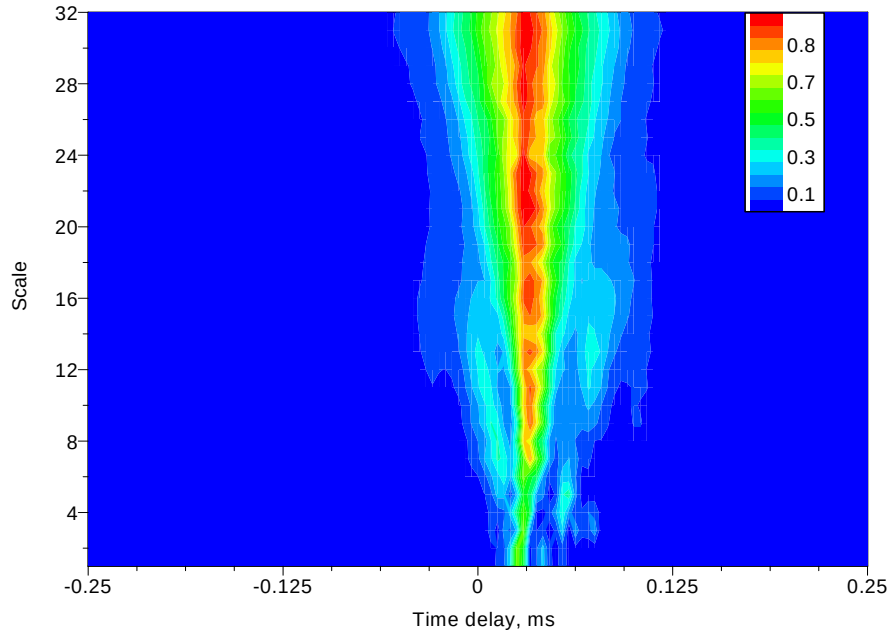

Figure 5.52. The WECC-Haar result with a constant upper time limit for a detonation wave captured by transducers 5–6 is provided in Fig. 5.34.

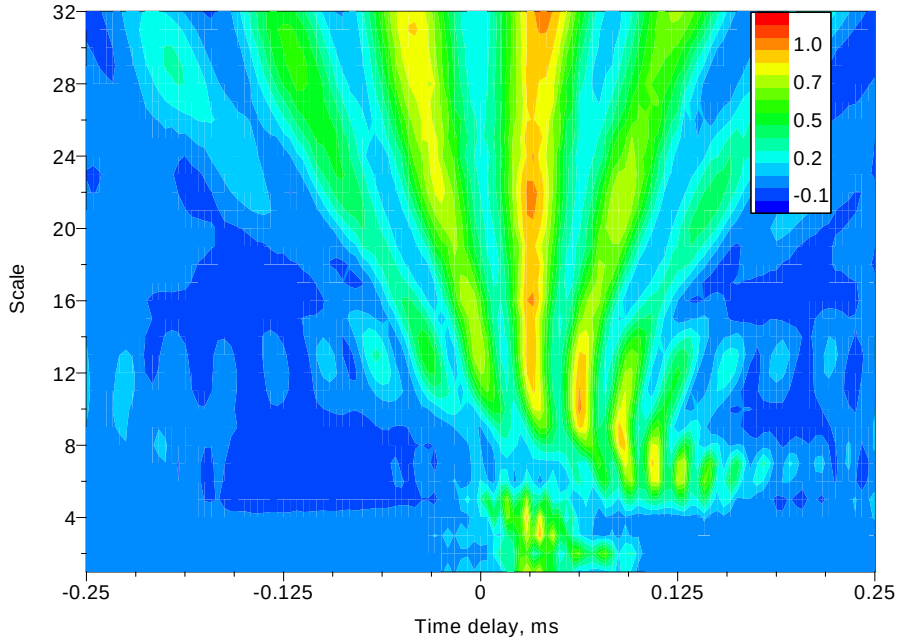

Figure 5.53. The WCCC-Morlet result with a constant upper time limit for a detonation wave captured by transducers 3–4 is provided in Fig. 5.32.

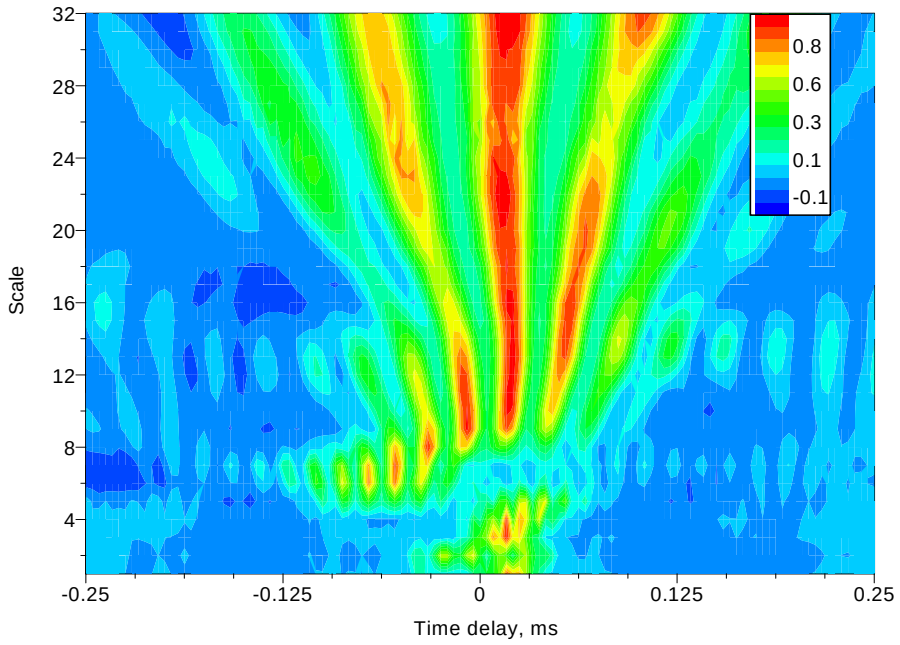

Figure 5.54. The WCCC-Morlet result with a constant upper time limit for a detonation wave captured by transducers 4–5 is provided in Fig. 5.33.

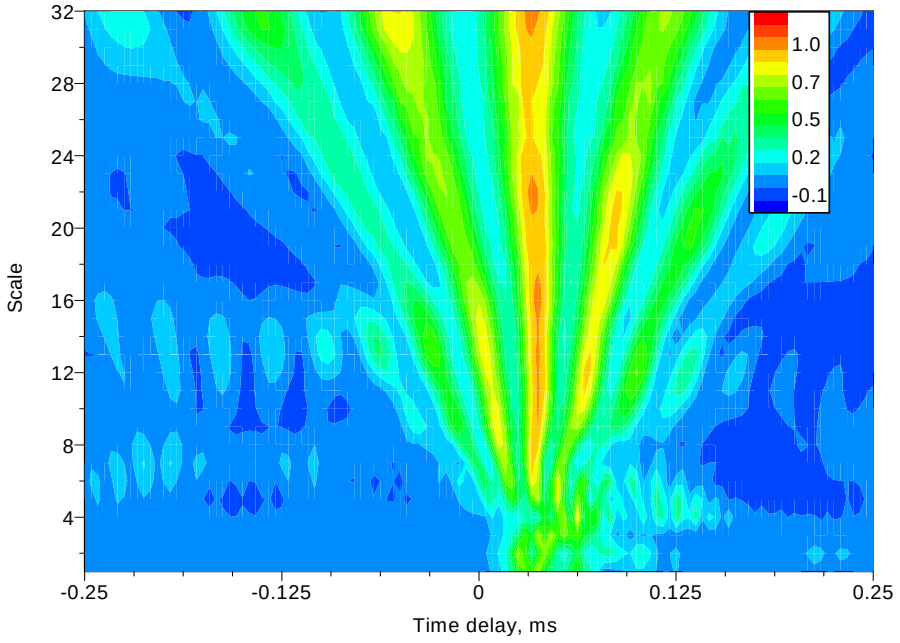

Figure 5.55. The WCCC-Morlet result with a constant upper time limit for a detonation wave captured by transducers 5–6 is provided in Fig. 5.34.

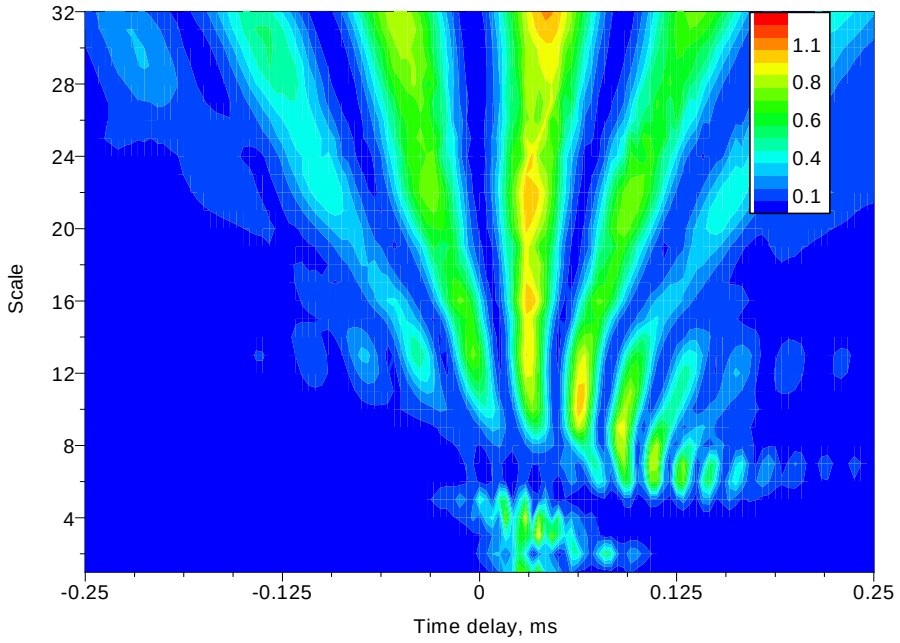

Figure 5.56. The WECC-Morlet result with a constant upper time limit for a detonation wave captured by transducers 3–4 is provided in Fig. 5.32.

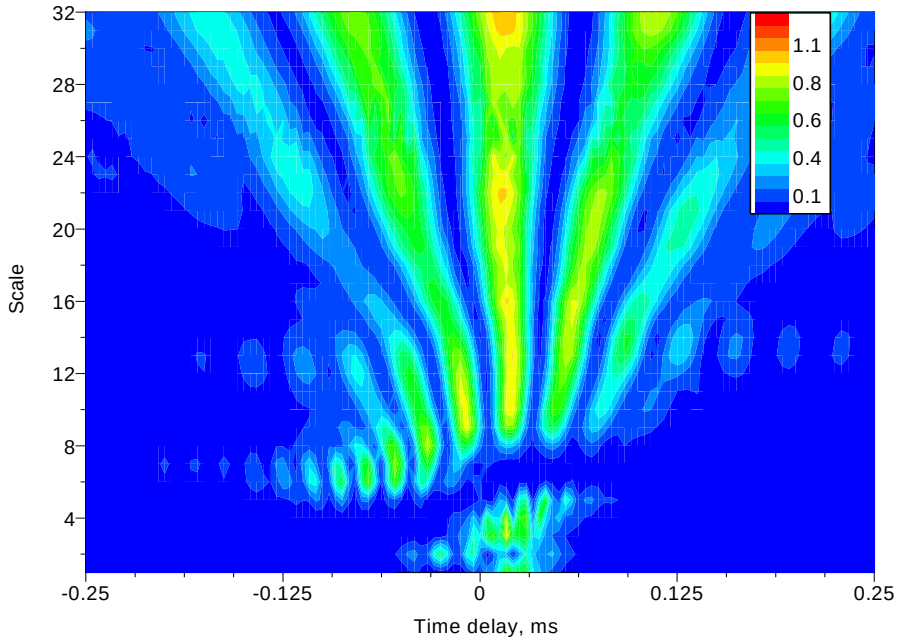

Figure 5.57. The WECC-Morlet result with a constant upper time limit for a detonation wave captured by transducers 4–5 is provided in Fig. 5.33.

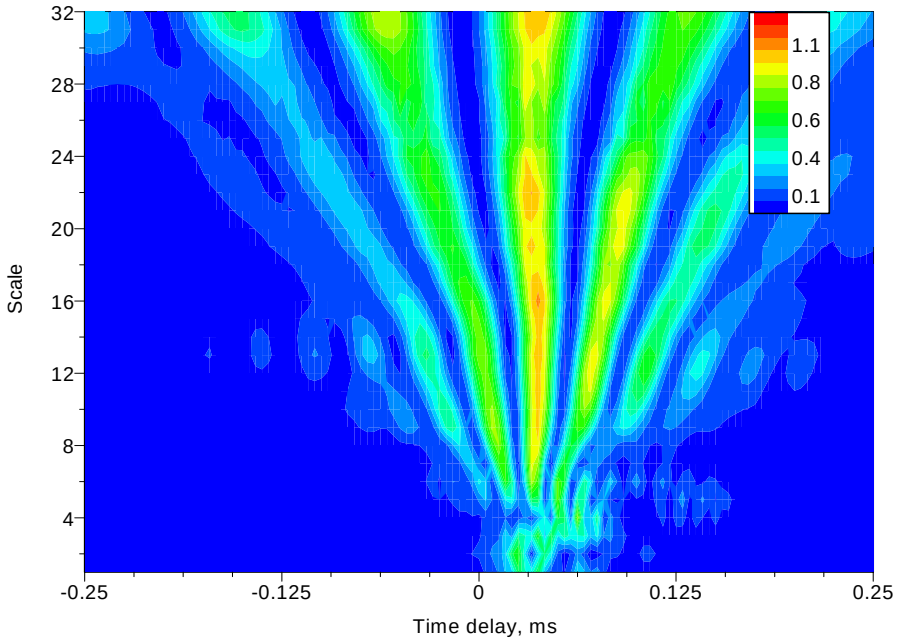

Figure 5.58. The WECC-Morlet result with a constant upper time limit for a detonation wave captured by transducers 5–6 is provided in Fig. 5.34.

provide identical results for all scales. The Haar methods results exhibit a small variance for the time delay estimate.

The methods that utilize the envelope function appear to only improve the time delay estimate. The improvement is clearly seen by comparing the results for the NCSDP to the NCSDPE and for the CSDP-2 to the CSDP-2E methods. The results for the NCCC indicate that the method is prone to violent oscillations as shown by several of the results in Tables 5.7 and 5.8. The NCCC results exhibit large variations and, for severe oscillations, the NCCC method reports incorrect estimates for the time delay.

Table 5.7. Time delay values for the second detonation wave shown in Fig. 5.29 using various methods

	Transducers 1–2		Transducers 2–3		Transducers 3–4		Transducers 4–5		Transducers 5–6	
Method	$\bar{\tau}$, ms	$\sigma(\tau)$, ms	$\bar{\tau}$, ms	$\sigma(\tau)$, ms	$\bar{\tau}$, ms	$\sigma(\tau)$, ms	$\bar{\tau}$, ms	$\sigma(\tau)$, ms	$\bar{\tau}$, ms	$\sigma(\tau)$, ms
TOF pk-pk	0.029	–	0.025	–	0.025	–	0.029	–	0.050	–
NCCC	0.263	0.486	-0.093	0.282	0.025	0.001	0.029	0.000	0.034	0.011
NHCCC	0.043	0.001	0.018	0.010	0.025	0.000	0.028	0.000	0.043	0.000
NECC	0.032	0.010	0.025	0.000	0.025	0.000	0.029	0.000	0.033	0.000
NCSDP	0.020	0.004	0.018	0.001	0.036	0.008	0.008	0.012	0.065	0.001
NCSDP-E	0.026	0.000	0.023	0.006	0.025	0.000	0.029	0.000	0.049	0.000
CSDP-2	0.033	0.002	0.012	0.004	0.025	0.001	0.029	0.003	0.048	0.002
CSDP-2E	0.034	0.001	0.018	0.001	0.022	0.000	0.030	0.001	0.032	0.000
WCCC-Haar	0.026	0.001	0.026	0.002	0.026	0.002	0.029	0.002	0.042	0.004
WCCC-Morlet	0.068	0.093	-0.069	0.181	0.036	0.034	0.019	0.031	0.046	0.008
WECC-Haar	0.026	0.001	0.026	0.002	0.026	0.002	0.029	0.002	0.042	0.004
WECC-Morlet	0.068	0.093	-0.069	0.181	0.036	0.034	0.019	0.031	0.046	0.008

Table 5.8. Time delay values for the third detonation wave shown in Fig. 5.29 using various methods

	Transducers 1–2		Transducers 2–3		Transducers 3–4		Transducers 4–5		Transducers 5–6	
Method	$\bar{\tau}$, ms	$\sigma(\tau)$, ms	$\bar{\tau}$, ms	$\sigma(\tau)$, ms	$\bar{\tau}$, ms	$\sigma(\tau)$, ms	$\bar{\tau}$, ms	$\sigma(\tau)$, ms	$\bar{\tau}$, ms	$\sigma(\tau)$, ms
TOF pk-pk	0.046	–	0.008	–	0.046	–	0.008	–	0.050	–
NCCC	0.232	0.507	-0.137	0.367	0.136	0.357	0.034	0.146	0.050	0.006
NHCCC	0.026	0.000	0.002	0.001	0.044	0.000	0.020	0.013	0.047	0.001
NECC	0.025	0.000	0.008	0.000	0.046	0.000	0.029	0.000	0.050	0.000
NCSDP	0.015	0.014	0.019	0.001	0.038	0.000	0.016	0.001	0.037	0.010
NCSDP-E	0.026	0.000	0.006	0.007	0.048	0.000	0.007	0.000	0.071	0.000
CSDP-2	0.041	0.003	0.007	0.004	0.051	0.003	0.002	0.003	0.056	0.003
CSDP-2E	0.039	0.002	0.012	0.002	0.060	0.002	-0.009	0.002	0.041	0.004
WCCC-Haar	0.026	0.002	0.027	0.003	0.038	0.013	0.022	0.006	0.046	0.003
WCCC-Morlet	0.128	0.182	-0.148	0.290	0.044	0.016	0.011	0.019	0.050	0.009
WECC-Haar	0.026	0.002	0.027	0.003	0.038	0.013	0.022	0.006	0.046	0.003
WECC-Morlet	0.128	0.182	-0.148	0.290	0.044	0.016	0.011	0.019	0.050	0.009

CHAPTER 6

UNCERTAINTY ANALYSIS

6.1 Uncertainty in the Velocity Estimation

The wave propagation uncertainty can now be determined with the use of the propagation time estimates obtained by the methods provided in Chapter 4. The velocity of the disturbance is typically determined by estimating the time delay between two transducers with a known separation. The velocity for the propagating wave can be determined by

$$\hat{V} = \frac{\Delta L}{\hat{\tau}} \tag{6.1}$$

where ΔL represents the separation between two transducers.

6.1.1 Propagation of Error

In order to determine the uncertainty in the velocity estimate, the uncertainties of all the parameters used to determine the velocity need to be accounted for. The velocity estimate has two main parameters, which are the separation distance and the time delay between the two transducers. The propagation of the uncertainty can be estimated by

$$u_V = \pm\sqrt{\sum_{i=1}^{n} \left(\theta_i u_{x_i}\right)^2 (P\%)}\,, \quad i = 1, 2, \ldots, n \tag{6.2}$$

where θ_i is the sensitivity index, $P\%$ is the probability level and u_{x_i} is the uncertainty associated with the best estimate of parameter x_i [16]. Generally a probability level of 95% is used to define all uncertainty calculations, which helps to define a standard

to maintain consistency amongst engineers [16]. Applying Eqn. (6.1) to Eqn. (6.1) yields

$$u_V = \pm\sqrt{\left(\frac{1}{\hat{\tau}}\frac{\delta V}{\delta x}\right)^2 + \left(\frac{-\Delta L}{\hat{\tau}^2}\frac{\delta V}{\delta \tau}\right)^2}\,(P\%) \tag{6.3}$$

which indicates that the uncertainty associated with the separation distance and the time delay needs to be determined.

6.1.2 Elemental Error for the System

The elemental errors are the propagating wave are the separation distance and the propagating time. The errors associated with determining the separation distance between the two transducers is provided by known tolerances. The tolerances consist of the machining tolerance for locating the instrumentation port and the manufacturing tolerance for the transducer's diameter which are respectively 0.01 and 0.001 inch. Since two transducers are used to determine the wave propagation speed, the tolerances are doubled to account for both transducers. The uncertainty associated by the separation distance between the two transducers can be computed by applying the root sum square (RSS) method. The RSS method is used to combine elemental errors to provide a better estimate of the uncertainty for a given parameter (separation distance). The RSS can be written as

$$u_i = \pm\sqrt{\sum_{i=1}^{n} e_i^2}\,(P\%)\,, \quad i = 1, 2, \ldots, n \tag{6.4}$$

Applying the RSS method for the separation distance between the transducers with a 95% confidence is given by

$$\frac{\delta V}{\delta x} = \pm\sqrt{e_{machining}^2 + e_{xdr}^2}\,(95\%) \tag{6.5}$$

where $e_{machining}$ and e_{xdr} represent twice the tolerance value for the machining of the port and the manufacturing of the transducer.

The uncertainty associated with the time is estimated by a similar approach. The time uncertainty accounts for the time resolution, the rise time for the system and the uncertainty provided by the methods for time delay estimate. The uncertainty for time with a 95% confidence is given by

$$\frac{\delta V}{\delta \tau} = \pm \sqrt{u_0^2 + e_r^2 + \left(t_{\nu,95}\sigma\left(\tau\right)\right)^2}\,(95\%) \tag{6.6}$$

where u_0 is the resolution uncertainty and e_r is the inherent error associated with the rise time for the system. The resolution uncertainty is half the time resolution. However, like the tolerances for the machining and manufacturing the resolution uncertainty has to be doubled to account for both transducers and is provided by

$$u_0 = 2\frac{1}{2f_s} = \frac{1}{f_s} \tag{6.7}$$

The inherent error associated with the rise time requires the use of the RSS method. The RSS method is needed to combine all the rise times values for the data acquisition system. The rise time associated with the chassis (NI 1042Q) and the cables were ignored as their rise time values are negligible compared to the rest of the system. The rise time for the pressure transducer $t_{r,XDR}$, signal conditioner $t_{r,SC}$, DAQ card $t_{r,DAQ}$ and the mounting of the transducer $t_{r,recessed}$ were accounted for in the determination of the error associated with the rise time for the system. Some of the known properties for the individual components are provided in Table 6.1. The properties from the table can be used to determine an estimate of the rise time for each component. A rule of thumb can be used to associate the -3 dB bandwidth $f_{-3\text{dB}}$ with rise time:

$$t_r f_{-3\text{dB}} = 0.35 \quad \text{to} \quad 0.45 \tag{6.8}$$

where 0.45 provides a conservative estimate [32].

The rise time for each component was computed by the conservative estimate and is shown in Table 6.2.

Table 6.1. Some of the known properties for the entire system

Component	$f_{-3\text{dB}}$, MHz	t_r, μs
PCB Pressure Transducer (Model 111A24)	–	$\leq$1.5
PCB Signal Conditioner (Model 483A)	1	–
NI 6133 DAQ Card	1.3	–

Table 6.2. Rise time estimates for several components

Component	Rise time, μs
PCB Pressure Transducer (Model 111A24)	$\leq$1.50
PCB Signal Conditioner (Model 483A)	0.45
NI 6133 DAQ Card	0.35
Recessed effect (1/8 in.)	3.34

The mounting of the transducer to the detonation tube can also contribute to the rise time error [33]. Since the pressure transducers were recessed to prevent damage by the extreme heat associated with the energy release by the detonation wave, a cavity is introduced that undergoes a phenomenon known as Helmholtz resonance. Helmholtz resonance can be represented by

$$F_r = \frac{a_{sound}}{4L_{col}} \tag{6.9}$$

where L_{col} is the length of the cavity and a_{sound} is the speed of sound in the gas. The length of the cavity is estimated to be 1/8 inch. The speed of sound of the gas is an unknown, and is approximated by the speed of sound for the Chapman–Jouguet (CJ) detonation solution provided by CEA. Some of the properties provided by CEA are shown in Table 6.4. The rise time produced by cavity can be approximated by

$$t_{r,recessed} \approx \frac{1}{3F_r} \tag{6.10}$$

An approximated rise time that is introduced by recessing the transducers is shown in Table 6.2.

Table 6.3. Some of the CEA Chapman–Jouguet detonation properties for a stochiometric propane–oxygen mixture

Property	English	SI
a_{sound}	4163 ft/s	1269 m/s
P/P_1	35.951	
T/T_1	12.742	
V_{CJ}	7732 ft/s	2356.6 m/s

The inherent error associated with the rise time can now be determined by

$$e_r = \sqrt{(2t_{r,XDR})^2 + (2t_{r,SC})^2 + (2t_{r,DAQ})^2 + (2t_{r,recessed})^2} \tag{6.11}$$

The standard deviation of the time delay estimate was multiplied by 1.96 to achieve a 95% confidence. The 1.96 value was determined by infinite statistics at a 95% probability level, and it was assumed that the results followed a normal distribution. The uncertainty in time can now be determined and used to compute the uncertainty in the velocity estimate. The TOF, NECC and WCCC-Haar method were used to determine the velocity estimates and uncertainty for the second detonation wave data provided in Table 5.7. The results for these methods are provided in Table 6.5. The velocity estimates are also compared to the CJ detonation velocity in Fig. 6.1. The error bars (blue and black) provided represent the 95% confidence intervals for the NECC and WCCC-Haar method. The transducer locations are provided in Table 6.4. Referring to Fig. 6.1, the NECC and WCCC-Haar methods tend to share the same confidence intervals for the velocity estimate. The velocity estimate with uncertainty for transducers 1–2 and 5–6 are the only estimates that differ significantly. For transducers 1–2, the NECC method provides a large uncertainty for the velocity estimate. The uncertainty is large enough to include the entire estimate provided by the WCCC-Haar method. For transducers 5–6, the two methods differ the most, which is clearly seen by a large portion of the confidence intervals not overlapping

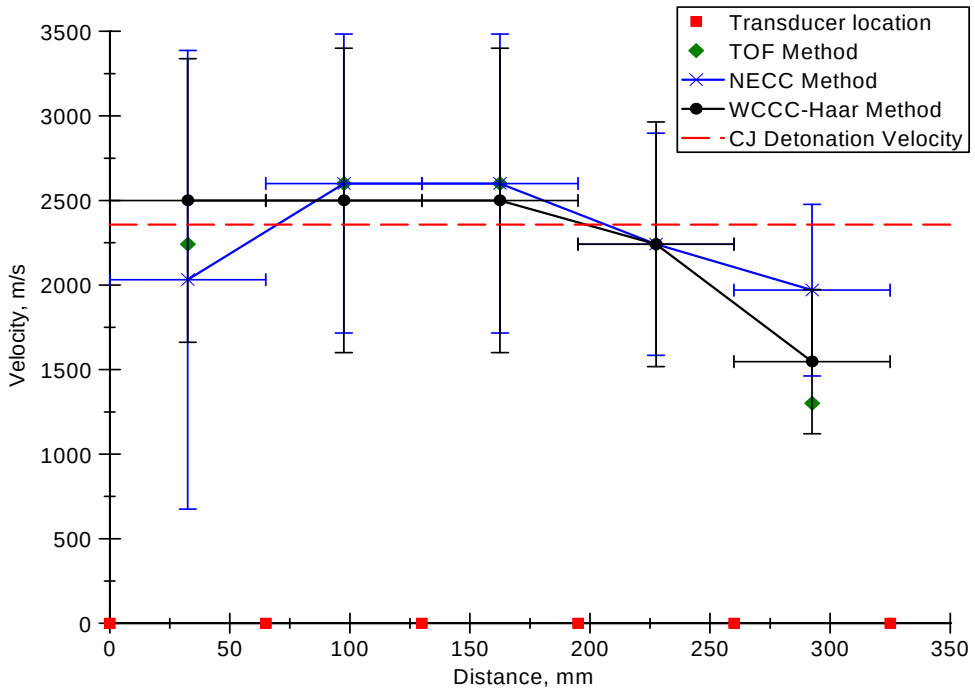

Figure 6.1. Detonation wave speed for the 2nd detonation wave provided in Table 5.7 by the TOF, NECC and WCCC-Haar method.

each other. The NECC method was unable to have a confidence interval that included the estimate by the TOF method. The detonation wave also appears to be slowing down. The velocity estimates as well as the confidence intervals for transducers 4–5 and 5–6 are generally below the CJ detonation velocity.

6.1.3 Rise Time Error

The rise time for the system has a significant effect on the velocity uncertainty results for the PDE. A comparison of the effects of the rise time for the system with and without the recessed transducers are shown in Table 6.6. The recession of the transducers increases the uncertainty by up to 60% for most of the cases. Unfortunately, the recession is a necessity for the pressure transducers used in the experiment.

Table 6.4. Transducer location for both the PDE and shock tube

Transducer #	Location$_{PDE}$, mm	Location$_{ST}$, mm
1	0	0
2	65	100
3	130	200
4	195	300
5	260	–
6	325	–

Another problem is associated with the inability of the transducers to properly capture the detonation wave. The transducers used for the experiment had a diaphragm size of about 5.5 mm. The amount of time required for a detonation wave at the CJ velocity to cross the transducer is approximately 2.33 μs.

For a resonant system, the overall rise time is recommended to be five times less than the observed rise time [33, 32]. Thus, the required rise time for a detonation wave should be 0.47 μs. Another rule of thumb recommended for resonant systems is

$$t_r f_n \geq 2.5 \tag{6.12}$$

which is provided in [32]. To successfully capture the detonation wave, the rise time of the system has to be less than 0.47 μs with a transducer that has a resonant frequency of about 5.4 MHz.

For a nonresonant transducer, the relationship from Eqn. (6.8) is used to determine the required natural frequency. The time taken by the wave to cross the transducer is divided by two to satisfy the Nyquist–Shannon sampling theorem. The minimum frequency required to acquire the detonation wave is about 860 kHz with a minimal rise time of 0.53 μs. The frequency required to capture the detonation wave is significantly reduced with the use of a nonresonant transducer.

Table 6.5. Detonation wave speed results for the 2nd detonation wave with a (95%) confidence level for the TOF, NECC and WCCC-Haar method

	Transducers 1–2		Transducers 2–3		Transducers 3–4		Transducers 4–5		Transducers 5–6	
Method	$\hat{V}$, m/s	u_V, m/s	$\hat{V}$, m/s	u_V, m/s	$\hat{V}$, m/s	u_V, m/s	$\hat{V}$, m/s	u_V, m/s	$\hat{V}$, m/s	u_V, m/s
TOF pk-pk	2241	–	2600	–	2600	–	2241	–	1300	–
NECC	2031	1356	2600	884	2600	884	2241	657	1970	507
WCCC-Haar	2500	839	2500	900	2500	900	2241	723	1548	426

Table 6.6. A comparision of the effect of recessing the transducer propagating to the velocity uncertainty

	Transducers 1–2		Transducers 2–3		Transducers 3–4		Transducers 4–5		Transducers 5–6	
Mounting	Recessed	Flush	Recessed	Flush	Recessed	Flush	Recessed	Flush	Recessed	Flush
Method	u_V, m/s	u_V, m/s	u_V, m/s	u_V, m/s	u_V, m/s	u_V, m/s	u_V, m/s	u_V, m/s	u_V, m/s	u_V, m/s
NECC	1356	1288	884	547	884	547	657	407	507	314
WCCC-Haar	839	540	900	631	900	631	723	507	426	348

Table 6.7. Mach number estimates for the incident shock wave with a (95%) confidence level for the TOF, NECC and WCCC-Haar method

	Transducers 1–2		Transducers 2–3		Transducers 3–4	
Method	$\hat{V}$	u_V	$\hat{V}$	u_V	$\hat{V}$	u_V
TOF pk-pk	1.95	–	1.83	–	1.52	–
NECC	1.63	0.05	1.69	1.07	1.51	0.08
WCCC-Haar	1.65	0.05	1.54	0.05	1.57	0.06

6.1.4 Shock Tube Uncertainty

Unlike the PDE experiment, the pressure transducers were not recessed for the shock tube experiment. So the uncertainty caused by the rise time of the system is reduced significantly for the shock tube experiment. The uncertainty in the velocity was determined the same way as the case with the PDE. The velocity was then normalized by the speed of sound to provide a plot of the Mach number for the incident shock wave. The plot is shown in Fig. 6.2. The results are also provided in Table 6.7. The location of the transducers are provided in Table 6.4. The figure clearly shows that the TOF method is not the best solution. The TOF method provided an estimate that was much larger than the NECC and WCCC-Haar method for transducers 1–2. The large uncertainty from the application of the NECC method is clearly shown to propagate to the uncertainty in the velocity estimate for transducers 2–3.

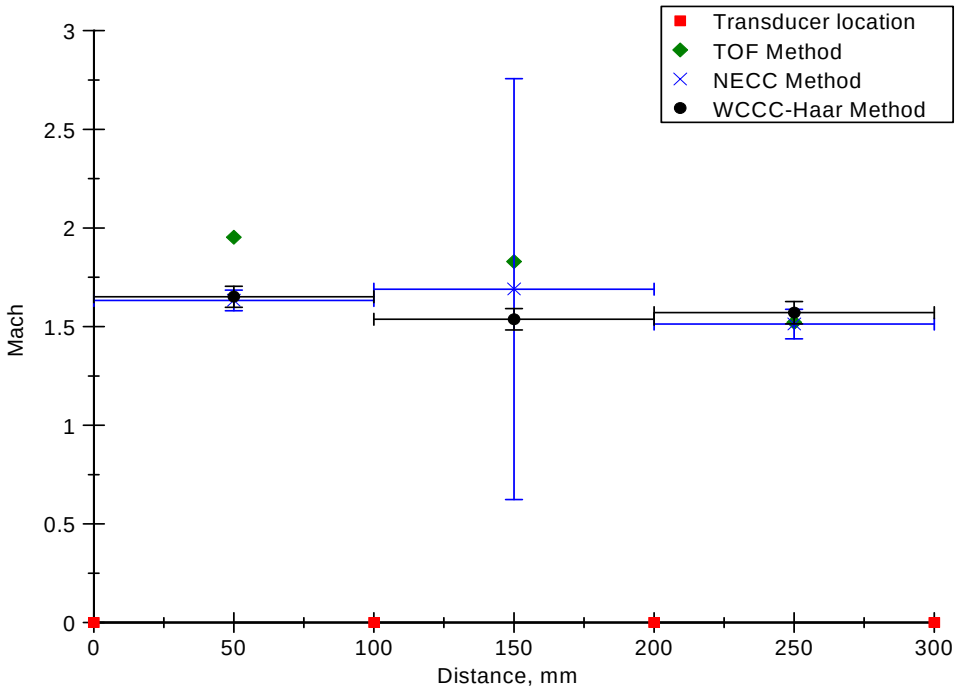

Figure 6.2. The Mach number estimate for the incident shock wave by the TOF, NECC and WCCC-Haar method.

CHAPTER 7

CONCLUSION & RECOMMENDATIONS

7.1 Conclusion

Several methods were developed to provide a statistical estimate of the propagation time for a shock and detonation wave, including an estimate of the uncertainty. The time delay estimate can then be used to determine the velocity of the propagating wave. The study showed that several methods were unable to provide a good estimate of the time delay. These methods were especially evident for the shock tube cases, which proved to be troublesome for most of the methods. Generally, for the methods incorporating the moving time window the estimate varied significantly when the lower and upper time indexes approached the disturbance. The uncertainty increased due to the limited amount of samples being used to determine the time delay estimate. All of the phase methods (NCSDP, NCSDPE, CSDP-2 and CSDP-2E) were very sensitive to the moving time window. The sensitivity of the phase methods with the time window was shown by their large variances for the time delay estimate.

The use of the envelope signal tended to improve the time delay estimates when applied. The improvements can clearly be seen by comparing the methods with (NECC, NCSDPE and CSDP-2E) and without (NCCC, NCSDP and CSDP-2) the application of the envelope signals in the time delay estimates. The time delay estimates improved with a smaller variance for the methods including the application of the envelope signals. The improvements noted with the application of the envelope signal were because the correlated peaks became sharper and less prone to the moving time window. Since the envelope signal makes the methods less prone to the moving

time window, it allows for a more relaxed selection of the lower and upper time indexes without the worry of any significant difference in the time delay estimate.

Only the NECC, WCCC-Haar and WECC-Haar methods were able to on a continuous basis provide feasible time delay estimates for the propagating waves. The selection between the three methods is difficult as each has their own benefits. The wavelet methods require less computational time than the NECC method since the methods do not require the use of the moving time window. The computational time required for the wavelet methods allow for the possibility of having a real-time analysis for repeated detonation pulses in a PDE. However, the NECC method is more relaxed with the time delay estimate because it accounts for more possibilities due to the moving time window.

7.2 Recommendations & Future Work

Several of the techniques can use better methods for determining the propagation time. For the NHCCC method, a better interpolation method may be required to improve the zero crossing estimate. The current method for identifying the zero crossing is with a linear interpolation. Further research is needed to identify which type of interpolation provides the best results for the disturbances. Slight changes to the NCSDP and NCSPD-E method might improve the time delay estimate. A higher coherence limit will improve the results, but identifying the best coherence limit for obtaining the time delay estimate needs to be researched. Also, a survey of the best weighting functions for the shock and detonation wave is required to improve the time delay estimates for all the phase methods. The time delay estimates for the wavelet methods can be further improved with the use of a better basis function. Only the Haar and Morlet wavelet basis function were used for the present study. A better

technique for the wavelet methods needs to be implemented to eliminate the artifacts noted for the shock tube cases.

The time window that consists of the upper and lower time indexes can also be improved. An algorithm that determines the optimal reduction in the time indexes (L and U) near the disturbance may improve the time delay estimates. The reduction of the time indexes near the disturbance will discard the cases with time windows that have limited data to identify the delay between the signals. The reduction of indexes will also improve the computational time.

Further improvements to the data acquiring process is also needed to properly capture the propagating disturbances. Sensors with a faster rise times, a higher -3dB bandwidth frequency, and the ability to withstand the extreme temperatures and pressures are needed. With the improvements in technology, it is possible that a non-obtrusive sensor with these capabilities could be developed in the near future.

Currently, it is recommended for offline analysis that a combination of the results from the NECC and WECC-Haar method be used for determining the time delay estimates. On the other hand, the WCCC-Haar is recommended for online analysis that require close to real-time results.

Some future work needs to be devoted to developing a method that utilizes the new Hilbert-Huang transform (HHT) or one of its variants. The HHT is a relatively new technique that is still not fully developed like the Fourier and wavelet transform. The HHT appears to be a very promising transformation that has several properties that are superior to the current transformations. Some of the properties associated with the HHT that are superior to the Fourier and wavelet transform are the following:

1. adaptive basis function
2. not limited by the uncertainty principle and
3. has the ability to analyze both nonlinear and nonstationary signals [34].

It is recommended to wait for the HHT to become more mature before applying the technique for time delay analysis.

APPENDIX A

NOMENCLATURE

A	instantaneous amplitude
A_{dia}	area of the diaphragm
a	scale dilation parameter
a_{sound}	speed of sound
B	bandwidth
b	translation parameter
C_{ψ}	admissibility condition
c	damping coefficient
CWT	continuous wavelet transform (CWT)
E	energy
$E[\ ]$	expected value of [ ]
E_{CWT}	wavelet energy spectrum
e_i	elemental errors
f	frequency
$F\{\ \}$	Fourier transform of { }
f_{-3dB}	-3dB bandwidth
F_a	pseudo-frequency
F_c	center frequency of the wavelet
$f_{aliased}$	aliased frequency
f_b	wavelet's variance bandwidth
f_c	wavelet's central frequency
f_n	resonant frequency
f_o	center frequency
f_{ratio}	ratio of the spectral resolution for the zoom transform and the Fourier transform

f_s	sampling rate
f_{signal}	bandwidth of the signal
G_{xx}	one-sided autospectral density function
G_{xy}	one-sided cross-spectral density function
$\mathcal{H}[\ ]$	Hilbert transform of [ ]
$\Im[\ ]$	imaginary value of [ ]
i	index value
i_τ	index value for time delay
j	$=\sqrt{-1}$, imaginary value
K	sensitivity
k	spring constant, frequency index
L	lower boundary index value
l	time index value
M	number of increments for nonstationary process
m	mass; modified time delay index value
N	sample size
n	index value
n_d	number of averages
P	pressure, probability
$P\,(\ \ )$	Cauchy principal value
Q	relative bandwidth grid
R_{xx}	autocorrelation function
R_{xy}	cross-correlation function
$\Re[\ ]$	real value of [ ]
S_{xx}	two-sided autospectral density function

S_{xy}	two-sided cross-spectral density function
T	Temperature
t	time
t_r	rise time
U	upper boundary index value
u_i	uncertainty of i^{th} component
u_V	velocity uncertainty
$(u,\, v)$	squared envelope of $(x,\, y)$
V	velocity
V	Chapman-Jouguet detonation velocity
W_{xx}	two-sided nonstationary autospectral density function
W_{xy}	two-sided nonstationary cross-spectral density function
$\mathcal{W}_{xx}$	discrete two-sided nonstationary autospectral density function
$\mathcal{W}_{xy}$	discrete two-sided nonstationary cross-spectral density function
WC_{xx}	wavelet autocorrelation function
WC_{xy}	wavelet cross-correlation function
WR_{xy}	wavelet cross-correlation coefficient
$(X,\ Y)$	Fourier transform of series $(x,\ y)$
$x\,(t)\,, y\,(t)$	time-dependent variables
x_d	displacement
z	analytic function
$<\ >$	mean ensemble value
$(\tilde{})$	Hilbert transform
*	complex conjugate
$(\hat{})$	estimated value

$(\bar{\ })$	mean value
γ_{xy}	coherence function
Δ_t	temporal width
Δ_t^2	time duration
Δf	spectral resolution
Δf_{zoom}	spectral resolution for the zoom transform
ΔL	transducer separation distance
Δt	time resolution
Δ_ω	spectral width
Δ_ω^2	frequency bandwidth
$\Delta\phi_{xy}$	cross-spectral phase angle uncertainty
ζ	damping ratio
θ	phase angle
$\dot{\theta}$	instantaneous phase angle
θ_{CWT}	phase angle for the CWT
θ_i	sensitivity index
θ_{xy}	cross-spectral phase angle
μ	mean value
ρ_{xy}	cross-correlation coefficient
ρ_{xx}	autocorrelation coefficient
ρ_{uv}	envelope correlation coefficient
$\sigma(\ )$	standard deviation
τ	time delay
τ_{iMax}	time delay for maximum correlated value
Ψ	Fourier transform of the wavelet function

ψ	wavelet function (mother wavelet)
$\psi_{a,b}$	translated and dilated wavelet function (daughter wavelet)
ω	angular frequency
ω_d	ringing frequency
ω_n	undamped natural frequency

APPENDIX B

PRESSURE TRANSDUCER CHARACTERISTICS

All these properties were provided on PCB's website for pressure transducer Model 111A24.

Table B.1. The performance properties for the pressure transducer (PCB Model 111A24)

Performance	**English**	**SI**
Measurement Range(for ± 5 V output)	1 kpsi	6895 kPa
Useful Overrange (for ± 10 V output)	2 kpsi	13790 kPa
Sensitivity(± 0.5 mV/psi)	5.0 mV/psi	0.73 mV/kPa
Maximum Pressure (static)	10 kpsi	68950 kPa
Resolution	0.020 psi	0.14 kPa
Resonant Frequency	$\geq$ 400 kHz	
Rise Time(Reflected)	$\leq$ 1.5 μs	
Low Frequency Response (−5 %)	0.005 Hz	
Non-Linearity	$\leq$ 2.0 % FS	

Table B.2. The environmental properties for the pressure transducer (PCB Model 111A24)

Environmental	**English**	**SI**
Acceleration Sensitivity	$<$ 0.002 psi/g	$<$ 0.0014 kPa/(m/s^2)
Temperature Range (Operating)	−100 to +275°F	−73 to +135°C
Temperature Coefficient of Sensitivity	$\leq$ 0.2 %/°F	$\leq$ 0.36 %/°C
Maximum Flash Temperature	3000 °F	1649 °C
Maximum Vibration	2000 g pk	19614 m/s^2 pk
Maximum Shock	20,000 g pk	196140 m/s^2 pk

Table B.3. The electrical properties for the pressure transducer (PCB Model 111A24)

Electrical	
Output Polarity (positive pressure)	Positive
Discharge Time Constant (at room temp.)	$\geq$ 100 s
Excitation Voltage	20 to 30 VDC
Constant Current Excitation	2 to 20 mA
Output Impedance	$\leq$ 100 Ω
Output Bias Voltage	8 to 14 VDC

Table B.4. The physical properties for the pressure transducer (PCB Model 111A24)

Physical	**English**	**SI**
Sensing Geometry	Compression	
Sensing Element	Quartz	
Housing Material	17–4 Stainless Steel	
Diaphragm	Invar	
Sealing	Epoxy	
Electrical Connector	10–32 Coaxial Jack	
Weight	0.21 oz	6 gm

APPENDIX C

WAVELET SCALES

The scales used for the wavelet methods can be related to frequency. A pseudo-frequency F_a is used to correspond to a given scale a for a wavelet. The relationship used to relate the pseudo-frequency and scale is the following

$$F_a = \frac{F_c F_s}{a} \tag{C.1}$$

where the center frequency of the wavelet F_c varies depending on the wavelet function used. The center frequency of the wavelet represents a periodic signal that matches the mother wavelet function. The periodic signal is the best approximation that captures the main wavelet oscillations [35]. An example of a periodic signal (blue line) approximating a Morlet wavelet (black line) is provided in Fig. C.1. The approximation is very good for the main oscillations. For the smaller oscillations, the approximation drifts from the actual oscillating effect produced by the wavelet function. Since the center frequency of the wavelet is an approximation, the relationship between scale and frequency is not exact. Hence, a pseudo-frequency is introduced that closely approximates a frequency for a given scale. The center frequency for both the Haar and Morlet wavelet functions are provided in Table C.1. The Haar function is a uniform periodic function, so it has nearly a 1:1 ratio for the center frequency approximation. The Morlet wavelet has a center frequency that is less than unity because the period between oscillations is greater than one.

Table C.1. The center frequency of the wavelet approximations for both the Haar and Morlet wavelet functions

	Haar wavelet	Morlet wavelet
F_c, Hz	0.9961	0.8125

An example of converting a scale to a frequency is provided by the following. For the Morlet wavelet, the center frequency of the wavelet is 0.8125 Hz. The shock tube

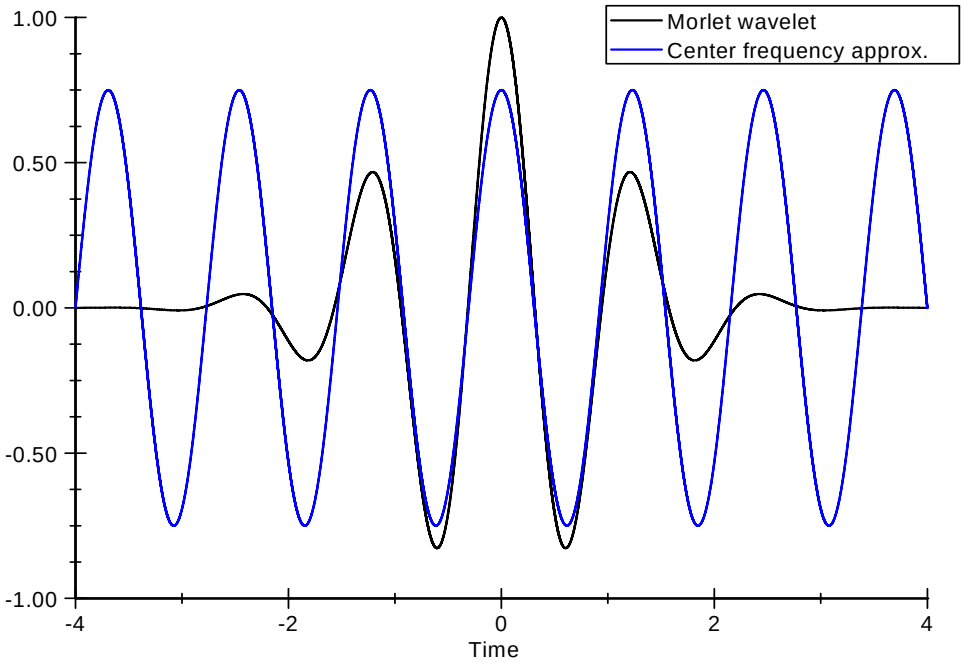

Figure C.1. Center frequency approximation of the Morlet wavelet function.

experiment was captured at 500 kHz. Hence, in this example, the pseudo-frequency for a scale value of 10 for the Morlet wavelet is 40625 Hz.

$$F_a = \frac{(0.8125)\,(500000)}{10} = 40625 \text{ Hz} \tag{C.2}$$

REFERENCES

[1] C. M. Harris, *Shock and Vibration Handbook*, 4th ed. NY: McGraw-Hill, 1996.

[2] Anon., *LabVIEW Analysis Concepts*, march ed. TX: National Instruments, 2004. [Online]. Available: http://www.ni.com

[3] E. Ocana, D. Stich, E. Carmona, F. Vidal, M. Breton, M. Navarro, and A. Garcia-Jerez, "Spatial analysis of the la paca, se spain, 2005 seismic series through the relative location of multipets and principal component analysis," *Physics of the Earth and Planetary Interiors*, vol. 166, pp. 117–127, 2008.

[4] J. Murray, S. Wermter, and H. Erwin, "Auditory robotic tracking of sound sources using hybrid cross-correlation and recurrent networks," in *2005 IEEE/RSJ International Conference Intelligent Robots and Systems*.

[5] T. Okano, L. L. Beranek, and T. Hidaka, "Relations among interaural cross-correlation coefficient ($iacc_E$), lateral fraction (lf_E), and apparent source width (asw) in concert halls," *The Journal of the Acoustical Society of America*, vol. 104, no. 1, pp. 255–265, 1998.

[6] J. Yang, Y. Wen, and P. Li, "Leak location using blind system identification in water distribution pipelines," *Journal of Sound and Vibration*, vol. 310, pp. 134–148, 2008.

[7] A. Rowey, S. Payne, I. Tachtsidis, J. Whiteley, D. Gavaghan, L. Tarassenko, M. Smith, C. Elwell, and D. Delpy, "Synchronization between arterial blood pressure and cerebral oxyhaemoglobin concentration investigated by wavelet cross-correlation," *Physiological Measurement*, vol. 28, pp. 161–173, 2007.

[8] D. Maraun and J. Kurths, "Cross wavelet analysis: significance testing and pitfalls," *Nonlinear Processes in Geophysics*, vol. 11, no. 4, pp. 505–514, 2004.

[9] A. Grinsted, J. Moore, and S. Jevrejeva, "Application of the cross wavelet transform and wavelet coherence to geophysical time series," *Nonlinear Processes in Geophysics*, vol. 11, no. 5, pp. 561–566, 2004.

[10] S. Klimenko, G. Mitselmakher, and A. Sazonov, "A cross-correlation technique in wavelet domain for detection of stochastic gravitational waves," 2002. [Online]. Available: http://www.citebase.org/abstract?id=oai:arXiv.org:gr-qc/0208007

[11] H. Li and T. Nozaki, "Applications of wavelet cross-correlation analysis to a plane turbulent jet," *Japan Society of Mechanical Engineers International Journal Series B*, vol. 40, no. 1, pp. 58–66, 1997.

[12] J. S. Bendat and A. G. Piersol, *Engineering Applications of Correlation and Spectral Analysis*, 2nd ed. NY: John Wiley and Sons, Inc., 1993.

[13] ——, *Random Data Analysis and Measurement Procedures*, 3rd ed. NY: John Wiley and Sons, Inc., 2000.

[14] P. H. Wirsching, T. L. Paez, and K. Ortiz, *Random Vibrations Theory and Practice*. NY: John Wiley and Sons, Inc., 1995.

[15] C. W. de Silva, Ed., *Vibration Monitoring, Testing, and Instrumentation*. Boca Raton: CRC Press, 2007.

[16] R. S. Figliola and D. E. Beasley, *Theory and Design for Mechanical Measurements*, 3rd ed. NY: John Wiley and Sons, Inc., 2000.

[17] S. W. Smith, *Digital Signal Processing: A Practical Guide for Engineers and Scientists*. CA: California Technical Publishing, 2002.

[18] K. A. Ramsey, "Effective measurements for structural dynamics testing - part ii," *Sound and Vibration*, vol. 10, no. 4, pp. 783–791, 1976.

[19] S. L. Hahn, *Hilbert Transforms in Signal Processing*. MA: Artech House, 1996.

[20] M. Vetterli and J. Kovacevic, *Wavelets and Subband Coding*. NJ: Prentice Hall PTR, 2007.

[21] A. Teolis, *Computational Signal Processing with Wavelets*. MA: Birkhauser, 1998.

[22] S. Qian, *Introduction to Time-Frequency and Wavelet Transformations*. NJ: Prentice Hall PTR, 2002.

[23] C. K. Chui, *An Introduction to Wavelets*. CA: Academic Press, 1992.

[24] P. S. Addison, *The Illustrated Wavelet Transform Handbook: Introductory Theory and Applications in Science, Engineering, Medicine and Finance*. Boca Raton: CRC Press, 2002.

[25] M. S. Tiscareno, J. A. Burns, P. D. Nicholson, M. M. Hedman, and C. C. Porco, "Cassini imaging of saturns rings ii. a wavelet technique for analysis of density waves and other radial structure in the rings," *Icarus*, vol. 189, no. 1, pp. 14–34, 2007.

[26] F. K. Lu and C. Kim, "Detection of wave propagation by cross correlation," in *Proceedings of the 38th Aerospace Sciences Meeting and Exhibit*, 2000.

[27] D. Avitzour, "Time delay estimation at high signal-to-noise ratio," *IEEE Transactions on Aerospace and Electronic Systems*, vol. 27, no. 2, pp. 234–237, 1991.

[28] J. S. Bendat, *The Hilbert Transform and Applications to Correlation Measurements*. Denmark: Bruel & Kjaer, Inc., 1985.

[29] M. P. Norton and D. G. Karczub, *Fundamentals of Noise and Vibration Analysis for Engineers*, 2nd ed. United Kingdom: Cambridge University Press, 2003.

[30] D. J. Inman, *Engineering Vibration*, 2nd ed. NJ: Prentice Hall, 2001.

[31] W. Fickett and W. C. Davis, *Detonation Theory and Experiment*. NY: DOVER Publications, INC., 2000.

[32] P. L. Walter, "Shock and blast measurement – rise time capability of measurement systems? tn-11," 2004. [Online]. Available: http://www.pcb.com/

[33] ——, *The Handbook of Dynamic Force, Pressure and Acceleration Measurement*. Endevco Corp., 2001.

[34] N. E. Huang and S. S. Shen, Eds., *Hilbert-Huang Transform and Its Applications*. NJ: World Scientific, 2005.

[35] Anon., *Wavelet Toolbox ™: scal2frq*. TX: MathWorks, 2008. [Online]. Available: http://www.mathworks.com/

BIOGRAPHICAL STATEMENT

Alfredo Albert Ortiz was born on April 21, 1982 in San Benito, Texas. Albert would later receive his diploma at San Benito High school in May 2000. He then enrolled at the Unversity of Texas to pursue one of his many dreams. He would then graduate with a Bachelor of Science in Aerospace Engineering in May of 2004. He then took a break from his academic career before continuing his educatation at the University of Texas at Arlington in the Spring of 2006. He then became involved with the PDE group, which help provide the foundation for his research as he pursued his Masters of Science in Aerospace Engineering degree.